The Dependence of Star Formation Quenching and of Lyman Alpha Escape on Galaxy Structural Properties

by

Keunho Kim

A Dissertation Presented in Partial Fulfillment
of the Requirements for the Degree
Doctor of Philosophy

Approved July 2020 by the
Graduate Supervisory Committee:

Sangeeta Malhotra, Co-Chair
Nathaniel R. Butler, Co-Chair
James E. Rhoads
Sanchayeeta Borthakur
Rolf A. Jansen

ARIZONA STATE UNIVERSITY

August 2020

ABSTRACT

Galaxy structural properties such as size, morphology, and surface brightness bear the imprint of galaxies′ evolutionary histories, and so are related with other properties such as stellar mass, star formation rate, and emergent spectra. In this dissertation, I present three studies exploring such relationships. In the first, I investigated the relationships between 4000 Å break (D4000) strength, colors, stellar masses, and morphology in a sample of 352 galaxies at intermediate redshifts based on photometric and spectroscopic data from the *Hubble Space Telescope (HST)*. I explored several diagrams such as *UVJ* color space combined with the D4000 strengths and the structural parameters of sample galaxies. The analysis shows that the presence of a bulge component is a necessary but not sufficient requirement for star formation quenching at intermediate redshifts. In the second study, I investigated the central 250 pc UV star formation intensity $S_{250\mathrm{pc}}$ (SFI, star formation rate per unit area) of a sample of 40 Green Pea (GP) galaxies and 15 local Lyman Break Galaxy Analogs (LBAs) to understand the Lyα escape mechanisms and the associations with the SFI in Lyα-emitters (LAEs). I utilized the Cosmic Origins Spectrograph near-ultraviolet (COS/NUV) images from the *HST*. I found that the Lyα equivalent width (EW(Lyα)) and the Lyα escape fraction ($f_{esc}^{Ly\alpha}$) are positively correlated with the ratio of SFI to galaxy stellar mass ($S_{250\mathrm{pc}}/M_{\mathrm{star}}$). These correlations suggest the importance of the central SFI in Lyα photon escape. In the third study, I investigated the UV photometric properties of a sample of 40 GPs and the possible associations with Lyα escape mechanisms. I measured the UV-continuum size and luminosity of the sample galaxies by employing the COS/NUV images. The circularized half-light radius ($r_{\mathrm{cir},50}$) of GPs shows compact sizes and it further shows the statistically significant anti-correlations with EW(Lyα) and $f_{esc}^{Ly\alpha}$. The size comparison of GPs to those of high-redshift LAEs shows that their sizes are similar, once spatial resolution effects

are properly considered. These results show that a compact size is crucial for escape of Lyα photons, and that Lyα emitters show constant characteristic size independent of their redshift. Therefore, the results presented in this dissertation emphasize the importance of galaxy structural properties in star formation quenching and in Lyα escape.

ACKNOWLEDGMENTS

First, I would like to thank my advisors Sangeeta Malhotra and James Rhoads for their academic guidance and support during my PhD. Their insights and suggestions have inspired me to learn how to research in Astronomy. I also would like to thank Nathaniel Butler for his suggestions on research and particularly for acting as a co-advisor for the past two years. I thank Sanchayeeta Borthakur for her time to be on my committee and her insights during our science discussions. I thank Rolf Jansen for his time to be on my committee and his detailed explanations about the *HST* MAMA detector and CCD instruments.

I would like to thank the other group members of Malhotra-Rhoads, Vithal Tilvi, Karen Olsen, Huan Yang, John Pharo, Tianxing Jiang, Alicia Coughlin, Bhavin Joshi, Lucia Perez, Santhosh Harish, Isak Wold, and Ali Khostovan for their encouragement and discussions. I also thank my officemates Mansi Padave, Tyler McCabe, and Christopher Dupuis, Hansung Gim, and Ozan Erdogan for making our office a lively and vibrant place.

I want to thank my colleagues in the Department of Astronomy at Yonsei University. Their motivation for astronomy and encouragement is really grateful.

Also, I would like my parents and sister for their devoted love. Lastly, I would like to thank my wife, Eunjung, for her unconditional support!

TABLE OF CONTENTS

CHAPTER Page

CHAPTER Page

LIST OF TABLES

LIST OF FIGURES

Chapter 1

INTRODUCTION

1.1 Galaxy Structure as the Footprints Bearing Galaxy Properties

Galaxy structural properties such as visual morphology, size, stellar density, and the concentration of stellar light have shown tight relationships with other galaxy properties such as stellar mass, the amount of star formation activity (star formation rate), and their environments whether galaxies reside in denser regions with more neighboring galaxies. Thus, the galaxy structural properties have provided important information about the formation and evolution histories of galaxies (e.g., Dressler, 1980; Lang *et al.*, 2014; Oh *et al.*, 2013; Conselice, 2014; Huertas-Company *et al.*, 2015; Khim *et al.*, 2015; Kim *et al.*, 2016, 2018, and references therein).

For instance, one of the most representative galaxy morphological schemes is the Hubble morphology classification (Hubble, 1926, 1936) where galaxies are visually-classified as a function of the dominance of round central bulge component, the extent of spiral arms wound in spiral galaxies, the presence of a galaxy bar component, and the overall shape of galaxies such as roundness and irregularity. While such morphological classification was solely based the observed images of galaxies, and thus there is no prior information about the stellar properties of constituent stellar populations such as overall stellar age, the amount of metal contents (metallicity) of stars, and the amount of star formation activity, subsequent studies of constituent stellar populations of galaxies have shown tight relationships of classified morphology and the overall stellar properties. Such tight relationships suggest the significant associations of galaxy structure with galaxies′ star formation history over cosmic

time. Specifically, round and elliptical-shaped galaxies largely consist of relatively old and metal contents enhanced stars often devoid of interstellar gas, whereas spiral arm and disk-shaped galaxies consist of young and metal contents poor stars with large amount of interstellar gas (Proctor and Sansom, 2002; Saintonge *et al.*, 2012; Oh *et al.*, 2013).

These close relationships between galaxy structural properties and the overall ages and metal contents of constituent stars mentioned above have led to the idea of the possible role of galaxy structure in stopping star formation activity (a.k.a., galaxy star formation quenching) of galaxies, given that round and elliptical galaxies tend to be older and to stop their star formation activity earlier compared to spiral arm and disk-shaped galaxies (e.g., Huertas-Company *et al.*, 2015; Kim *et al.*, 2018). In particular, some numerical simulations have shown that the significant gravitational potential of the central dense bulge component can prevent interstellar gas in galactic disk from collapsing to form stars by stabilizing the gas disk structure (Martig *et al.*, 2009, 2013), suggesting the dominance of a central bulge component as one of the physical conditions for star formation quenching in galaxies.

Another astrophysical phenomenon where galaxy structural properties likely play important roles would be understanding the mechanisms for Lyα photon escape from their host galaxies. It has been known that actively star-forming galaxies, typically observed at high redshifts (i.e., $z > 2$), often show the sign of Lyα emission line imprinted in their spectral energy distribution (e.g., Rhoads *et al.*, 2000; Malhotra and Rhoads, 2002, and references therein). Considering that 1) only relatively massive stars (approximately 20 times or more massive than the sun) can emit strong UV radiation for Lyα photons and that 2) the escape of Lyα photons from their host galaxies is not trivial mainly due to the physical nature of Lyα emission being resonantly scattered and sensitive to dust absorption/scattering in the interstellar medium

(ISM), not all actively star-forming galaxies allow Lyα photon escape (e.g., Ahn *et al.*, 2003; Verhamme *et al.*, 2006). In this regard, while several global properties of Lyα-emitting galaxies such as the amount of dust, the amount of metal contents in the ISM, and stellar mass have been extensively investigated to understand the physical mechanisms for Lyα photon escape (e.g., Malhotra *et al.*, 2012; Song *et al.*, 2014; Verhamme *et al.*, 2017, and references therein), it still remains unclear as to exactly why Lyα photons can escape only in some of the actively star-forming galaxies.

It has been known that Lyα lines are a promising indicator of Lyman-continuum leaker galaxies (i.e., galaxies that emit ionizing photons with wavelength 912 Å into the surrounding intergalactic gas). Cosmologically, such LyC leakers are likely contributors for reionizing neutral hydrogen in the early universe ($z > 6$). Lyα emission is also related to star formation mechanisms in galaxies. Therefore, understanding the physical properties of Lyα-emitting galaxies (a.k.a., Lyα emitters, or LAEs) and their Lyα escape mechanisms is important both for cosmology, and for galaxy formation and evolution (e.g., Malhotra and Rhoads, 2002; Verhamme et al., 2015; Izotov et al., 2016).

It has been suggested that most LAEs show compact sizes (i.e., their size, usually measured as their UV radius, is typically smaller than 1.5 kpc) often with multiple clumps, and that their sizes are relatively constant over a wide range of redshift (i.e., $2 \lesssim z \lesssim 6$) (e.g., Malhotra *et al.*, 2012; Bond *et al.*, 2012; Paulino-Afonso *et al.*, 2018). The compact and relatively constant sizes of LAEs are noticeably different morphological properties compared to non-Lyα-emitting star-forming galaxies with comparable stellar mass or star formation rate given that non-Lyα-emitting star-forming galaxies show redshift dependent size growth (van der Wel *et al.*, 2014; Shibuya *et al.*, 2015). To this extent, previous studies (e.g., Malhotra *et al.*, 2012) based on a sample of LAEs over a range of redshift ($2 \lesssim z \lesssim 6$) have suggested that the compact morpho-

logical properties of LAEs are some of the important physical conditions for making a galaxy an LAE. Therefore, to further shed some light on the possible role of compact morphology of LAEs in their Lyα photon escape, it is important to investigate the galaxy structural properties of more sample of LAEs over a wider range of redshift, towards both lower and higher redshifts.

In this context, this dissertation aims to investigate the dependence of star formation quenching and of Lyα escape mechanisms on galaxy structural properties observationally. In particular, for star formation quenching, we explore the relationships between galaxy structure, stellar populations, and star formation quenching for galaxies at intermediate redshifts (i.e., $0.6 \lesssim z \lesssim 1.2$) by fully utilizing most of the available optical photometric and spectroscopic data sets. For the Lyα escape mechanisms, we investigate the UV photometric properties of local universe (i.e., $0.1 \lesssim z \lesssim 0.35$) LAEs dubbed as 'Green Pea' galaxies (Cardamone *et al.*, 2009) (due to their strong [OIII] emission line at their redshifts) and Lyman Break Galaxy Analogs (LBAs) (Heckman *et al.*, 2005). We measure their UV photometric properties such as the central star formation intensity, size, and luminosity to explore the possible associations with their Lyα emission properties. The physical proximity of these local LAEs and the high spatial resolution of near-ultraviolet images we employ are suitable for studying the spatially-resolved morphological analysis of Green Pea galaxies and LBAs.

The studies presented in this dissertation are thus expected to shed some light on the role of galaxy structural properties in star formation quenching mechanisms and in Lyα escape mechanisms observationally.

1.2 Dissertation Outline

This dissertation is organized as follows. In Chapter 2, we investigate the relationships between galaxy structure and the stellar properties such as spectroscopic 4000 Å break (D4000) strength, optical and near-infrared colors, stellar masses in a sample of 352 galaxies with $\log(M_{\rm star}/M_{\odot}) > 9.44$ at intermediate redshifts ($0.6 \lesssim z \lesssim 1.2$). We utilize four different catalogs to obtain both spectroscopic and photometric information such as D4000 strength, visually-classified morphology, star formation rate, stellar mass, Sérsic index, stellar surface density within the effective radius. The combined optical, spectroscopic, and photometric information enables us to explore the morphological *and* stellar properties of galaxies at intermediate redshifts in detail. We discuss our results and implications in the context of star formation quenching.

In Chapter 3, we construct sample of 40 GPs and 15 local Lyman Break Analogs (LBAs) at redshifts ($0.1 \lesssim z \lesssim 0.35$) to understand their central UV photometric properties and the possible associations with Lyα photon escape. We utilize the Cosmic Origins Spectrograph near-ultraviolet (COS/NUV) images from the *Hubble Space Telescope (HST)*. The physical proximity of the sample GPs and LBAs and the high spatial resolution (0.0235 arcsec pixel^{-1}) of the COS/NUV images enable us to study the spatially-resolved central region properties of the sample galaxies. Specifically, we measure the uniform central 250 pc region star formation intensity (SFI, i.e., star formation rate per unit area, equivalently star formation rate surface density) across our sample GPs and LBAs. We investigate the possible correlations between the measured central SFI and the Lyα properties such as the Lyα equivalent width (EW(Lyα)) and the Lyα escape fraction ($f_{esc}^{Ly\alpha}$). We further show the significant role of galaxy stellar mass likely as a proxy for gravitational potentials through the parameter of specific star formation intensity (sSFI, defined as SFI divided by stellar

mass) in Lyα escape mechanisms.

In Chapter 4, we measure the UV-continuum size and luminosity of sample of 40 GPs to investigate their UV photometric properties and the possible associations with Lyα escape mechanisms as local analogs of high-z Lyman-α emitters (LAEs). We utilize the same processed COS/NUV images as used in Chapter 3 to measure the size and luminosity of GPs. The better spatial resolution of the COS/NUV images, compared to those of typically employed images to measure the size of high-z LAEs, enables us to measure the size of GPs with the seeing effects properly taken into account. With the measured size and luminosity, we study the size distribution, the size-luminosity relation, correlations between UV size and Lyα properties such as EW(Lyα) and $f_{esc}^{Ly\alpha}$. Also, we compare the size of GPs with those of high-z LAEs to investigate whether the size of GPs shows comparable sizes to high-z as some of the best local analogs of high-z LAEs, and more fundamentally whether there is any morphologically required compactness of LAEs as one of the important physical conditions to determine whether a galaxy is an LAE, independent of redshift.

In Chapter 5, we summarize the primary results and conclusions of the studies explored in this dissertation.

Chapter 2

GALAXY STRUCTURE, STELLAR POPULATIONS, AND STAR FORMATION QUENCHING AT $0.6 \lesssim z \lesssim 1.2$

2.1 Abstract

We use both photometric and spectroscopic data from the *Hubble Space Telescope* to explore the relationships among 4000 $\mathring{A}$ break (D4000) strength, colors, stellar masses, and morphology, in a sample of 352 galaxies with $\log(M_*/M_\odot) > 9.44$ at $0.6 \lesssim z \lesssim 1.2$. We have identified authentically quiescent galaxies in the UVJ diagram based on their D4000 strengths. This spectroscopic identification is in good agreement with their photometrically-derived specific star formation rates (sSFR). Morphologically, most (that is, 66 out of 68 galaxies, ~ 97 %) of these newly identified quiescent galaxies have a prominent bulge component. However, not all of the bulge-dominated galaxies are quenched. We found that bulge-dominated galaxies show positive correlations among the D4000 strength, stellar mass, and the Sérsic index, while late-type disks do not show such strong positive correlations. Also, bulge-dominated galaxies are clearly separated into two main groups in the parameter space of sSFR vs. stellar mass and stellar surface density within the effective radius, $\Sigma_{\rm e}$, while late-type disks and irregulars only show high sSFR. This split is directly linked to the 'blue cloud' and the 'red sequence' populations, and correlates with the associated central compactness indicated by $\Sigma_{\rm e}$. While star-forming massive late-type disks and irregulars (with D4000 < 1.5 and $\log(M_*/M_\odot) \gtrsim 10.5$) span a stellar mass range comparable to bulge-dominated galaxies, most have systematically lower $\Sigma_{\rm e} \lesssim 10^9 M_\odot {\rm kpc}^{-2}$. This suggests that the presence of a bulge is a necessary but not sufficient requirement for

quenching at intermediate redshifts. This chapter previously published as Kim et al. (2018).

2.2 Introduction

How galaxies have formed and evolved over the Hubble time remains a challenging question in extragalactic astronomy. In particular, why and how galaxies have stopped their star formation activities during the course of their evolutionary paths is not clearly understood yet. Observational aspects have shown that galaxies largely form a bimodality in diverse diagrams (e.g., the Color-Magnitude diagram (CMD), the color-color diagram, and global star formation rate (SFR) versus stellar mass diagram), being separated into an actively star-forming group and a star-formation quiescent group. The former group forms the 'blue cloud', while the later group forms a tight 'red sequence' in the CMD. The intermediate parameter space, between the blue cloud and the red sequence, forms the 'green valley' (Strateva *et al.*, 2001; Schawinski *et al.*, 2014; Pandya *et al.*, 2017; Bremer *et al.*, 2018; Gu *et al.*, 2018).

Previous studies (e.g., Pasquali *et al.*, 2010; Peng *et al.*, 2010b) have suggested that two main mechanisms quenched the star formation activity in galaxies. The first is mass-quenching, which indicates that the more massive galaxies are, the earlier they likely had formed stars and shut down star formation activities (i.e., "downsizing" scenario) (Cowie *et al.*, 1996; De Lucia *et al.*, 2006; Haines *et al.*, 2017). The second is environmental quenching, which states that denser environments tend to make galaxies more passive, resulting in a larger fraction of quenched galaxies than in less dense regions (Pasquali *et al.*, 2010; Peng *et al.*, 2010b; Khim *et al.*, 2015).

Along with these two main mechanisms of quenching galaxies over a wide span of redshift, morphological properties of quiescent galaxies and star-forming counterparts show that quiescent galaxies tend to have a prominent bulge component, while most

of star-forming galaxies tend to have prominent disk or clumpy structures (Oh *et al.*, 2013; Huertas-Company *et al.*, 2016). These morphologically-entangled features of quiescent and star-forming populations of galaxies have led to an idea of 'morphological quenching' of galaxies (Martig *et al.*, 2009; Dekel *et al.*, 2009; Martig *et al.*, 2013; Dekel and Burkert, 2014; Genzel *et al.*, 2014). In addition to morphology, analyses of internal structure of galaxies based on galaxy structural parameters, such as the central surface density, a bulge-to total ratio, and the Sérsic index, also suggest that the presence of a prominent bulge component (or, similarly, compact central density in galaxy center) in galaxies, as the results of 'inside-out' growth, is related to the quenching of galaxies. (Franx *et al.*, 2008; Ilbert *et al.*, 2010; van Dokkum *et al.*, 2010; Bell *et al.*, 2012; Saintonge *et al.*, 2012; Bluck *et al.*, 2014; Lang *et al.*, 2014; Tacchella *et al.*, 2015, 2016; Lilly and Carollo, 2016; Huertas-Company *et al.*, 2016; Jung *et al.*, 2017; Whitaker *et al.*, 2017; Williams *et al.*, 2017).

Although the community seems to agree on the presence of a prominent bulge component as a useful indicator associated with quenched galaxies, the mechanisms that are responsible for a bulge growth and the associated galaxy structure evolution have not been fully understood yet (Conselice, 2014, for a review). Recent studies (e.g., Margalef-Bentabol *et al.*, 2016; Huertas-Company *et al.*, 2015, 2016) have suggested that fractions of different morphological types of galaxies have evolved over cosmic time and the associated morphology-related dominant quenching mechanisms have changed accordingly. However, most of studies at intermediate or high redshifts (e.g., Huertas-Company *et al.*, 2016; Ownsworth *et al.*, 2016; Haines *et al.*, 2017) have mainly focused on either optical photometric properties of galaxies with their morphology or spectroscopic and photometric properties of galaxies with a lack of morphological information.

In this study, we investigate the stellar properties of galaxies in the redshift range $0.6 \lesssim z \lesssim 1.2$ throughout the Hubble sequence (Hubble, 1926, 1936), combining optical spectroscopic and photometric properties of galaxies as well as their visual morphological classification. The combination of most currently available optical diagnostics on galaxies enables us to comprehensively explore both the stellar and morphological properties of galaxies within the redshift range of interest, which is our hope in this study. Morphological behaviors in several diagrams such as a $U-V$ vs. $V-J$ color-color (hereafter, UVJ) diagram, the 4000 Å break (i.e., Bruzual A., 1983; Hamilton, 1985) vs. stellar mass, and specific star formation rate (sSFR) vs. stellar mass are investigated.

This chapter is organized as follows: in Section 2.3, we describe the observational data sets employed in this study. In Section 2.4, we describe the 4000 Å break measurements, sample selection, and comparison of visually-classified morphology with other morphology indicators. We present our results in Section 2.5. In Section 2.6, we discuss the stellar and morphological properties of galaxies and the associated quenching mechanisms. We close with a summary in Section 2.7.

We adopt the ΛCDM cosmology of (H_0, Ω_m, Ω_Λ) = (70 kms^{-1} Mpc^{-1}, 0.3, 0.7) wherever necessary. All magnitude in this paper are quoted in the AB system (Oke and Gunn, 1983).

2.3 The Observation Data Sets

2.3.1 The PEARS Survey

The 4000 Å break (hereafter, D4000) information for our sample galaxies is obtained from the Probing Evolution And Reionization Spectroscopically survey (PEARS; PI: S. Malhotra). The PEARS wide survey observed 8 fields, four each in the

GOODS-North and GOODS-South (Giavalisco *et al.*, 2004) regions. The slitless grism ACS/G800L instrument used for the survey has an average dispersion of 40 Å pixel^{-1} and the spectral resolution R = 100 at 8000 Å. The grism data are suitable for measuring the D4000 strength for galaxies within the redshift range of $0.6 \lesssim z \lesssim 1.2$, taking into consideration the observed wavelength coverage of the ACS/G800L instrument.

2.3.2 Morphology Classification

Galaxy morphology information is obtained from the CANDELS (Grogin *et al.*, 2011; Koekemoer *et al.*, 2011) visual morphology classification catalog provided by Kartaltepe *et al.* (2015). In that paper, the authors performed visual classifications on the four *HST* bands (F606W, F850LP, F125W, and F160W) by voting for the most likely morphological types (among disk, spheroid, irregular/peculiar, compact/unresolved, and unclassifiable) for individual galaxies. Specifically, in the visual morphology classification procedure, the F160W band was primarily used and the other three bands were also used to cover different rest-frame wavelengths sensitive to different types of galaxy structures. Thus, the rest-frame wavelengths employed for the morphology classification range from near-UV (~ 3000 $\mathring{A}$) to near-IR (~ 8000 $\mathring{A}$) for most galaxies within the redshift range $0.6 \lesssim z \lesssim 1.2$. The four bands were simultaneously displayed when a classifier voted for morphologies for each galaxy. A minimum size of galaxy images is 84 pixels in each x and y-axis. Regarding voting for the likely morphologies of a galaxy, multiple choices of morphological types for a galaxy are allowed. Thus, the resulting morphology information from the catalog is given as the fractions of individual human classifiers who selected each of the several morphological types. In the following, we are concerned with the fractions of spheroid, disks, and irregulars, denoted as $f_{\rm sph}$, $f_{\rm disk}$, and $f_{\rm irr}$, respectively. Further

details on the morphology classification procedure can be found in Kartaltepe *et al.* (2015).

Four types of morphology are considered in this work and classified as follows: spheroids satisfying the fractions of $f_{\rm sph} > 2/3$ and $f_{\rm disk} < 2/3$ and $f_{\rm irr} < 0.1$, early-type disks satisfying the fractions of $f_{\rm sph} > 2/3$ and $f_{\rm disk} > 2/3$ and $f_{\rm irr} < 0.1$, late-type disks satisfying the fractions of $f_{\rm sph} < 2/3$ and $f_{\rm disk} > 2/3$ and $f_{\rm irr} < 0.1$, and irregulars satisfying the fractions of $f_{\rm sph} < 2/3$ and $f_{\rm irr} > 0.1$. Additionally, regarding the morphology classification difference between early-type disks and late-type disks, we note that the only difference between the two morphological types is the value of $f_{\rm sph}$. That is, with the same morphological fractions of $f_{\rm disk} > 2/3$ and $f_{\rm irr} < 0.1$, if a galaxy has $f_{\rm sph} > 2/3$ ($< 2/3$), the galaxy is classified as early (late)-type disks. Note our adopted morphological classification differs from the traditional approach that follows the Hubble tuning fork diagram, taking into account the spiral arm structure in late-type systems. Therefore, our definition of early-type disks is more likely to focus on the moderate dominance of both bulge and disk components, while our definition of late-type disks is more likely to focus on the dominance of a disk component compared to a relatively small (or no) bulge component, which does not consider the detailed spiral arms features as often adopted in the local Universe.

This classification scheme has been found effective in disks/spheroids separations, considering the close correlations between diskiness/bulginess, Sérsic index n, and optical colors (Kartaltepe *et al.*, 2015; Huertas-Company *et al.*, 2016). Particularly, Kartaltepe *et al.* (2015) showed that their "Mostly Disk" galaxies have relatively lower Sérsic indices with a mean of $\langle n \rangle = 1.01$ and bluer optical colors in the UVJ diagram, while their "Mostly Spheroid" galaxies have relatively higher Sérsic indices with a mean of $\langle n \rangle = 2.98$ and redder optical colors (Kartaltepe *et al.*, 2015, see their Figures 12 and 13). For our sample of galaxies, we will address the visual morphology

and the comparison to other morphology indicators in detail in Section 2.4.3.

The number of classifiers for our sample of galaxies ranges from 3 to 6. The mean number of classifiers is 4.09.

2.3.3 Photometrically-Derived Properties of Galaxies

The photometrically-derived properties such as stellar mass, rest-frame colors, and star formation rate are obtained from the stellar mass catalog of Santini *et al.* (2015), where different stellar masses derived by different spectral energy distribution (SED) fitting procedures are presented and compared. Their fitting is based on the 17 multi-wavelength photometric bands ranging from UV to mid-infrared for the GOODS-South field provided by Guo *et al.* (2013).

Among the different stellar masses provided in the catalog, we adopt the stellar mass derived by the 'Method $6a_{\tau}^{NEB}$', in which Method $6a_{\tau}^{NEB}$ is the team notation with the abbreviations of the SED fitting methods as designated in Santini *et al.* (2015). Specifically, the Method $6a_{\tau}^{NEB}$ makes use of the 'zphot' code for the SED fitting based on the χ^2 minimization fitting method (Giallongo *et al.*, 1998; Fontana *et al.*, 2000). Also, it adopts the Chabrier Initial Mass Function (Chabrier, 2003) and the stellar templates from Bruzual and Charlot (2003) with the exponentially-declining star formation history (so-called the direct-τ model, $\psi(t) \propto \exp(-t/\tau)$). The resulting stellar mass and SFR estimates are provided with the least significant digit being 0.01 dex (base-10 log) and 0.01 decimal, respectively. The minimum SFR is set to 0.00 $M_{\odot}\mathrm{yr}^{-1}$.

Additionally, the Method $6a_{\tau}^{NEB}$ includes the nebular emission component into its SED fitting procedures following the prescription of Schaerer and de Barros (2009), where continuum emission is added to the stellar continuum, and emission lines are treated using the relative line intensities from Anders and Fritze-v Alvensleben (2003)

for non-hydrogen lines such as He, C, N, O, and S, and from Storey and Hummer (1995) for hydrogen lines such as Lyα line and Balmer, Paschen, and Brackett series. Further details on the nebular emission prescription can be found in Schaerer and de Barros (2009). However, more importantly, we note that the differences in stellar mass between those with and without the emission prescription are not significant. That is, the median value of the stellar mass differences is 0.00 $M_{\odot}\mathrm{yr}^{-1}$ for our sample of galaxies that will be described in Section 2.4.2 (see also Figure 3 and the discussion in Section 4.3 of Santini *et al.* (2015) on the nebular emission prescription for further details).

2.3.4 Galaxy Structural Parameters

Galaxy structural parameters for our sample are obtained from the publicly available galaxy structural parameters catalog provided by van der Wel *et al.* (2012). The structural parameters in the catalog were derived by the two-dimensional light profile fitting procedures utilizing the GALFIT software for the CANDELS galaxies (Peng *et al.*, 2002, 2010a). A single Sérsic component model (i.e., Sersic, 1968) was used to fit the two-dimensional light distribution of galaxies. For all of our sample galaxies, the structural parameters are measured with the $F160W$ image. Further details regarding the fitting procedures can be found in van der Wel *et al.* (2012).

2.4 Data Analysis

2.4.1 D4000 Measurements

The D4000 strength has been widely used as an optical regime age indicator for constituent stellar populations of galaxies (Bruzual A., 1983; Hamilton, 1985; Balogh *et al.*, 1999; Kauffmann *et al.*, 2003a; Hathi *et al.*, 2009; Haines *et al.*, 2017). It is

defined by the average flux ratio of the red side continuum to the blue side continuum of 4000 ÅṪhe wavelength ranges for the D4000 measurement are $[4050, 4250]$ and $[3750, 3950]$ Å for the red and blue side continua, respectively (Bruzual A., 1983). The D4000 strength is mainly affected by the combination of several metal lines of constituent stars, including Ca II H and K lines (Hamilton, 1985). Considering the physical properties of stars such as temperature, metallicity, and surface gravity, stars whose spectral types are later than G0 are known to show the strongest D4000 features (Bruzual A., 1983; Hamilton, 1985).

Considering the specifications of the ACS/G800L instrument as low resolution spectroscopy, the grism data sets require the wider definition of D4000 instead of its narrower definition of Balogh *et al.* (1999). The D4000 strengths for our sample of galaxies are measured with the *HST* ACS/G800L Grism data from the PEARS survey as mentioned in 2.3.1. The reduced grism spectra from individual position angles (PA) were combined in the observed frame and we then de-redshifted the observed spectra to the rest-frame. De-redshifting was done by employing the redshift information ('$z_{\rm best}$' column) provided by the SED-fitting stellar mass catalog of Santini *et al.* (2015) that we are adopting in this work. Within the rest-frame spectra, we identified the blue and red continua and calculated the flux ratio of the two continua following the definition of the D4000 strength as described in this section. The errors of our D4000 measurements (δ(D4000)) are also calculated considering the grism spectra fluxes and their measurement uncertainties within the D4000 bandpasses. The typical δ(D4000) of our sample of galaxies that will be described in Section 2.4.2 is 0.09, and the typical relative error (i.e., δ(D4000)/D4000) is 0.06. Further details on the D4000 measurements of this sample are described by Joshi et al. (2019).

2.4.2 Sample Selection

The sample galaxies for this study are constructed by employing the four different catalogs described in Section 2.3. First, we cross-match between the PEARS master catalog [1] , the visually-classified morphology catalog (i.e., Kartaltepe *et al.*, 2015), the stellar mass catalog (i.e., Santini *et al.*, 2015), and the galaxy structural parameters catalog (i.e., van der Wel *et al.*, 2012) by cross-matching the right ascension and declination information with a cross-matching radius of $0.05''$. The cross-matching results in 2923 galaxies. We further reduce the number of sample galaxies with the consideration of the appropriate wavelength coverage of the ACS/G800L instrument (that is, 5500 to 10500 Å (Kümmel *et al.*, 2009)) for measuring the D4000 strength, which corresponds to the redshift range of $0.6 \lesssim z \lesssim 1.2$. This redshift range leaves 1050 galaxies out of 2923 galaxies.

Also, we consider the reliability of our D4000 measurements in our sample selection. First, we removed unphysically extreme values of D4000 measurements such as those within the range of D4000 < 0.5 or D4000 > 2.5. These extreme D4000 ranges are unlikely to be generated by the associated constituent stellar populations of galaxies, considering stellar population analysis (Bruzual A., 1983; Hamilton, 1985; Kauffmann *et al.*, 2003a). The exclusion of these extreme, unphysical D4000 galaxies removes 20 galaxies out of 1,050 galaxies, leaving 1030 galaxies.

Additionally, we adopt the error of D4000 measurements derived in Section 2.4.1 in order to select galaxies with only moderate error of D4000 measurements. We apply the relative error cut of D4000 measurements to be smaller than 0.5. That is, we require $\delta(\mathrm{D4000})/\mathrm{D4000} < 0.5$. This relative error cut further removes 9 galaxies out of 1030 galaxies, leaving 996 galaxies.

[1] https://archive.stsci.edu/prepds/pears/

With the remaining 996 galaxies, we derive the stellar mass completeness for our sample of galaxies following the methodology of Pozzetti *et al.* (2010). The limiting stellar mass ($M_{\rm lim}$) is calculated based on the apparent magnitude of galaxies and the limiting magnitude of the observation data set. Since our analysis incorporates the four different catalogs (see Section 2.3 for details), the limiting magnitude for calculating the stellar mass completeness could in principle be complex. However, the morphology catalog of Kartaltepe *et al.* (2015) has selected their sample galaxies with *HST* WFC3/IR H band < 24.5. This is the most stringent cut among the input catalogs, and therefore *is* our limiting magnitude. The galaxy structural parameters and stellar mass catalogs (that is, van der Wel *et al.*, 2012; Santini *et al.*, 2015, respectively) have fainter H-band limits. The PEARS survey catalog is magnitude limited at $i < 26.5$, which is a substantially different wavelength, but we have checked that $H - i < 2$ would occur for a trivially small number of objects for our purposes.

As described in Pozzetti *et al.* (2010) and Huertas-Company *et al.* (2016), we first calculate the limiting stellar mass based on each object using the relation given as $\log(M_{\rm lim}/M_{\odot}) = \log(M_*/M_{\odot}) + 0.4(H - 24.5)$ where M_* and 24.5 indicate a stellar mass of a galaxy and the limiting magnitude of the observation data set, respectively. And then, we calculate the 90th percentile of the $M_{\rm lim}$ distribution in each redshift bin below which the 90 % of the $M_{\rm lim}$ lie. In this way, the derivation ensures that the stellar mass of our sample galaxies is complete at least up to 90 %.

We derive the 90th percentile of the $M_{\rm lim}$ distribution with only quiescent galaxies because they typically have higher mass-to-light ratios than star-forming galaxies and thus have a higher stellar mass completeness threshold than star-forming galaxies. For this derivation, we adopt the UVJ color-color criterion for selecting quiescent galaxies suggested by Williams *et al.* (2009) (their Equation 4) as follows:

$$(U - V) > 0.88 \times (V - J) + 0.49. \qquad [1.0 < z < 2.0] \tag{2.1}$$

With the quiescent galaxies selected by the UVJ criterion, the derived 90th percentile of the $M_{\rm lim}$ distribution within the redshift range $1.0 < z < 1.2$, which is the highest redshift range of our sample of galaxies, is $\log(M_*/M_\odot) = 9.44$. Our stellar mass completeness can be compared with that in Huertas-Company *et al.* (2016), where the same limiting magnitude in the H band (i.e., $H < 24.5$) and the same photometric catalog for the GOODS-South field (i.e., Guo *et al.*, 2013) are used. Their stellar mass completeness within the redshift range of $1.1 < z < 1.5$ is $\log(M_*/M_\odot) = 9.61$ for their 'All' sample galaxies, which shows reasonable agreement with our derived value of $\log(M_*/M_\odot) = 9.44$. This stellar mass completeness of $\log(M_*/M_\odot) = 9.44$ reduces our sample size from 996 to 379 galaxies.

Lastly, we apply the morphology classification for our sample of galaxies as described in Section 2.3.2. Of 379 galaxies, 86, 61, 133, and 72 galaxies are classified as spheroids, early-type disks, late-type disks, and irregulars, respectively. The remaining 27 galaxies do not belong to any of the four morphological types and thus, are excluded from our sample of galaxies. This last sample selection criterion leaves the final sample of 352 galaxies which will be analysed throughout this paper.

The number of sample galaxies in each sample selection criterion is summarized in Table 2.1. Also, examples of our sample of galaxies in each morphological type with their color-composite images and the PEARS Grism spectra are shown in Figure 2.1.

2.4.3 Comparison of Visually-Classified Morphology with Other Morphology Indicators

In this section, we compare the visually-classified morphology of our sample of galaxies with other widely-used non-parametric morphology indicators such as concentration index, asymmetry, and M_{20} (Bershady *et al.*, 2000; Conselice, 2003; Lotz *et al.*, 2004). For the comparison, we employ the concentration index, asymmetry,

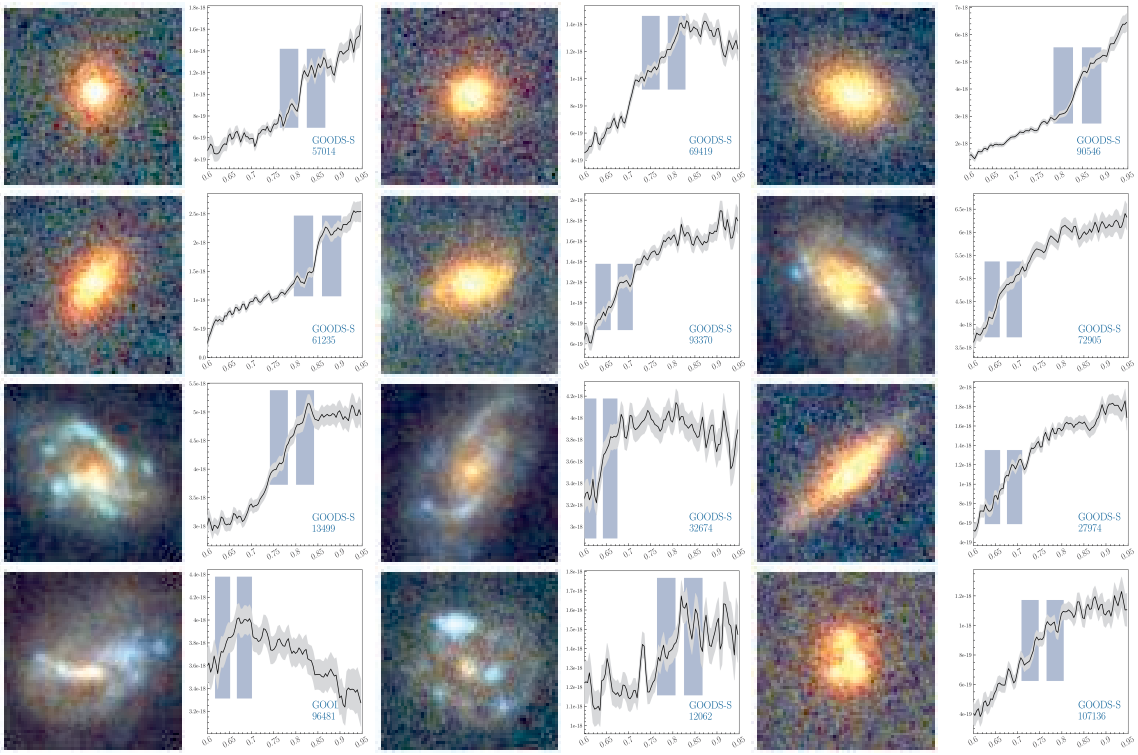

Figure 2.1: Examples of the ACS BVz filters color composite images (odd columns) and the corresponding PEARS grism spectra (even columns) of sample galaxies. All of the color composite images are 3″x 3″ sized. The wavelength range of the grism spectra is given in observed frame wavelength with the unit of µm. The unit of the flux of the grism spectra is given as erg $s^{-1}cm^{-2}$ Å . The black solid line is the observed spectrum and the grey-shaded area is the corresponding 1σ error. The two blue bands indicate the blue and red continua for D4000 measurement, respectively. The PEARS ID is marked on bottom right. Each row contains three randomly selected galaxies in each of the four morphological types. From top to bottom, visually classified spheroids, early-type disks, late-type disks, and irregulars are displayed. See Section 2.3.2 for further detail on the morphology classification scheme adopted in this study.

Table 2.1: Summary of Sample Selection

Criterion	Explanation (Number of galaxies)
Cross-matching the four catalogs[a]	Cross-matching radius of $0.05''$ (2923)
$0.6 \lesssim z \lesssim 1.2$	Redshift range for the D4000 measurement with the PEARS Grism data (1050)
$0.5 <$ D4000 < 2.5 & δ(D4000)/D4000 < 0.5[b]	Remove the poor measurements of D4000 (996)
$\log(M_*/M_\odot) > 9.44$	Stellar mass completeness (379)
Morphology classification -Spheroids (Sph) -Early-type Disks (E-D) -Late-type Disks (L-D) -Irregulars (Irr)	Remove 27 galaxies whose morphology classification does not belong to any of the four morphological types of Sph, E-D, L-D, and Irr (86, 61, 133, and 72, respectively)
Total	352

[a] The four catalogs used in this analysis. See Section 2.3 for details.

[b] The error of D4000 measurements derived as described in Section 2.4.1.

and M_{20} values measured by Ferreras *et al.* (2005, 2009) based on the HST/ACS i band. 62 galaxies among our final sample of 352 morphologically classified galaxies have been measured for concentration index, asymmetry, and M_{20} values from Ferreras *et al.* (2005, 2009).

The concentration index we employ here is defined as the ratio of the radius enclosing 80 % of the flux to that enclosing 20 % of the flux. The asymmetry is calculated using the squared-pixel values of residual images after an image of the galaxy is rotated by 180° about its center and subtracted from the original (unrotated) image. The asymmetry is applied with noise correction as well (see Conselice (2003) for further details). M_{20} is defined as the second-order moment of the brightest 20 % of the galaxy's flux, normalized by the total second-order moment of the galaxy's flux (Lotz *et al.*, 2004).

Figure 2.2 shows the correlations between the concentration index, asymmetry, M_{20}, and the visual morphology classification. Panel (a) shows the concentration index versus M_{20}, with the visual-inspection morphology color-coded. The black horizontal line of concentration index of 2.4 is the criterion that Ferreras *et al.* (2005) adopted for selecting their early-type candidates. The overall distribution of galaxies in panel (a) shows a positive correlation between the two morphology indicators of concentration index and M_{20}, as shown in previous studies (Lotz *et al.*, 2004; Ferreras *et al.*, 2005).

Figure 2.2 additionally shows how well the visual morphology we employ in this paper is correlated with concentration index, asymmetry, and M_{20}. The morphology distribution in panel (a) seems consistent with both concentration index and M_{20} distributions, such that all spheroids and $\sim$ 86 % of early-type disks (that is, 12 out of 14 galaxies) are located above the black horizontal line of concentration index of 2.4 along the positive correlation. The distributions of late-type disks and irregulars seem

broader than those of spheroids and early-type disks, ranging from low concentration index of $\sim$ 1.6 and high M_{20} of $\sim$ -1.0 to larger concentration index and lower M_{20} values similar to those of spheroids and early-type disks. These broader distributions of late-type disks and irregulars in concentration index vs. M_{20} seem to originate from their more complex galaxy structure (as compared to spheroids and early-type disks), which may include variously sized bulge components, diverse shapes of spiral arms, and so on.

Panel (b) shows the correlation between asymmetry and concentration index with the visual morphology. The two black solid lines are the demarcation lines for classifying galaxies into early, mid, and late types as suggested in Bershady *et al.* (2000). 2 of 14 early-type disks are removed in this panel because one of the two has an extremely large value of asymmetry (i.e., 1.194), and the other has a poorly measured asymmetry. Most spheroids (i.e., 9 of 11 galaxies) are located in the early or mid types regions having relatively small asymmetry values. However, early-type disks, late-type disks, and irregulars show broader distributions in the panel. Visual inspection of these early-type disks, late-type disks, and irregulars confirms that late-type disks and irregulars with larger asymmetry values (approximately larger than 0.3) tend to show more significantly disturbed features than those with smaller asymmetry values.

Overall, the visual morphology classification employed in this paper shows reasonable agreement with other widely-used morphology indicators such as concentration index, asymmetry, and M_{20} as explored in Figure 2.2.

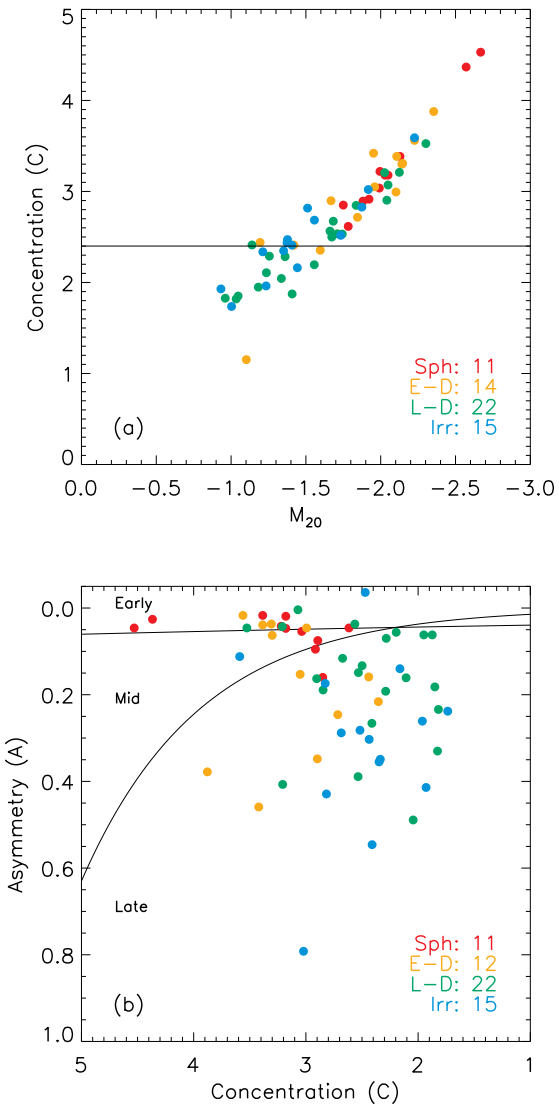

Figure 2.2: Comparison of visually classified morphology with other morphology indicators. (a) Concentration vs. M_{20} (Lotz *et al.*, 2004) for four morphological types color-coded. The morphological types and the number of galaxies in each type are marked in bottom right corner. The black solid horizontal line is the suggested line for selecting early-type candidates from Ferreras *et al.* (2005). (b) Asymmetry vs. Concentration for the same sample of galaxies as panel (a). The two black solid lines are the suggested lines for separating early, mid, and late-type galaxies from Bershady *et al.* (2000). The format is the same as panel (a).

2.5 Results

2.5.1 Morphology Distribution in the UVJ diagram with the D4000 Strength

There is a well-known correlation between galaxy morphology and their underlying stellar populations such that elliptical and S0 (i.e., early-type) galaxies consist of relatively old and metal rich stars, while spiral and irregular (i.e., late-type) galaxies consist of relatively young and metal-poor stars based on their luminosity-weighted ages and metallicity analysis (Oh *et al.*, 2013; Schawinski *et al.*, 2014; Alpaslan *et al.*, 2015; Khim *et al.*, 2015). The correlation between galaxy morphology and stellar properties of galaxies has thus suggested that the understanding of galaxy morphology is necessary in order to fully understand galaxy formation and evolution (see Conselice, 2014, for a review).

Both color-magnitude or color-color diagrams have been widely employed in numerous previous studies as ways to explore the stellar properties of galaxies photometrically (Sandage and Visvanathan, 1978; Bower *et al.*, 1992; Strateva *et al.*, 2001; Blanton *et al.*, 2003; Driver *et al.*, 2006; Williams *et al.*, 2009). Among the diverse possible combinations of colors, we adopt the UVJ diagram in this section.

Figure 2.3 shows the UVJ diagram for our sample of galaxies. We marked the black lines for identifying photometrically-quiescent galaxies from Williams *et al.* (2009), where the degeneracy between dust-free quiescent galaxies and dust-obscured starburst galaxies is empirically broken. Taking advantage of having both galaxy morphology and the D4000 strength information, it is interesting to note that our analysis in the UVJ diagram is able to show how galaxy morphology and the photometric and spectroscopic properties of galaxies are correlated at intermediate redshifts (i.e., $0.6 \lesssim z \lesssim 1.2$), which is expected to shed some light on the understanding of star formation histories of galaxies along with their morphological properties.

We separately plot the UVJ diagram for the four morphological sub-samples described in section 2.3.2, namely, spheroids, early-type disks, late-type disks, and irregulars. We indicate their D4000 strengths in Figure 2.3 using point colors. First of all, a reasonable correlation between the optical colors of $U-V$ and $V-J$ and the D4000 strength is clearly shown for all morphological types, such that galaxies with redder optical colors mostly have larger D4000 strength. This correlation overall ranges from blue to red colors of $U-V$ and $V-J$ (i.e., approximately from 0.5 to 2.2 for $U-V$ and from 0.5 to 2.0 for $V-J$).

Panel (a) shows the UVJ diagram for *spheroids*. The majority of spheroids (i.e., 64 of 86 galaxies, 74 %) are within the region of quiescence (i.e., top-left region) defined with the black dotted line suggested by Williams *et al.* (2009) for the redshift range $0.5 < z < 1.0$, within which more than half of our sample (that is, 205 of 352 galaxies) of galaxies reside. A color sequence of quiescent spheroids with increasing both $U-V$ and $V-J$ colors in the quiescent region is noticeable. The quiescent sequence of 'red and dead' spheroids is apparently so tight that it seems reasonable to suggest another separation line for defining the region of quiescence in the UVJ diagram based on our sample of galaxies within the redshift range $0.6 \lesssim z \lesssim 1.2$. The suggested line is shown in red dashed line in each panel and is as follows:

$$(U-V) > 0.88 \times (V-J) + 0.79. \qquad [0.6 \lesssim z \lesssim 1.2] \tag{2.2}$$

The newly suggested line has basically the same slope as that in Williams *et al.* (2009), but has a 0.1 larger intercept in order to define the quiescent region more conservatively, mainly focusing on the tight quiescent sequence as shown in panel (a). The line is found to be well-correlated with the D4000 strength such that the average D4000 strength for quiescent spheroids defined with the new line is 1.60. In addition to the D4000 strength, the color evolutionary track with an exponentially

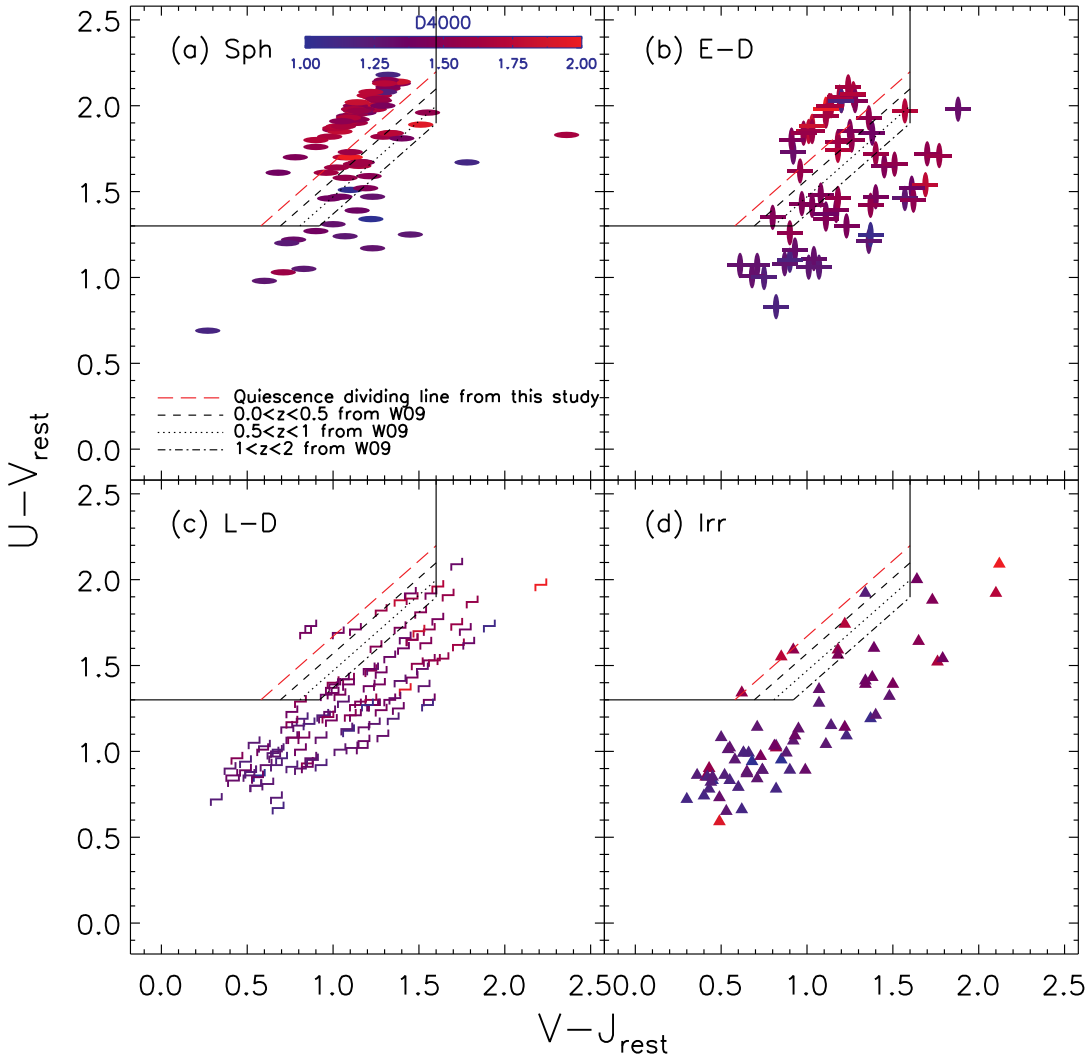

Figure 2.3: The UVJ diagram for different morphological types of galaxies with the D4000 strength color-coded. From top left to bottom right, spheroids, early-type disks, late-type disks, and irregulars are shown. The black lines are the suggested lines from Williams *et al.* (2009) for separating photometrically star-forming galaxies and quiescent counterparts. The red dashed line is the suggested line from this study for identifying both photometrically and spectroscopically red sequence galaxies in the UVJ diagram. Note the lack of late-type disks and irregulars above our suggested red dashed line.

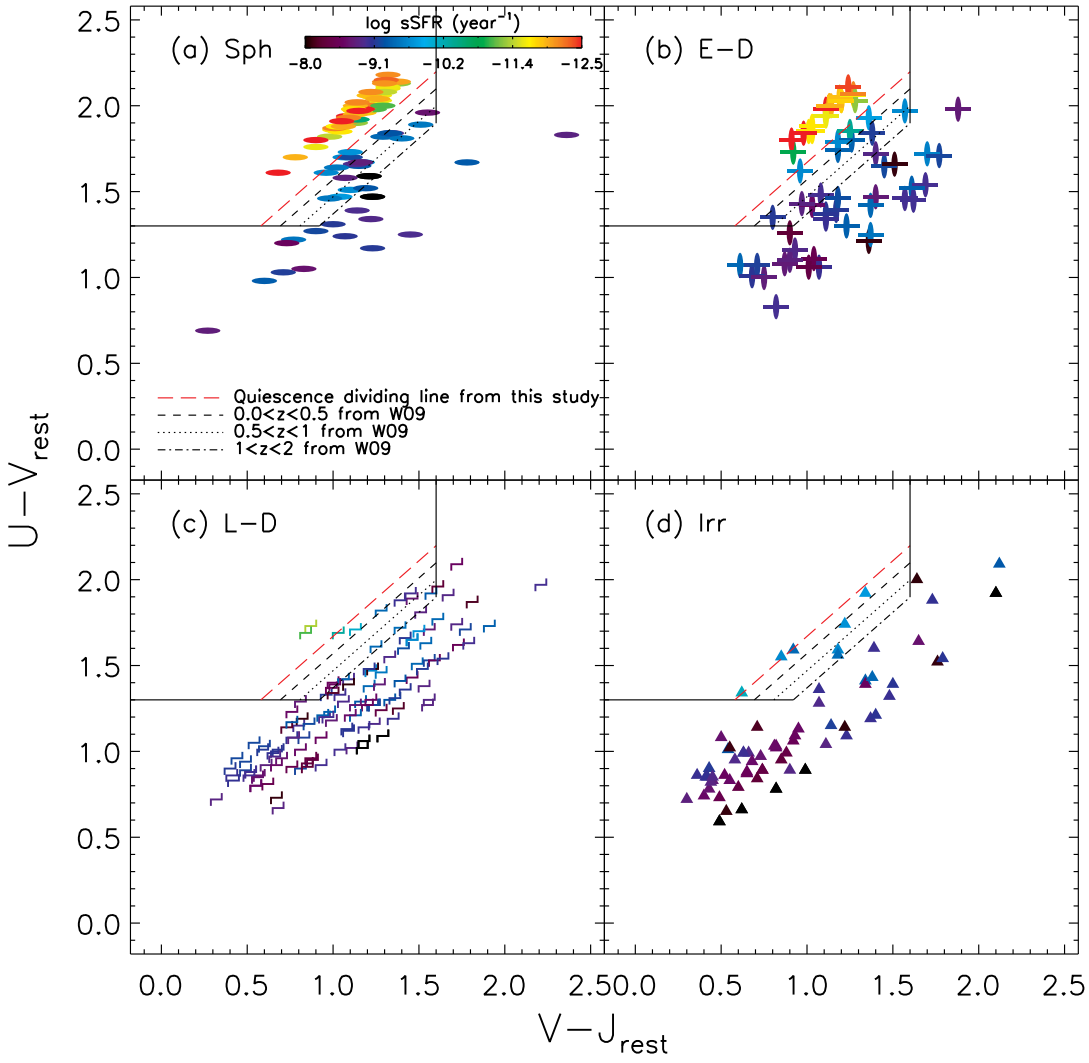

Figure 2.4: The same UVJ diagram as Figure 2.3, but with galaxy specific star formation rate (sSFR). Note that our newly suggested criterion (i.e., the red dashed line in each panel) for identifying optically quiescent galaxies based on the D4000 strength is qualitatively in good agreement with the distribution of sSFR. See the text for details.

declining star formation history with $\tau = 0.1$ Gyr in the UVJ diagram presented in Ownsworth *et al.* (2016) shows a close overlapping region with the red sequence of our spheroids. Moreover, the same UVJ diagram but with galaxy specific star formation rate (that is, SFR divided by stellar mass) in Figure 4.1 shows a qualitatively good agreement with the distribution of the D4000 strength. Given the overall large D4000 strengths, the close overlapping of the color evolutionary track with the stellar population model, and the qualitatively good agreement with the specific star formation rates, our newly suggested line seems to reasonably select the optically authentic 'red and dead' galaxies at intermediate redshifts based on their colors and the D4000 strength.

The sequence of quiescent spheroids is effectively the same sequence of quiescent galaxies identified in previous studies (Williams *et al.*, 2009; Whitaker *et al.*, 2011; Bell *et al.*, 2012; Muzzin *et al.*, 2013; Ownsworth *et al.*, 2016), while additionally showing their visually-identified morphological properties and spectroscopic properties represented by the D4000 strength. Considering the distributions of all other types of morphologies (i.e., *early-type disks*, *late-type disks*, and *irregulars* in panels (b), (c), and (d), respectively) in the UVJ diagram as well, it is interesting to note that the majority (i.e., 66 of 68 galaxies, $\sim 97\%$) of the quiescent galaxies defined with the red dashed line are bulge-dominated systems being classified as either spheroids or early-type disks. This strong correlation between the dominance of a bulge component and the quenching of star formation activities in galaxies is qualitatively in agreement with what has been known as the correlation between galaxy structure and star formation activities (Wuyts *et al.*, 2011; Bell *et al.*, 2012; Saintonge *et al.*, 2012; Bait *et al.*, 2017).

However, it is also clear that not all spheroids and early-type disks (i.e., the bulge-dominated systems) have fully quenched their star formation activities, as there exist

relatively blue (that is, $U-V \lesssim 1.3$ and $V-J \lesssim 1.0$) and weak D4000 strength (that is, D4000 $\lesssim 1.5$) spheroids and early-type disks. Those of not-quenched bulge-dominated systems are distributed from the blue colors of $U-V$ (~ 0.7) and $V-J$ (~ 0.5) to the locations just below the red sequence. Along with the gradual changes in their optical colors, their D4000 strength is increasing as well. These gradually increasing trends in both the UVJ colors and the D4000 strength are also seen in late-type disks and irregulars in panels (c) and (d), respectively. The gradual changes in the optical properties of galaxies seem to show the transitional sequence of galaxies from the 'blue cloud' to the 'red sequence' as shown in the color-magnitude (or stellar mass) relations in previous studies (Baldry *et al.*, 2004; Bell *et al.*, 2004; Schawinski *et al.*, 2014).

While there are photometrically and spectroscopically 'red and dead' quiescent galaxies in spheroids and early-type disks, few late-type disks and irregulars are within the region of quiescence defined with our suggested line (i.e., the red dashed lines in panels (c) and (d)). Only 2 of 133 late-type disks and none of 72 irregulars (1.5 % and 0 %, respectively) are within the quiescent region. Even if we consider the other quiescence lines (i.e., the black lines in the panels), the fraction of quiescent galaxies in late-type disks and irregulars is still low: 6.0 % of late-type disks and 6.9 % of irregulars would be classified as quiescent using the black dotted line, compared with 74% of spheroids and 43% of early-type disks. Although there are gradually increasing trends in the UVJ colors along with the D4000 strength from the 'blue cloud' to the 'red sequence' in late-type disks and irregulars, the lack of these bulgeless systems within the region of quiescence in the UVJ diagram seems to show again the close correlation between the galaxy structure and the quenching of star formation activities in galaxies, as mentioned earlier in this section.

2.5.2 The D4000 Strength vs. Stellar Mass and Stellar Surface Density with Morphologies

The D4000 strength of galaxies (or similarly, its narrower wavelength range version D_n4000; Balogh *et al.* (1999)) is a useful luminosity-weighted stellar population age indicator, as explained in Section 2.4.1. In particular, a D4000 strength of 1.5 generally corresponds to an average stellar population age of 1 Gyr, and thus the D4000 strength of 1.5 or a similar value has been used as a criterion for separating star-forming galaxies and quiescent galaxies (Kauffmann *et al.*, 2003a,b; Hathi *et al.*, 2009; Haines *et al.*, 2017).

We explore the correlations between the D4000 strength, stellar mass, the Sérsic index, and stellar surface density within the half-light radius for different subsets of our final sample, to check if these stellar property-related correlations show any dependence on morphological types.

Figure 2.5 shows the correlation between the D4000 strength and stellar mass for galaxies of each morphological type. The color indicates the Sérsic index, and the empty diamonds and the corresponding error bars indicate the median values and 1-σ standard deviations of D4000 strength distribution in each stellar mass bin, respectively. Panel (a) shows the distribution for spheroids. There is a moderately positive correlation between the D4000 strength and stellar mass, based on the overall distribution and the median values marked in the panel. The Pearson correlation coefficient (the associated p-value) is only 0.48 (0.00), although the value is slightly larger than the same correlation coefficient of 0.44 (0.00) for the total sample of galaxies, which is most likely attributed to the quality of the grism spectra and the vulnerability of the D4000 index to the possible outshining (i.e., luminosity-weighted "frosting") effect of small amount of young stellar populations in the majority of

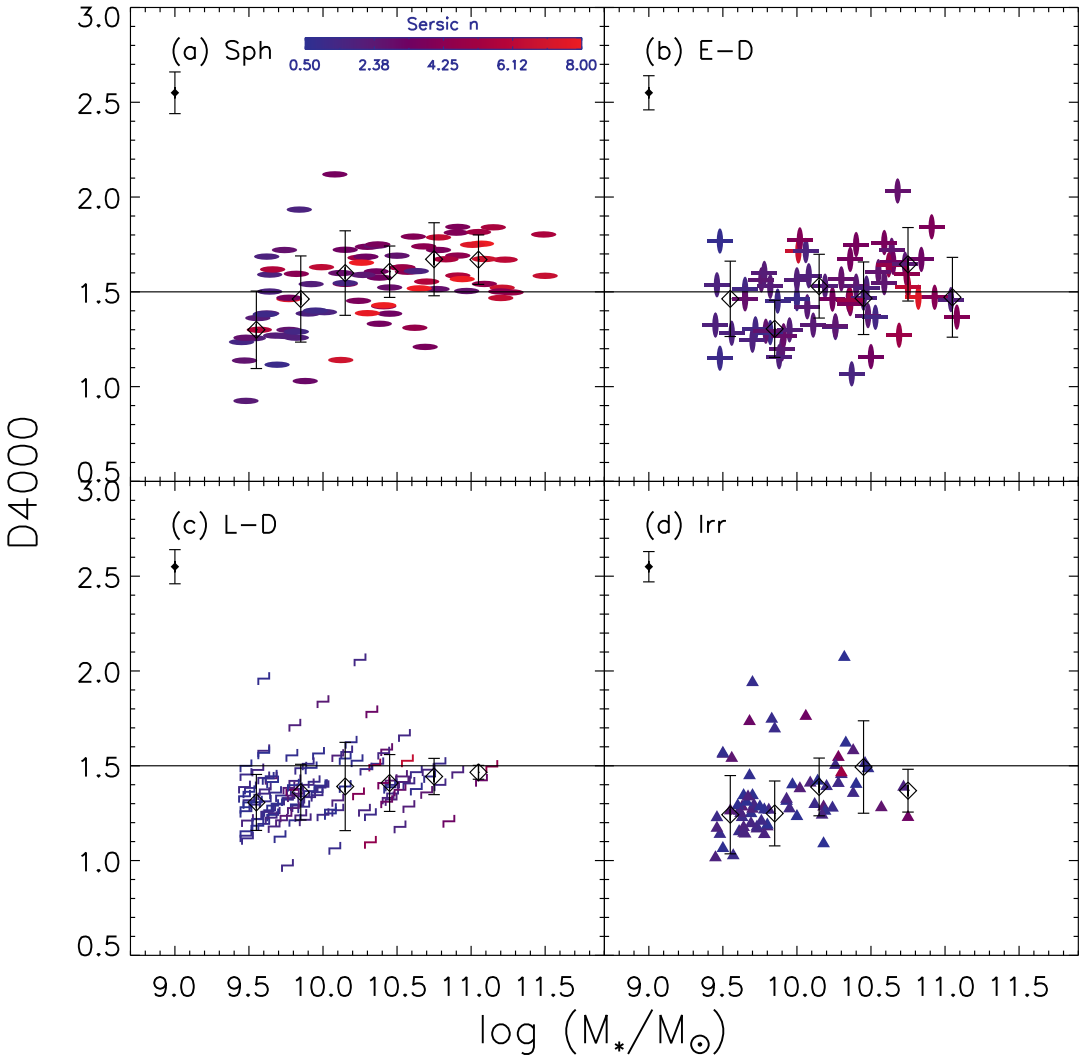

Figure 2.5: The D4000 strength vs. stellar mass with the Sérsic index color-coded. The format is the same as in Figure 2.3. The black-solid horizontal line is the D4000 strength of 1.5 for distinguishing spectroscopically star-forming galaxies (i.e., D4000 $<$ 1.5) and quiescent galaxies (i.e., D4000 $\geq$ 1.5). The empty diamonds are the running median values and the corresponding error bars show the 1σ standard deviations to indicate the population scatter. The typical measurement uncertainty in the D4000 strength for each morphological type is marked on top left of each panel.

relatively old stellar populations (see Trager *et al.* (2000); Hernán-Caballero *et al.* (2013) for further discussion on this). This increasing trend has similarly (but, with respect to the entire population of galaxies without morphology classification) been shown with the D_n4000 within similar redshift range in previous studies and has been discussed as one of the indicators for the "downsizing" scenario for the star formation histories of galaxies (Cowie *et al.*, 1996; De Lucia *et al.*, 2006; Hernán-Caballero *et al.*, 2013; Pacifici *et al.*, 2016; Haines *et al.*, 2017). Despite some overlapping of the 1σ standard deviations of the median values near the D4000 strength of 1.5, all of the median values for stellar mass bins greater than $\log(M_*/M_\odot) \gtrsim 10.0$ show the D4000 strengths greater than 1.5, suggesting that most of the moderately massive spheroids (i.e., $\log(M_*/M_\odot) \gtrsim 10.0$) observed at intermediate redshift (i.e., $0.6 \lesssim z \lesssim 1.2$) ceased forming stars at least 1 Gyr prior to the observed epoch. However, there are also some fraction of spheroids that show D4000 < 1.5. Those weak-D4000 spheroids tend to be less massive (i.e., $\log(M_*/M_\odot) \lesssim 10.0$). The fraction of strong D4000 galaxies in each mass bin for the four morphological types is summarized in Table 2.2. As in the table, 62.8 % of our sample of spheroids show strong D4000 strength.

The Sérsic index for each plotted galaxy is indicated by color in Figure 2.5, allowing examination of its dependence on D4000 strength and stellar mass. The distribution shows that massive (thus, likely large D4000 strength) spheroids tend to have larger values of Sérsic index, suggesting that massive spheroids have either centrally concentrated or extended light profiles, or both. We will discuss the Sérsic index distribution and the concentration of light profiles of galaxies in more details in Section 2.5.4.

The moderately positive correlations between the D4000 strength, stellar mass, and the Sérsic index shown in spheroids seem gradually weaker as the morphology of interest changes from spheroids to late-type disks. Panels (b) and (c) show the cor-

relations between the quantities in early-type disks and late-type disks, respectively. Early-type disks show 47.5 % of strong D4000 galaxies among them for the entire stellar mass range, which is 0.76 times that of spheroids (i.e., 62.8 %). However, the positive correlation between the D4000 strength and stellar mass is still visible based on the running median values (the empty diamonds) in panel (b), although the increasing trend is not as strong as in spheroids and the associated Pearson correlation coefficient (the associated p-value) is only 0.30 (0.02). Late-type disks in panel (c) show an interestingly and relatively flat trend between the D4000 strength and stellar mass, even up to a higher stellar mass regime, $\log(M_*/M_\odot) \sim 11.0$. The Pearson correlation coefficient (the associated p-value) for late-type disks is 0.25 (0.00). The running median values and the fraction of strong D4000 galaxies among late-type disks do not seem to show any strong indication of the positive correlation between the D4000 strength and stellar mass that is visible in spheroids. Only 16.5 % of late-type disks within the entire stellar mass range of interest have strong D4000 strength, which is 0.26 times that of spheroids.

Moreover, among the 16.5 % of late-type disks with strong D4000 (that is, 22 late-type disks as shown in Table 2.2), many may not actually be quenched. 15 of these 22 objects (i.e., 68 %) have an apparent axis ratio less than 0.5, suggesting that the strong D4000 strength in late-type disks is mainly caused by their inclination and the associated extinction. For instance, using the D4000 index with the stellar population synthesis models of Vazdekis *et al.* (2012) at solar metallicity, the effect of an E(B-V) = 0.2 mag attenuation results in a dust-free equivalent age change of 0.5 Gyr for a 1 Gyr old population, or an age change of 2 Gyr for a 3Gyr old population. Additionally, a test on the effect of E(B-V) on the measured value of the D4000 strength was performed. Specifically, we considered an intrinsic D4000 strength of 1.5 and applied the extinction law from Calzetti *et al.* (2000). For the case of color

excess E(B-V) of 0.2 mag attenuation, the intrinsic value of 1.5 was changed to 1.603, which is $\sim$ 7 % increase. For the case of color excess E(B-V) of 0.4 mag attenuation, the change is from 1.5 to 1.714, $\sim$ 14 % increase, and for the case of color excess E(B-V) of 0.6 mag attenuation, the change is from 1.5 to 1.832, $\sim$ 22 % increase. Therefore, the inclination effect on late-type disks seems to further reduce the fraction of authentically 'red and dead' late-type disks, corroborating that late-type disks do not get quenched and do not show a strong mass quenching at intermediate redshifts (i.e., $0.6 \lesssim z \lesssim 1.2$).

Panel (d) shows the correlations in irregulars. The Pearson correlation coefficient (the associated p-value) for irregulars is 0.31 (0.01). They show qualitatively similar trends that are shown in late-type disks in low stellar mass regime (that is, $\log(M_*/M_\odot) \lesssim 10.0$) such that most of low stellar mass irregulars (that is, approximately 83 % of the less massive irregulars based on Table 2.2) do not show strong D4000 strengths. These low stellar mass irregulars mainly show clumpy and ill-defined features such as asymmetric disks and non-spherical components at their centers based on their color-composite images, which is expected for them to be classified as irregulars. However, in the higher stellar mass regime (that is, $\log(M_*/M_\odot) \gtrsim 10.0$), the running median values of D4000 strength increase as stellar mass increases. This positive correlation between the D4000 strength and stellar mass is likely to be attributed to irregulars that have irregular features mainly due to galaxy interactions such as mergers and fly by, rather than typically clumpy star-forming irregulars. Visual inspection on the color-composite images of moderately massive irregulars (i.e., stellar mass larger than $\log(M_*/M_\odot) > 10.1$) shows that more than half of these massive irregulars have more than one of the visually-identifiable systems, suggestive of the likely interactions with other galaxies. Having the two distinctive types of irregulars in our morphology classification is presumably due to the fact that the classification

scheme adopted in our study for classifying irregulars does not distinguish between the typically clumpy star-forming irregulars and the galaxy interaction-driven irregulars (see Section 2.3.2 for details).

Regarding the correlation between D4000 strength and stellar mass, we additionally calculate the Kendall's Tau nonparametric correlation coefficient. The results of the correlation coefficient (the associated p-value) are 0.33 (0.00), 0.34 (0.00), 0.21 (0.02), 0.23 (0.00), and 0.31 (0.00) for the total sample galaxies, spheroids, early-type disks, late-type disks, and irregulars, respectively, which suggests that the overall trend shown in the Pearson correlation coefficients for the correlation is consistent with that shown in the Kendall's Tau nonparametric correlation coefficients.

The statistical significance on the Pearson correlation coefficients and the Kendall's Tau nonparametric correlation coefficients for the correlation between the D4000 strength and stellar mass is further checked by performing a bootstrap resampling in addition to the associated p-values. That is, we performed 1000 bootstrap resampling by shuffling the stellar masses while fixing the D4000 strengths within each morphological type and measured the correlation coefficients accordingly. From the 1000 bootstrap resampling results, the number of occurrences that the Pearson correlation coefficient from each bootstrap resampling is larger than the actually calculated value are 0, 0, 13, 2, and 4 for the total sample, spheroids, early-type disks, late-type disks, and irregulars, respectively. In case of the Kendall's Tau nonparametric correlation coefficient, the number of occurrences are 0, 0, 6, 0, and 0 in the same order of morphological type as the one for the Pearson correlation coefficient. In both correlation coefficients, the results from the bootstrap resampling test show the qualitatively similar trend to that shown in the associated p-values to the actually measured correlation coefficients and seem to suggest that the our computed correlation coefficients are not likely randomly obtained.

Another useful statistics for analysing the distributions of parameters of interest, the Cramér-von Mises statistics for the two-dimensional distribution of two samples (Anderson, 1962) with bootstrap resamples (hereafter, C-vM), is also performed for the correlation between the D4000 strength and stellar mass of two selected morphological types, which could show a morphological dependence on the "downsizing" trend. The hypothesis tested is whether "x is distributed as y" where x and y indicate two selected morphological types in this case. The results of the statistical test show that the hypothesis for all pairs of the two selected morphological types is rejected with the associated p-values of 0. The only exception when the hypothesis is confirmed is the case between spheroids and early-type disks with the associated p-value of 0.16, most likely originated from their close similarity of morphology. We will discuss the results of the statistical test in detail in Section 2.6.1.

Table 2.2: Fraction of strong D4000 galaxies in each morphological type (D4000 $\geq$ 1.5)

Mass range and Morphology	Spheroids	Early-type Disks	Late-type Disks	Irregulars
$9.44 \leq \log(M_*/M_\odot) < 9.9$	28 % (7/25)	37.5 % (6/16)	7.4 % (5/68)	17.1 % (7/41)
$9.9 \leq \log(M_*/M_\odot) < 10.3$	68.8 % (11/16)	40 % (6/15)	30 % (9/30)	15.8 % (2/19)
$10.3 \leq \log(M_*/M_\odot) < 10.7$	66.7 % (14/21)	57.1 % (12/21)	26.9 % (7/26)	40 % (3/10)
$10.7 \leq \log(M_*/M_\odot) < 11.1$	100 % (16/16)	55.6 % (5/9)	12.5 % (1/8)	0 % (0/2)
$11.1 \leq \log(M_*/M_\odot) \leq 11.5$	75 % (6/8)	0 galaxy	0 % (0/1)	0 galaxy
Total	62.8 % (54/86)	47.5 % (29/61)	16.5 % (22/133)	16.7 % (12/72)

It is also interesting to examine the correlations between the D4000 strength and stellar surface density as a function of morphology, since stellar surface density within the effective radius (Σ_e) or the central 1 kpc has been suggested to be associated with the quenching of star formation activities in galaxies (Bell and de Jong, 2000;

Kauffmann *et al.*, 2003b; Franx *et al.*, 2008; Bell *et al.*, 2012; Fang *et al.*, 2013; Omand *et al.*, 2014; Barro *et al.*, 2017; Williams *et al.*, 2017; Lee *et al.*, 2018).

Figure 2.6 shows the correlations between the D4000 strength, $\Sigma_{\rm e}$, and the Sérsic index that is color-coded in each data point, with separate panels for distinct morphological classes. $\Sigma_{\rm e}$ is derived adopting the widely employed formula: $\Sigma_{\rm e} = 0.5M_*/(\pi r_{\rm e}^2)$ where M_* is galaxy stellar mass in unit of solar mass, and $r_{\rm e}$ is the effective radius of galaxies in unit of kpc (Kauffmann *et al.*, 2003b; Franx *et al.*, 2008; Bell *et al.*, 2012). We employ the circular effective radius for calculating the $\Sigma_{\rm e}$ and the Kormendy relation in Section 2.5.5 by multiplying the semi-major axis effective radius by the square root of the axis ratio of galaxies.

Panel (a) shows the correlations between the parameters in spheroids. The surface density distribution approximately ranges from $10^{8.3}$ $M_\odot{\rm kpc}^{-2}$ to $10^{10.2}$ $M_\odot{\rm kpc}^{-2}$. A weakly positive correlation between the D4000 strength and the surface density is seen, based on the distribution and the running median values, although the median values do not dramatically increase with increasing surface density. We compute for this correlation a Pearson correlation coefficient and the resulting correlation coefficient (the associated p-value) is 0.24 (0.03). It is particularly interesting to compare the trend shown in the figure with the well-known sharp threshold in $\Sigma_{\rm e}$ over which galaxies suddenly become quiescent of their star formation activities (Brinchmann *et al.*, 2004; Franx *et al.*, 2008; Whitaker *et al.*, 2017; Williams *et al.*, 2017). A threshold of $\Sigma_{\rm e}$ which varies depending on the redshift of interest roughly corresponds to 10^9 $M_\odot{\rm kpc}^{-2}$ at intermediate redshift (that is, the redshift range of interest in this study) (Whitaker *et al.*, 2017). Indeed, our spheroids show a larger fraction of strong D4000 galaxies (D4000 $\geq$ 1.5) above the $\Sigma_{\rm e}$ of 10^9 $M_\odot{\rm kpc}^{-2}$, which is 80 % (39 out of 49 galaxies), compared to 41 % (15 out of 37 galaxies) for those below the $\Sigma_{\rm e}$ of 10^9 $M_\odot{\rm kpc}^{-2}$. The dramatic increase in the fraction of strong D4000 galaxies above the

Σ_e threshold is also seen in early-type disks in panel (b) with the fractions of 76 % (19 out of 25 galaxies) and 28 % (10 out of 36 galaxies) for galaxies above and below the Σ_e threshold, respectively. The Pearson correlation coefficient (the associated p-value) for early-type disks in panel (b) is 0.58 (0.00). For reference, the Pearson correlation coefficient (the associated p-value) for the total sample galaxies is 0.49 (0.00).

Therefore, our data support the hypothesis that Σ_e (or, similarly, the surface mass density in the central 1 kpc) is related to the quenching of star formation activities in galaxies as previously reported (Franx *et al.*, 2008; Omand *et al.*, 2014), suggesting the role of internal structure of galaxies in quenching of star formation activities.

What is shown in late-type disks and irregulars (i.e., panels (c) and (d), respectively) is that the two types of morphologies have very few galaxies whose Σ_e is larger than 10^9 $M_\odot$kpc^{-2}, compared to spheroids and early-type disks. That is, only 8 of 133 late-type disks (6 %) and 5 of 72 irregulars (7 %) have the Σ_e larger than 10^9 $M_\odot$kpc^{-2}, while spheroids and early-type disks show the fractions of 49 of 86 galaxies (57 %) and 25 of 61 galaxies (41 %), respectively. The running median D4000 values in late-type disks do not show noticeably significant increase with increasing Σ_e, although the associated Pearson correlation coefficient (the associated p-value) is 0.37 (0.00). The running median D4000 values in irregulars seem rather randomly distributed with some increases and decreases as the associated Pearson correlation coefficient (the associated p-value) of 0.22 (0.07) indicates. The lack of disk-dominated galaxies and irregular galaxies with $\Sigma_e \gtrsim 10^9$ $M_\odot$kpc^{-2} is most likely to be attributed to the star-forming disk or clumpy structures in late-type disks and irregulars that typically result in a larger effective radius and the subsequently smaller Σ_e at given stellar mass, compared to spheroids and early-type disks.

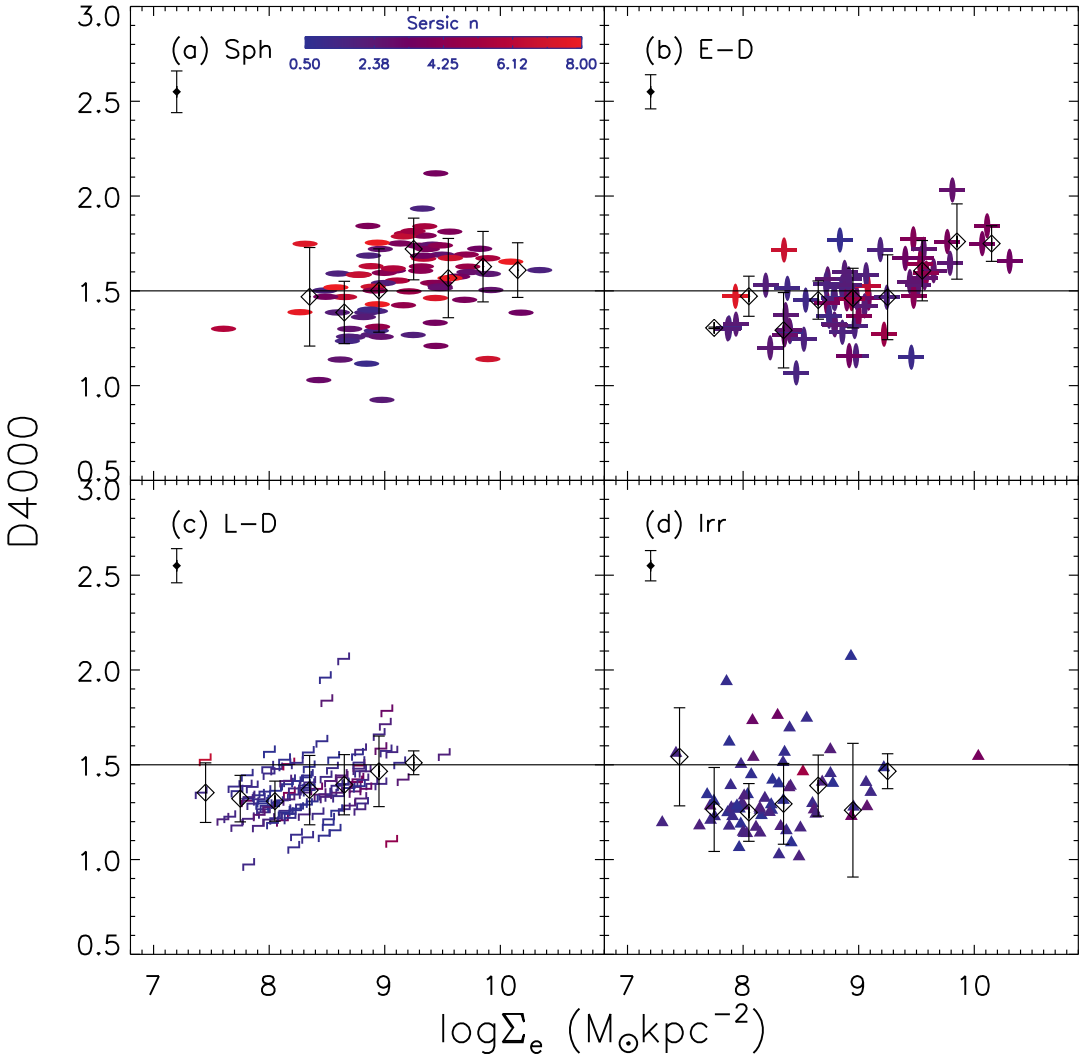

Figure 2.6: The D4000 break vs. stellar surface density within the half-light radius Σ_e, with the Sérsic index color-coded. The format is the same as Figure 2.5. Note the lack of late-type disks and irregulars with the stellar surface density larger than 10^9 $M_\odot$kpc^{-2}. See the text for details.

As performed for the correlation between the D4000 strength and stellar mass, we calculate the same Kendall's Tau nonparametric correlation coefficient for the correlation between the D4000 strength and Σ_e. The results of the correlation coefficient (the associated p-value) are 0.37 (0.00), 0.21 (0.00), 0.42 (0.00), 0.28 (0.00), and 0.15 (0.06) for the total sample galaxies, spheroids, early-type disks, late-type disks, and irregulars, respectively. The results suggest that the overall trend shown in the Pearson correlation coefficients for the correlation is consistent with that shown in the Kendall's Tau nonparametric correlation coefficient.

The same bootstrap resampling test as the one performed for the correlation between the D4000 strength and stellar mass to check statistical significance is performed for the correlation between the D4000 strength and Σ_e by shuffling Σ_e while fixing the D4000 strength within each morphological type. The results for the Pearson correlation coefficient are 0, 4, 0, 0, and 39 for the total sample, spheroids, early-type disks, late-type disks, and irregulars, respectively. The results for the Kendall's Tau nonparametric correlation coefficient are 0, 1, 0, 0, and 36 in the same order of morphological type as the one for the Pearson correlation coefficient. As in the correlation between the D4000 strength and stellar mass, the results from the bootstrap resampling test for the correlation between the D4000 strength and Σ_e also seem to suggest that our computed correlation coefficients are not likely randomly obtained.

The same C-vM test as the one performed for the correlation between the D4000 strength and stellar mass is also performed for the correlation between the D4000 strength and Σ_e. The results show that the hypothesis "x is distributed as y" is rejected for all pairs of the two selected morphological types, with the associated p-values of 0.02 for the case between spheroids and early-type disks and 0 for the other cases.

The Sérsic index distribution that is color-coded in each data point seems to behave as expected such that higher surface density galaxies tend to have higher values of the Sérsic index (Bell *et al.*, 2012). Further analysis of the surface density and the Sérsic index will be discussed in Section 2.5.4.

2.5.3 sSFR vs. Stellar Mass and Stellar Surface Density with Morphologies

The diagram of galaxy specific star formation rate (sSFR) versus stellar mass has often been employed to analyse the properties of stellar populations of the star-forming blue cloud, the quiescent red sequence, and the transient green valley galaxies (Noeske *et al.*, 2007; Ciambur *et al.*, 2013; Abramson *et al.*, 2014; Brennan *et al.*, 2015, 2017; Eales *et al.*, 2017; Pandya *et al.*, 2017). Along with this diagram, the correlation between sSFR and the Σ_e also has been investigated to find some link between star formation activities and internal structure of galaxies (Whitaker *et al.*, 2015, 2017; Williams *et al.*, 2017). (Similar relations using SFR in place of sSFR, and/or central surface density in place of effective-radius surface density, have similar applications.) In this section, we explore the sSFR versus stellar mass and the surface density within the effective radius with galaxy morphology in order to see if there is any morphological dependence on the locations of galaxies in the two diagrams.

Figure 2.7 shows the correlation between the sSFR and stellar mass for our sample of galaxies depending on their morphologies. The D4000 strength is color-coded in each data point. Panel (a) shows the correlation in spheroids. First of all, there is a clear bimodality between the star-forming spheroids and the quiescent spheroids with the separation sSFR of $\sim 10^{-10}\mathrm{yr}^{-1}$. A similar trend is seen in early-type disks in panel (b) as well. If we take the sSFR of $10^{-10}\mathrm{yr}^{-1}$ as an approximate separation criterion between the star-forming population and the quiescent population, the fractions of quiescent spheroids and early-type disks are 55.8 % (48 of 86 galaxies) and 31.1 %

(19 of 61 galaxies), respectively. These fractions are quantitatively in good agreement with those (i.e., 62.8 % and 47.5 %, respectively) derived by the fractions of strong D4000 galaxies in Table 2.2 with slightly higher fractions in the D4000 case. The similar fractions suggest the overall consistency between the photometrically-derived sSFR and the spectroscopically-derived D4000 strength. Other than the clear bimodality, the mass quenching trend is shown in bulge-dominated systems, such that the more massive galaxies are, the lower their sSFR is. Additionally, the presence of both star-forming bulge-dominated systems (i.e., either spheroids or early-type disks) and their quiescent counterparts in panels (a) and (b) (i.e., galaxies with sSFR $\gtrsim 10^{-10}\mathrm{yr}^{-1}$ and sSFR $\lesssim 10^{-10}\mathrm{yr}^{-1}$, respectively) is confirmed again, as previously shown in Figures 2.3, 4.1, 2.5, and 2.6. The distribution of the bimodality shown in Figure 2.7 is qualitatively consistent with those of Salimbeni *et al.* (2008) and Santini *et al.* (2009).

While spheroids and early-type disks show the overall mass quenching trend as well as the bimodality in the diagram of sSFR versus stellar mass, the distributions of late-type disks and irregulars (panels (b) and (c) in Figure 2.7, respectively) do not show a strong mass quenching trend or bimodality even up to the stellar mass of $\sim 10^{11} M_*/M_\odot$. In other words, there are only 4 of 133 (3.0 %) and 1 of 72 (1.4 %) quiescent (i.e., sSFR $\lesssim 10^{-10}\mathrm{yr}^{-1}$) late-type disks and irregulars, respectively throughout the stellar mass range considered in the figure (that is, stellar mass greater than $10^{9.44}\ M_*/M_\odot$). The remarkable lack of quiescent late-type disks and irregulars at intermediate redshift seems to confirm disk components or clumpy structures as the main drivers of global star formation activities in galaxies (Margalef-Bentabol *et al.*, 2018). This is further supported by the fact that the moderately massive (i.e., stellar mass greater than $10^{10}\ M_*/M_\odot$) star-forming (sSFR $\gtrsim 10^{-10}\mathrm{yr}^{-1}$) early-type disks still tend to show visually-identifiable blue star-forming disk components,

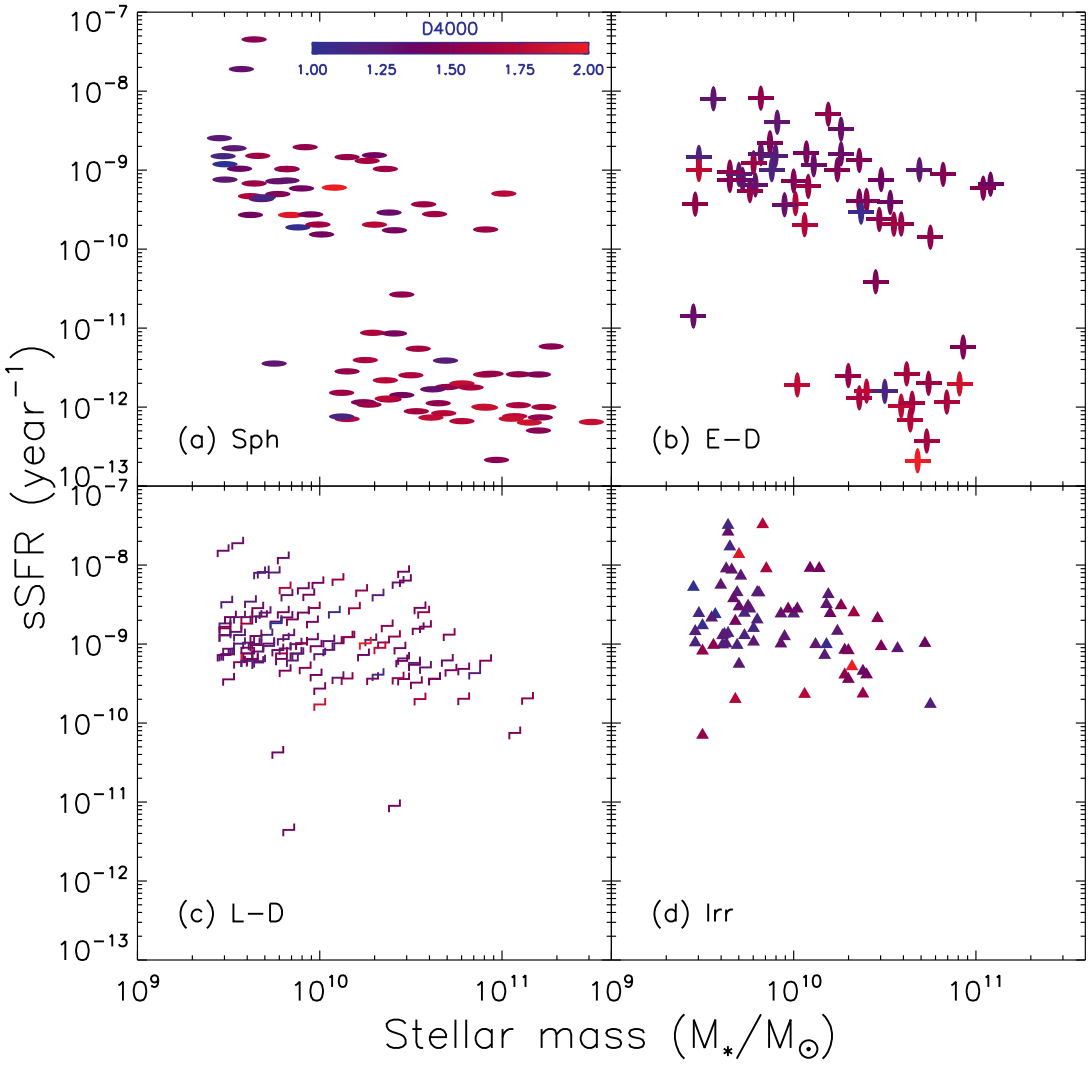

Figure 2.7: sSFR vs. stellar mass with the D4000 strength color-coded. The format is the same as Figure 2.3. Note that galaxies with a prominent bulge component (i.e., spheroids and early-type disks) are separated into two regions depending on their sSFR values, while most of late-type disks and irregulars do not show such remarkable separations. See the text for detail.

while their quiescent counterparts (i.e., sSFR $\lesssim 10^{-10}\mathrm{yr}^{-1}$) show almost spheroid-like morphologies without any visually-identifiable blue star-forming disk components. We checked the BVz filters color composite images of these early-type disks and noticed the morphological differences between the star-forming early-type disks and the quiescent early-type disks even within the same massive stellar mass range (that is, stellar mass greater than $10^{10}\ M_*/M_\odot$).

The results from the C-vM test for the correlation between sSFR and stellar mass indicate that the hypothesis "x is distributed as y" is rejected for all pairs of the two selected morphological types, with the associated p-values of 0.01 for the case between spheroids and early-type disks, 0.02 for the case between late-type disks and irregulars, and 0 for the other cases.

We also explore the morphological dependence on the star formation activities of galaxies in the same diagram, but for the surface density instead of stellar mass. Figure 2.8 shows the correlations between sSFR and Σ_e with the D4000 strength color-coded. As inferred from Figures 2.6 and 2.7, spheroids and early-type disks in panels (a) and (b), respectively show the bimodality such that there are star-forming and low Σ_e populations (i.e., sSFR $\gtrsim 10^{-10}\mathrm{yr}^{-1}$ and $\Sigma_\mathrm{e} \lesssim 10^9\ M_\odot\mathrm{kpc}^{-2}$) and quiescent and high Σ_e populations (i.e., sSFR $\lesssim 10^{-10}\mathrm{yr}^{-1}$ and $\Sigma_\mathrm{e} \gtrsim 10^9\ M_\odot\mathrm{kpc}^{-2}$). The separation between the star-forming galaxies and the quiescent galaxies at $\Sigma_\mathrm{e} \sim 10^9\ M_\odot\mathrm{kpc}^{-2}$ seems clear (e.g., Whitaker *et al.*, 2017), as discussed earlier in Section 2.5.2.

The distributions for late-type disks and irregulars in panels (c) and (d), respectively show that they do not have quiescent and high Σ_e galaxies (i.e., sSFR $\lesssim 10^{-10}\mathrm{yr}^{-1}$ and $\Sigma_\mathrm{e} \gtrsim 10^9\ M_\odot\mathrm{kpc}^{-2}$), unlike spheroids and early-type disks. The lack of quiescent and high Σ_e galaxies in late-type disks and irregulars seems to be attributed to star-forming disk components (or clumpy structures for irregulars) and the associated extendedly-measured effective radii that result in small Σ_e in the late-

type disks and irregulars.

The results from the C-vM test for the correlation between sSFR and Σ_e indicate that the hypothesis "x is distributed as y" is rejected for all pairs of the two selected morphological types, with the associated p-values of 0.01 for the cases between spheroids and early-type disks and between late-type disks and irregulars and 0 for the other cases.

At this point, we would like to remind that the overall sSFR distributions shown in Figures 2.7 and 2.8 are based on the sSFR derived by the multi-wavelength photometric bands SED fitting procedures, as mentioned earlier in Section 2.3.3. Regarding this, we note that the SED fitting-based SFR and the associated sSFR typically show larger uncertainties and have lower nominal values than the IR and UV flux-based SFR and the associated sSFR as previously discussed (Santini *et al.*, 2009, see their Figures 2 and 7).

Finally, we tested whether our conclusions depend on which stellar mass prescription we adopt among the several possibilities provided by Santini *et al.* (2015). We find that the trends shown in Figures 2.7 and 2.8 are robust to changes in stellar mass fitting procedure, although the bimodality at sSFR $\sim 10^{-10}\mathrm{yr}^{-1}$ shown in those figures can be less distinct for some of the other stellar mass models.

2.5.4 The Concentration of Light Profiles of Galaxies with Morphologies

The concentration of galaxies' light profiles may be related to their star formation activity. Galaxies with highly concentrated light profiles, as probed by the Sérsic index or central surface density, generally show the signatures of quenched star formation (Bell *et al.*, 2012; Cheung *et al.*, 2012; Barro *et al.*, 2017). This demonstrates the predictive power of the central surface density for quiescence (Whitaker *et al.*, 2017; Lee *et al.*, 2018).

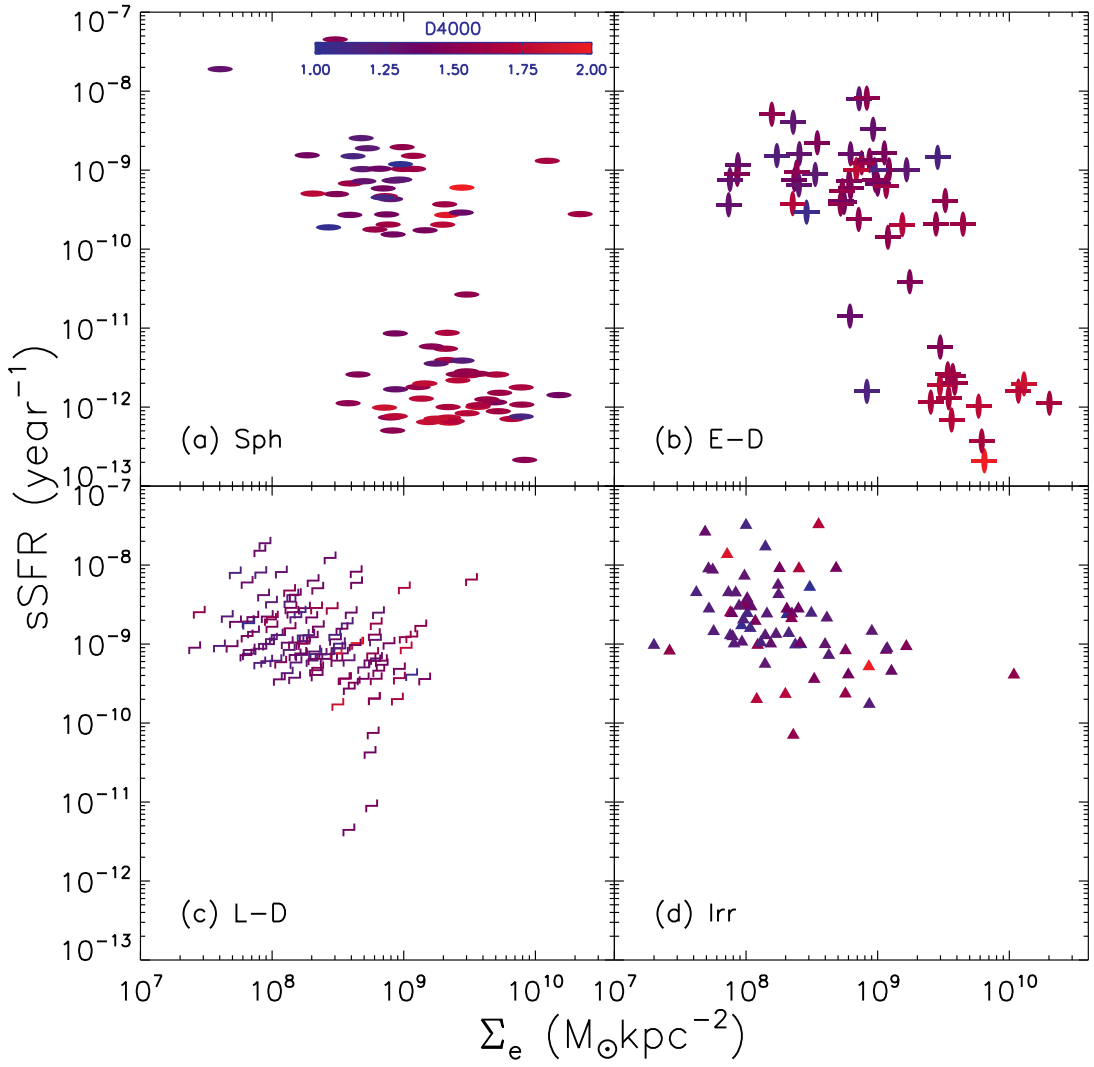

Figure 2.8: sSFR vs. Σ_e with the D4000 strength color-coded. The format is the same as in Figure 2.3. Note that most of the low sSFR galaxies (i.e., sSFR $< 10^{-10}$yr^{-1}) are bulge-dominated galaxies and have the surface density approximately greater than $10^9 M_\odot$kpc^{-2}, while the high sSFR galaxies (sSFR $\gtrsim 10^{-10}$yr^{-1}) in any morphological types mostly have the surface density smaller than $10^9 M_\odot$kpc^{-2}.

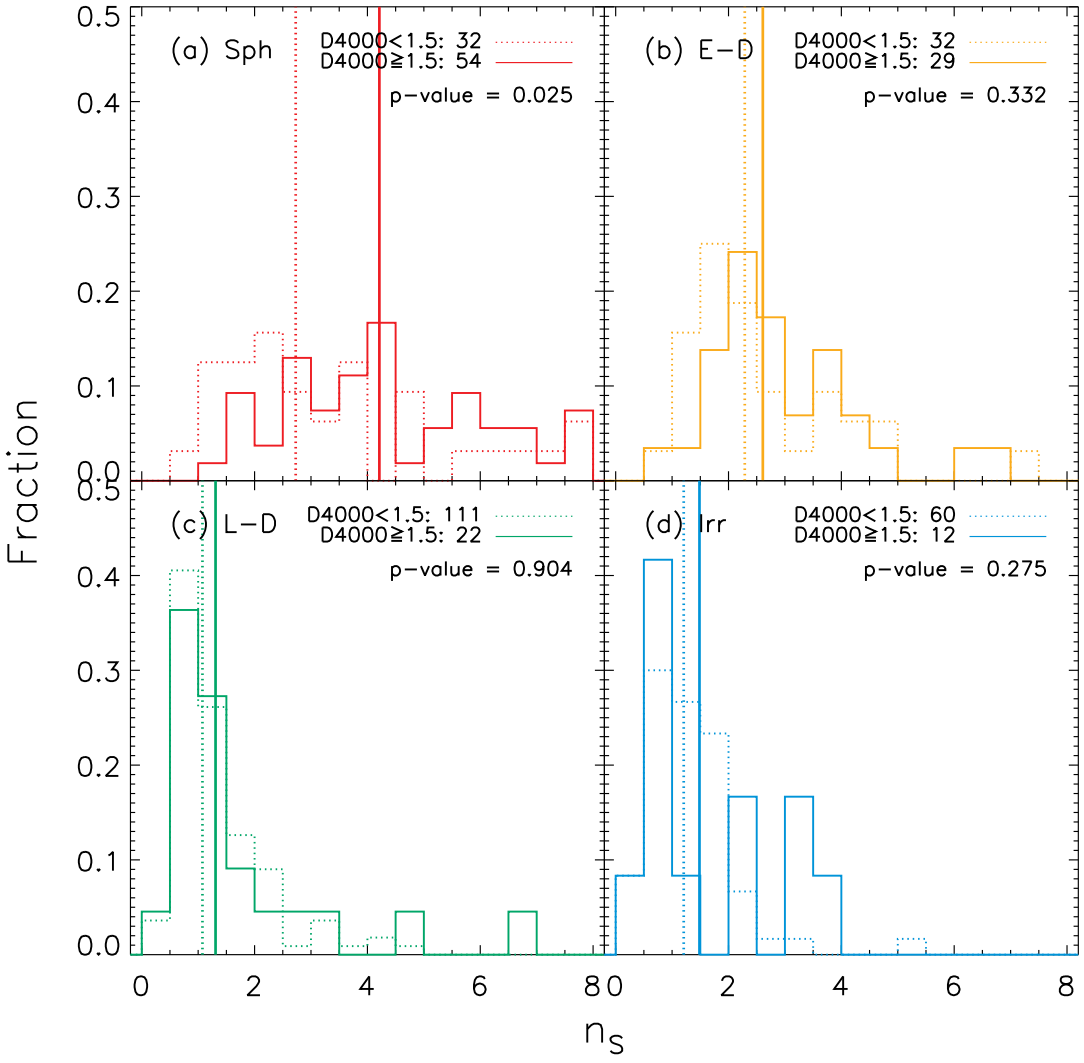

Figure 2.9: Sérsic index distribution for each of the four morphological types. From top left to bottom right, spheroids, early-type disks, late-type disks, and irregulars are displayed. In each panel, the dotted and solid lines correspond to the Sérsic index distribution for weak D4000 (i.e., D4000 < 1.5) and strong D4000 (i.e., D4000 ≥ 1.5) galaxies, respectively. The corresponding vertical lines indicate the median values of each D4000 strength group. The number of galaxies and the p-values from the K−S test are marked on top right of each panel. Note that the difference in distribution between the weak and strong D4000 strength groups is most significant in spheroids. The median value is n=4.21 for strong D4000 galaxies, while the median value for the weak D4000 counterparts is only n=2.73. However, a significant difference between weak and strong D4000 groups is not seen in other morphological types. See the text for details.

We explore a morphological dependence of the correlation between light profile concentration and star formation quiescence using the Sérsic index, Σ_e, and the D4000 strength of galaxies. Figure 2.9 shows the Sérsic index distributions for the four types of morphologies adopted in this paper. In each morphological type, we divide galaxies into star-forming and quiescent galaxies depending on their D4000 strength with the same criterion of D4000 of 1.5 as employed in Table 2.2. Panel (a) shows the distribution for spheroids.

We find that the star-forming spheroids tend to have lower Sérsic indices (the median value is 2.73), while the quiescent spheroids tend to have higher Sérsic indices (the median value is 4.21). Moreover, the difference is reasonably robust. A Kolmogorov−Smirnov (K−S) test comparing the Sérsic index distributions for the weak and strong D4000 distributions yields only a 2.5 % probability that such a large difference would be observed from intrinsically identical distributions.

While the difference in the Sérsic index distribution between the weak and strong D4000 spheroids seems significant, the difference becomes gradually weaker as the morphological type of interest goes from spheroids to late-type disks. The median Sérsic index values for weak and strong D4000 early-type disks are 2.29 and 2.61, respectively. The associated p-value is 0.332; i.e., there is a 33.2 % probability of observing a difference this large among two samples drawn from the same intrinsic distribution. For late-type disks, the median Sérsic indices for the weak and strong D4000 subsets are 1.08 and 1.31, a difference that is not statistically significant (with K-S test p-value of 0.904). Finally, irregulars have median Sérsic index values 1.21 and 1.49, for weak and strong D4000 subsets, with an associated K-S test p-value of 0.275. While this difference could be due to random chance, it is also consistent with the observation that the "irregular" galaxies are a mixed set including galaxies of different nature, as discussed earlier in Section 2.5.2 (i.e., star-forming clumpy

irregulars and galaxy interaction-driven irregulars).

The results from the Sérsic index distribution for each of morphological types are further confirmed when galaxies are plotted in the diagram of the Sérsic index versus Σ_e, which is shown in Figure 2.10 with the D4000 strength color-coded. In Figure 2.10, each morphological type is divided into the same weak and strong D4000 galaxies as in Figure 2.9. The median Sérsic index and Σ_e values of each of weak and strong D4000 galaxies are also marked with empty diamonds with blue and red 1σ standard deviation error bars, respectively. Spheroids in panel (a) show that not only the strong D4000 spheroids have typically higher Sérsic indices, but also they have larger Σ_e values, suggesting that the strong D4000 spheroids have more compact light profiles than the weak D4000 counterparts. A similar trend is seen in early-type disks but with a smaller difference in the Sérsic index distribution between the weak and strong D4000 early-type disks, compared to spheroids.

The noticeable correlation between the D4000 strength and compactness explored by the Sérsic index and Σ_e in spheroids and early-type disks does not seem to exist in late-type disks and irregulars, partly as expected from the analysis of Figure 2.9 for the Sérsic index distribution. Along with negligible differences in the Sérsic index distribution between weak and strong D4000 galaxies in late-type disks and irregulars (that is, the median Sérsic index differences of 0.23 and 0.28 between the weak and strong D4000 groups in late-type disks and irregulars, respectively), their Σ_e values show marginal differences between weak and strong D4000 galaxies as well. That is, late-type disks and irregulars have the median $\log(\Sigma_e)$ value differences of 0.48 and 0.2, respectively, suggesting a marginal correlation between compactness and quenching in late-type disks and irregulars.

Overall, what is shown in Figures 2.9 and 2.10 is a morphological dependence on the observed correlations such that bulge-dominated systems (that is, spheroids and

early-type disks) have noticeably positive correlation, while disk or clumpy structure-dominated systems do not, implying that galaxies need to experience morphological transformations to bulge-dominated systems for them to follow the observed positive correlation between quenching and compactness of galaxies as shown in Figures 2.9 and 2.10.

2.5.5 The Kormendy Relation for Spheorids

In this section, we explore the Kormendy relation for our sample of spheroids. This scaling relation has been widely employed in order to study structural properties of early-type galaxies and spheroidal components of late-type galaxies and the associated formation and evolution mechanisms (Kormendy, 1977; Bernardi *et al.*, 2003a; La Barbera *et al.*, 2003; Ferreras *et al.*, 2005; Longhetti *et al.*, 2007; Gadotti, 2009; Fisher and Drory, 2010; Kim *et al.*, 2016).

The top panel in Figure 2.11 shows the Kormendy relation for our sample of spheroids with the D4000 strength color-coded. We adopted the same circular effective radius calculated in Section 2.5.2 and the same mean surface brightness as defined in Bernardi *et al.* (2003b). Also, we corrected for the cosmological dimming $(1+z)^4$ to our sample of spheroids and 9 early-type galaxies at $1.2 < z < 1.7$ that are shown as the empty diamonds in the panel from Longhetti *et al.* (2007). Our spheroids seem to follow the general scaling relation based on the comparison to the 9 early-type galaxies and the fit through the maximum likelihood analysis (the black dashed line in the panel) to $\sim$ 9,000 early-type galaxies at $0.01 < z < 0.3$ in the Sloan Digital Sky Survey (SDSS) from Bernardi *et al.* (2003a). We particularly refer to the fit in the SDSS i-band because the bandpass of the i-band at low redshifts closely traces the bandpass of the H-band at intermediate redshifts for our sample of spheroids (that is, the median redshift of our sample spheroids is 0.94). We performed

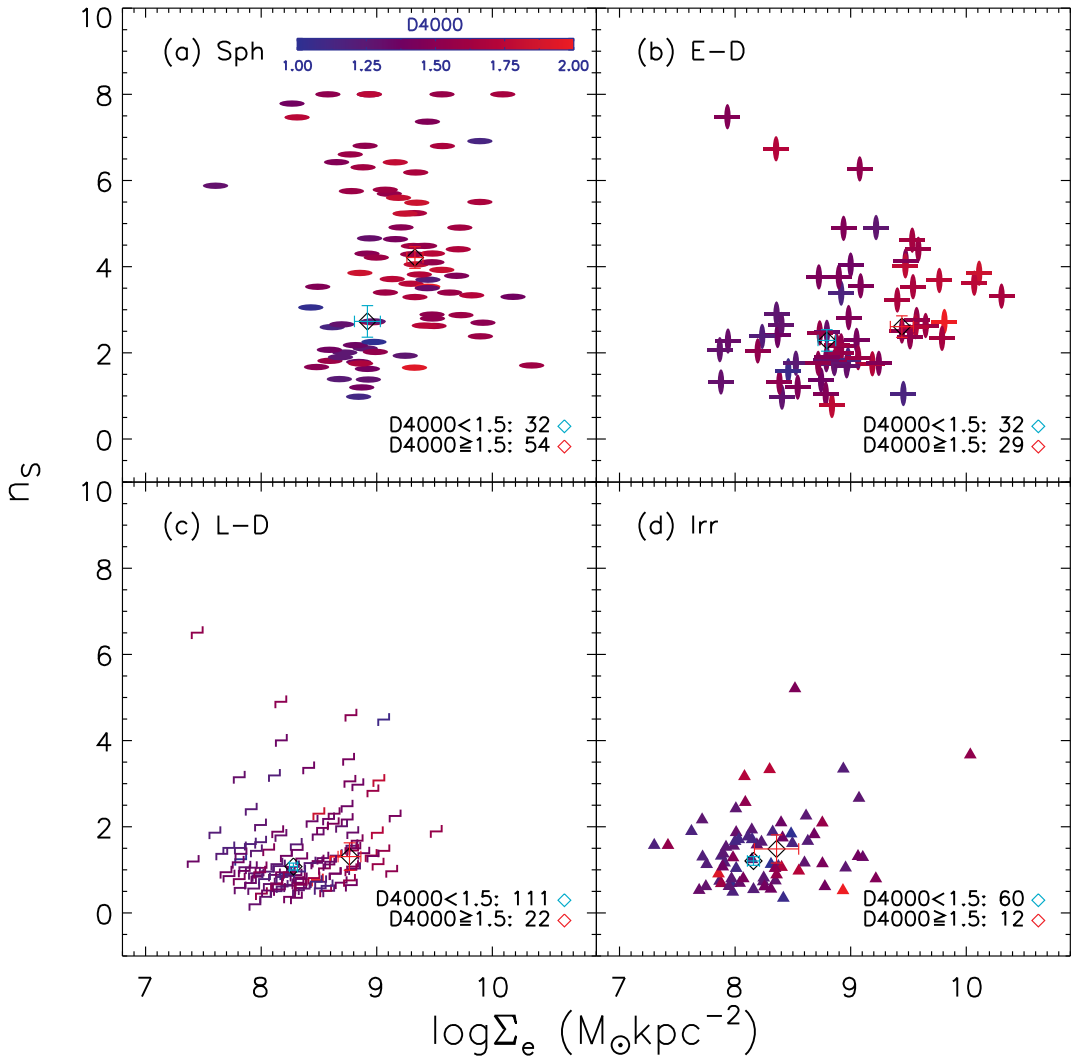

Figure 2.10: Sérsic index vs. Stellar surface density within the half-light radius, with the D4000 strength color-coded. The format is the same as Figure 2.5. The two diamonds with blue and red error bars in each panel are the median values for weak and strong D4000 galaxies, respectively. The corresponding error bars indicate the errors of the means in each D4000 group of galaxies.

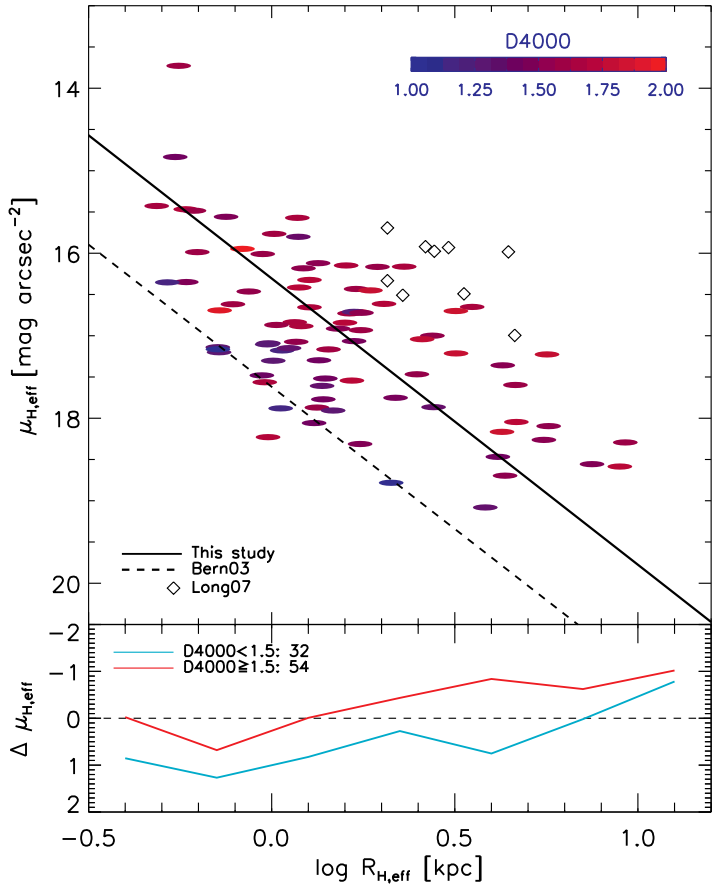

Figure 2.11: Top panel: the Kormendy relation for spheroids, with the D4000 strength color-coded. The color bar in top right indicates the D4000 strength. The black straight line is the linear fit to our sample of spheroids. The black dashed line is the Kormendy relation for relatively local (i.e., $0.01 < z < 0.3$) early-type galaxies derived in the SDSS i-band from (Bernardi *et al.*, 2003a, Bern03b). The empty diamonds are early-type galaxies at $1.2 < z < 1.7$ from (Longhetti *et al.*, 2007, Long07). All of the data points are corrected for the cosmological dimming $(1+z)^4$. Bottom panel: the fit residuals of spheroids to the Kormendy relation depending on their D4000 strength. Note that the weak D4000 strength spheroids tend to lie below the fitting line, while the strong D4000 strength spheroids tend to lie above the fitting line. See text for details.

a linear fit to our sample of spheroids and derived the following fitting relation:

$$\mu_{\rm H,eff} = (3.47 \pm 0.31)\log_{10} R_{\rm H,eff} + 16.31 \pm 0.11. \quad (2.3)$$

The slope of 3.47 ± 0.31 derived for our sample spheroids shows a comparable range with that of 3.29 ± 0.09 derived for the local early-type galaxies from Bernardi *et al.* (2003a) except for a larger uncertainty of the fit and a slightly steeper slope value.

Other than the general trend of the Kormendy relation shown in our sample of spheroids, we further check any dependence on the stellar properties of spheroids presented by the D4000 strength in this scaling relation. We divide the spheroids into weak and strong D4000 groups as in Section 2.5.4 and calculate the residuals of the surface brightness to the linear fit that is expressed in Equation 2.3. The residuals are shown in the bottom panel of Figure 2.11. As likely inferred from the top panel, at fixed effective radius the weak D4000 spheroids tend to have larger (fainter) surface brightness (luminosity) than the strong D4000 spheroids by ~ 0.8 mag, except for the large effective radius range (i.e., $\log R_{\rm H,eff} \gtrsim 0.6$) where the statistical trend for the weak and strong D4000 groups is not clearly seen mainly due to fewer number of sample spheroids.

If the difference in the residuals to the fitting line between the weak and strong D4000 groups primarily originated from the difference in their light profiles, a possible explanation for the trend shown in the weak D4000 spheroids lying below the fitting line and the strong D4000 spheroids lying above the fitting line in surface brightness is that the strong D4000 spheroids generally have more concentrated and dense stellar light profiles than the weak D4000 spheroids, resulting in smaller (brighter) surface brightness (luminosity) in the strong D4000 strength spheroids. This explanation is consistent with the results shown in Figures 2.9 and 2.10 where the same strong D4000 spheroids tend to have larger Sérsic index and $\Sigma_{\rm e}$ values.

Overall, the analysis performed in this section regarding the Kormendy relation for our sample of spheroids seems to support the idea that quenching of star formation activities is indeed related to the internal structure of galaxies (e.g., Bell *et al.*, 2012; Lang *et al.*, 2014, at least apparently in spheroids.).

2.6 Discussion

2.6.1 Morphological Dependence on the "Downsizing" Trend

Our main result is that there is a morphological dependence of the "downsizing" trend, such that galaxies with a prominent bulge component show a stronger mass quenching trend than galaxies without a prominent bulge component, even at a fixed stellar mass (i.e., Figures 2.5 and 2.7 and Table 2.2). This suggests that the 'mass' quenching is accelerated only after galaxies acquire a prominent bulge component. The acceleration of the mass quenching trend after the acquisition of a prominent bulge component in galaxies is likely to be due to either the role of a bulge component in preventing star formation activities, or the fading of a star-forming disk component, or both of the two effects working simultaneously.

Table 2.3: Mean p−values from the K−S tests for the pairs of the D4000 strength distributions between two selected morphological types.

Morphology	Spheroids	Early-type Disks	Late-type Disks	Irregulars
Spheroids	1.0	0.23 ± 0.21	$3.77 \times 10^{-6} \pm 3.00 \times 10^{-5}$	$4.81 \times 10^{-7} \pm 3.51 \times 10^{-6}$
Early-type disks	– [a]	1.0	0.006 ± 0.016	0.0003 ± 0.0014
Late-type disks	–	–	1.0	0.04 ± 0.08
Irregulars	–	–	–	1.0

[a] The '–' mark indicates that the corresponding value is already given in the symmetric column and row.

The role of a bulge component in preventing subsequent star formation activities in galaxies has been extensively discussed in previous studies (e.g., Dekel *et al.*, 2009; Saintonge *et al.*, 2012; Bluck *et al.*, 2014; Lang *et al.*, 2014; Tacchella *et al.*, 2015; Huertas-Company *et al.*, 2016) where the gravitational potential of a prominent bulge component can stabilize the gas disk, preventing the gas disk from forming stars. At least, the quenching mechanisms associated with the prominence of a bulge component seem to exist in our sample of galaxies as well, as most of our quenched galaxies are bulge-dominated systems as shown in Figure 2.3.

Additionally, the presence of star-forming blue spheroids among our sample (i.e., spheroids that are outside the quiescence region in the UVJ diagram of Figure 2.3 and have the D4000 strength less than 1.5) supports the idea that the emergence of a prominent bulge component precedes the departure from the star-forming populations (e.g., Lang *et al.*, 2014). The presence of blue spheroids at similar redshifts ($0.7 < z < 1.3$) has been also reported by Powell *et al.* (2017), where the most likely mechanism responsible for the formation of blue spheroids was mentioned to be major mergers of star-forming disk galaxies. If most blue spheroids indeed originated from major mergers of star-forming disk galaxies, it would be interesting to note that most blue spheroids are relatively low mass systems (i.e., $\log(M_*/M_\odot) \lesssim 10.0$). This is seen in Figure 2.5 and Table 2.2 for our sample of blue spheroids, and from Figure 7 for those in Powell *et al.* (2017). For these less massive systems, mergers that they might encounter would be likely to be major mergers for them (that is, merger mass ratio less than 4:1) due to their relatively low masses, which could possibly transform their morphologies into spheroids. Once they obtain a spheroidal morphology from the major mergers, the dominance of a bulge component-related quenching mechanisms such as gravitational stabilization of gas disks to prevent forming stars (e.g,. Martig *et al.*, 2009; Saintonge *et al.*, 2012) and the energetic active galactic nuclei (AGN)

feedback triggered by major mergers (e.g., Springel *et al.*, 2005; Hopkins *et al.*, 2007) would be likely to occur, turning blue spheroids into red and quiescent spheroids and accelerating their mass quenching trend likely along with the associated size-mass relation for quiescent galaxies.

However, we also note that there are additional mechanisms that could possibly contribute to the formation of blue spheroids other than major mergers of star-forming disk galaxies. For instance, the 'rejuvenation' of red spheroids by an external source could make the red spheroids blue again (e.g., Salim and Rich, 2010). In addition, environmental effect is one of the candidates that could contribute to the formation of blue spheroids (Lopes *et al.*, 2016). Although a single mechanism can not be pinned down for explaining the formation of blue spheroids (Tojeiro *et al.*, 2013), the tendency towards a high asymmetry index in blue spheroids reported by several studies (e.g., Lopes *et al.*, 2016; Powell *et al.*, 2017) seems to favor that most of blue spheroids come from merger-related mechanisms.

Late-type disks in our study, however, do not seem to show such a strong mass quenching trend as spheroids do (that is, Figure 2.5 and Table 2.2). The main reason for late-type disks not to show the strong mass quenching trend is likely the dominance of mostly star-forming disk components in them, at least at the redshift of interest (i.e., $0.6 \lesssim z \lesssim 1.2$). The blue (thus, star-forming) disk components might resist against the mass quenching trend while the parent galaxies continue to grow in mass, unless they experience significant changes in their evolutionary paths such as additional gas supply or major mergers that could disrupt their disk components and consequently turn them into bulge-dominated systems morphologically. The resistance of star-forming disk components against the mass quenching mechanism seems to be related to what is called 'slow quenching' where gas exhaustion in late-type galaxies occurs slowly over several Gyr. (e.g., Schawinski *et al.*, 2014). Assuming

that the 'slow quenching' mechanism also works for our sample of late-type disks, they are expected to evolve into either massive red late-type disks or early-type disks (in case they have grown their bulge components more efficiently) unless they have experienced abrupt changes.

Although further analysis such as environmental effects, AGN activity, and structural parameters from bulge−disk decomposition are required to draw firm conclusions on the evolution of late-type disks, what is seen in our results (e.g., Figure 2.5, Table 2.2, and Section 2.5.2) for them is that they do not tend to follow a strong mass quenching trend as bulge-dominated systems do, most likely due to the dominance of their star-forming disk components.

Lastly, we note that *some* quiescent late-type disks do exist in our sample, although they are a significantly smaller fraction of the population than their star-forming counterparts, as previously reported (e.g., McGrath *et al.*, 2008; Bell *et al.*, 2012). Using D4000 $\geq$ 1.5 as a criterion, there are 22 quiescent galaxies among 133 late-type disk galaxies (i.e., 16.5 %), as given in Table 2.2. Dust reddening can increase the D4000 measurements for late-type disks that are near edge-on viewing angles. If we use an axis ratio < 0.5 as a marker of edge-on geometry, and eliminate such inclined galaxies from our quiescent late-type disk sample, there are still 7 quiescent late-type disks (i.e., 5.3 % of the full late-type disk sample; see Section 2.5.2 for details). A similar fraction of late-type disks (4 of 133 galaxies, or 3.0 %) are identified as quiescent using the criterion sSFR $< 10^{-10}\mathrm{yr}^{-1}$. Regarding the possible mechanisms responsible for quiescent late-type disks, external processes such as environmental effects are often considered (e.g., Bassett *et al.*, 2013). Further analysis on environmental properties of quiescent late-type disks at intermediate redshifts is expected to shed some light on the formation mechanisms of these rare population of quiescent late-type disks.

While spheroids and late-type disks show distinct trends (including the mass quenching trend) in the correlations between stellar properties and galaxy structural properties explored in this study, early-type disks show intermediate trends that are between spheroids and late-type disks. This sounds obvious as the morphological selection of early-type disks is designed to do so, considering both the fractions $f_{\rm sph}$ and $f_{\rm disk}$ to be larger than 2/3 (see Section 2.3.2 for details). Regarding this, it is interesting to note that even among early-type disks there are visually-identifiable morphological differences between moderately massive star-forming (that is, $\log(M_*/M_\odot) > 10.0$ and sSFR $\gtrsim 10^{-10}\mathrm{yr}^{-1}$) and massive quiescent galaxies (that is, $\log(M_*/M_\odot) > 10.0$ and sSFR $< 10^{-10}\mathrm{yr}^{-1}$), as previously mentioned in Section 2.5.3. In other words, massive star-forming early-type disks tend to have blue star-forming disk components, while the massive quiescent counterparts show more spheroid-like morphologies. This trend seems to suggest that morphological transformations in early-type disks gradually occur from disk-dominant systems to bulge-dominated systems as they become older and more massive.

Irregulars in our study overall seem to show the well-known properties such as relatively young stellar populations that are revealed by their colors, D4000 strength, and sSFR distributions and low concentration of light profiles as shown in their Sérsic index and $\Sigma_{\rm e}$ distributions as previously reported (e.g., Oh *et al.*, 2013; Eales *et al.*, 2017). The mass quenching trend in irregulars does not seem significant, yet is slightly stronger in moderately high stellar mass regime (that is, $\log(M_*/M_\odot) \gtrsim 10.0$) than that in late-type disks based on the correlation between the D4000 strength and stellar mass in Figure 2.5 and Table 2.2. The slightly stronger mass quenching trend in irregulars in the moderately high stellar mass regime, however, is likely to be attributed to the presence of two different types of irregulars (i.e., typically young and star-forming clumpy irregulars and galaxy interaction-driven irregulars) in our

total sample of irregulars as discussed in Section 2.5.2, rather than their intrinsic "downsizing" trend.

Regarding the evolution of irregulars, the well-known sequence of average stellar properties (e.g., age and metallicity) of galaxies along the Hubble sequence detailed in the local Universe (e.g., Oh *et al.*, 2013; Khim *et al.*, 2015) and the decrease in the fraction of irregulars at least since $z \sim 2$ (Huertas-Company *et al.* (2016)) seem to suggest that the majority of irregulars have undergone morphological transformations from clumpy irregulars to structured late-type disks over time as long as they remain relatively undisturbed. Numerical simulations of the early evolution of disk galaxies performed by Noguchi (1999), for instance, show that clumpy structures in a galactic disk can evolve to organized bulge and disk components likely into be late-type disks.

Our discussion in this section on the morphological dependence on the "downsizing" trend is further supplemented by the p-values from the K−S test for the D4000 strength distributions between spheroids, early-type disks, late-type disks, and irregulars. The associated p-values are tabulated in Table 2.3. In order to confirm that the p-values derived from the pairs of the D4000 strength distributions among morphologies statistically exist, we performed 1,000 K−S tests by considering the D4000 measurement errors to be the Gaussian random errors each time. Therefore, the p-values shown in Table 2.3 are the mean p-values of the 1,000 different K−S tests, and the associated standard deviations are also given in the table. As shown in the table, it is interesting to note that all of the p-values are sufficiently low (that is, compared to the typically-employed p-value of 0.05) to suggest that the D4000 strength distributions (and thus, likely the overall age distributions of constituent stellar populations of galaxies) of the four morphological types are statistically different from one another. The only exception is the case between spheroids and early-type disks with the associated p-value of 0.23. The case between spheroids and early-type

disks is likely to be related to their morphological similarity of being bulge-dominated systems.

Although the results from the K-S test seem interesting by themselves, they should not be regarded as evidence for a morphological dependence on the "downsizing" trend because the K-S test does not consider the stellar mass distribution of each morphological type. Rather, the results from the C-vM test for the correlation between the D4000 strength and stellar mass shown in Section 2.5.2 could indicate the morphological dependence on the "downsizing" trend since the C-vM test considers both the D4000 strength and the stellar mass distributions simultaneously. Recalling the results from the C-vM test shown in Section 2.5.2, both results from the C-vM test and the K-S test show qualitatively similar trends, i.e., all pairs of the two selected morphological types show statistically different distributions except for the case between spheroids and early-type disks with the associated p-values of 0.16 and 0.23 for the C-vM test and the K-S test, respectively. If the morphological selection is the only criterion applied to separate galaxies into the four morphological types, the results from the C-vM test shown in Section 2.5.2 for the correlation between the D4000 strength and stellar mass would be a piece of supporting evidence for a morphological dependence on the "downsizing" trend indeed.

2.6.2 Morphological Dependence on Concentration of Light Profiles

As discussed in Sections through 2.5.2, 2.5.3, and 2.5.4, the concentration of galaxies' light profiles (as explored by the Sérsic index and Σ_e in this study, and often by the stellar surface density within the central 1 kpc in other works) is related to the stellar properties of galaxies. Quiescent galaxies tend to have more concentrated light profiles, indicating the predicting power of identifying quiescent galaxies through concentration (Franx *et al.*, 2008; Fang *et al.*, 2013; Omand *et al.*, 2014; Williams *et al.*,

2017).

Regarding the correlation between the concentration (equivalently, compactness) of light profiles of galaxies and quiescence, in addition to the possible physical mechanisms to explain the correlation, we also note that there is another possible explanation named the "progenitor effect" (Lilly and Carollo, 2016; Abramson and Morishita, 2018), which is somewhat of the "progenitor bias" (van Dokkum and Franx, 1996) in terms of selecting sample of galaxies over a span of cosmic time. This "progenitor effect" shows that the correlation between the central surface density and galaxy sSFR is naturally reproduced by assuming the evolution of the observed size-mass relation for star-forming galaxies and the appropriate mass-quenching trend (Peng *et al.*, 2010a; Carollo *et al.*, 2013), rather than invoking any physical link between the two parameters (that is, Figure 5 in Lilly and Carollo (2016)).

Although both the possible physical mechanisms and the "progenitor effect" can explain the strong correlation between the concentration of light profiles of galaxies and the quiescence, it is clear that most of quiescent galaxies (i.e., D4000 > 1.5) with high concentration (i.e., Sérsic index $\gtrsim 4$ and $\Sigma_{\rm e} \gtrsim 10^9\ M_{\odot}{\rm kpc}^{-2}$) are morphologically bulge-dominated systems in our study (Figures 2.6, 2.8, 2.9, and 2.10). Thus, it seems reasonable to assume that mechanisms responsible for higher concentration of light profiles are involved with visually-identifiable morphological transformations into bulge-dominated systems, likely either by the bulge growth or the fading of a disk component, or both effects working simultaneously.

In this regard, other than the discussion on the bulge growth in Section **??**, several studies mainly with low$-z$ ($0.03 < z < 0.11$) galaxy samples (e.g., Vulcani *et al.*, 2015; Carollo *et al.*, 2016) have suggested that the fading (or removal) of a disk component is the main cause for galaxies to be morphologically transformed into bulge-dominated systems, rather than the bulge growth itself. In particular, Carollo *et al.* (2016)

quantitatively demonstrated how the (either uniform or differential) fading of a disk component could make a bulge to total light ratio (B/T) increase without invoking actual bulge growth. (for instance, B/T can increase from 0.4 to 0.63 with the fading of a disk component by ~ 1 mag for an ordinary star-forming galaxy.)

Although our morphological analysis in this study alone cannot pin down which mechanism (that is, the bulge growth or the fading of a disk component) is more important than the other for morphological transformations into bulge-dominated systems, what is shown here is that the correlation between the concentration of light profiles of galaxies and the quiescence is involved with visually-identifiable morphological transformations of galaxies such that only bulge-dominated systems tend to have higher light concentration profiles with the signature of quiescence, since late-type disks and irregulars do not show such higher concentration of light profiles with the quiescence.

2.7 Summary

In this study, we have explored galaxy morphology and the associated stellar properties of galaxies in the redshift range $0.6 \lesssim z \lesssim 1.2$ by utilizing visual morphology, photometric, and spectroscopic information taken together. We have identified both spectroscopically and photometrically 'red and dead' galaxies in the UVJ diagram and further found that most (~ 97 %) of these quiescent galaxies are morphologically bulge-dominated systems.

Also, we have investigated a morphological dependence in the mass quenching trend in the diagram of the D4000 strength vs. stellar mass. In this diagram, we find a morphological dependence such that bulge-dominated systems show more significant mass quenching compared to disk-dominant systems within the same stellar mass range (i.e., Figure 2.5 and Table 2.2). This trend is most likely due to the dominance

of a blue star-forming disk component in late-type disks that would dilute the mass quenching trend compared to the bulge-dominated counterparts.

The correlations between the D4000 strength and galaxy structural parameters such as the Sérsic index and the stellar surface density within the effective radius (which is often considered to be related to the quiescence), $\Sigma_{\rm e}$, show that only some fraction of the bulge-dominated galaxies have large D4000 strength (D4000 > 1.5), $\Sigma_{\rm e}$ ($\Sigma_{\rm e} \gtrsim 10^9\ M_{\odot}{\rm kpc}^{-2}$), and Sérsic index (Sérsic index $\gtrsim 4$), indicating that not all of the bulge-dominated galaxies have high concentration light profiles with the signature of quiescence. On the other hand, the late-type disks and irregulars generally show neither such highly concentrated light profiles nor signatures of quiescence.

A morphological analysis on the correlations between sSFR, stellar mass, $\Sigma_{\rm e}$, and the Sérsic index basically shows qualitatively similar trends to those based on the D4000 strength. In particular, in the diagram of sSFR vs. stellar mass, bulge-dominated systems such as spheroids and early-type disks are clearly separated into the star-forming sequence and the quiescent sequence, while late-type disks and irregulars within the same stellar mass range considered have formed the star-forming sequence only, which is likely due to the star-forming disk or clumpy components in them.

The difference in the concentration of light profiles between weak and strong D4000 galaxies in each morphological type is shown to be the most significant in spheroids and the least significant in late-type disks (i.e., Figures 2.9 and 2.10). The Kormendy relation for spheroids further shows that at fixed effective radius strong D4000 spheroids tend to have smaller (brighter) surface brightness (luminosity) than weak D4000 counterparts by ~ 0.8 mag on average, suggesting more concentrated light profiles in strong D4000 strength spheroids at fixed effective radius. Although the correlation between the high concentration light profiles and the quiescence in

spheroids could be alternatively explained by the combination of the observed evolution of the size-mass relation for star-forming galaxies and the "progenitor" effect of quiescent populations (i.e., Lilly and Carollo, 2016), the morphological analysis regarding this correlation in our study suggests that most quiescent and centrally dense galaxies at intermediate redshifts at least have a visually-identifiable prominent bulge component and that none of late-type disks and irregulars show the high concentration light profiles with the signature of quiescence.

Taken together, our analysis of galaxy structure (including visual morphology) and stellar properties of galaxies through photometric and spectroscopic information as well as galaxy structural parameters indicates that physically-motivated quenching mechanisms are required to appropriately explain the morphological behavior shown in the various diagrams explored in this study. Observationally, future studies with significantly larger sample of galaxies are expected to enable us to better understand the morphology-entangled galaxy properties and the associated quenching mechanisms at intermediate redshifts statistically. All in all, our findings suggest a morphological dependence of the downsizing trend, and a tight correlation between quenching and the presence of a prominent bulge component, such that most of quenched galaxies at intermediate redshifts are bulge-dominated systems.

Chapter 3

THE IMPORTANCE OF STAR FORMATION INTENSITY IN LYα ESCAPE FROM GREEN PEA GALAXIES AND LYMAN BREAK GALAXY ANALOGS

3.1 Abstract

We have studied ultraviolet images of 40 Green Pea galaxies and 15 local Lyman Break Galaxy Analogs to understand the relation between Lyα photon escape and central UV photometric properties. We measured star formation intensity (SFI, star formation rate per unit area) from the central 250 pc region ($S_{250\mathrm{pc}}$) using the Cosmic Origins Spectrograph near-ultraviolet images from the *Hubble Space Telescope*. The measured $S_{250\mathrm{pc}}$ of our sample Green Peas ranges from 2.3–46 $M_\odot$ yr^{-1} kpc^{-2}, with a geometric mean of $15 M_\odot$ yr^{-1} kpc^{-2} and a standard deviation of 0.266 dex, forming a relatively narrow distribution. The Lyman Break Galaxy Analogs show a similarly narrow distribution of $S_{250\mathrm{pc}}$ (0.271 dex), though with a larger mean of 28 $M_\odot$ yr^{-1} kpc^{-2}. We show that while the Lyα equivalent width (EW(Lyα)) and the Lyα escape fraction ($f_{esc}^{Ly\alpha}$) are not significantly correlated with the central SFI ($S_{250\mathrm{pc}}$), both are positively correlated with the ratio of surface brightness to galaxy stellar mass ($S_{250\mathrm{pc}}/M_{\mathrm{star}}$), with correlation coefficients (p-values) of 0.702 (1×10^{-8}) and 0.529 (5×10^{-4}) with EW(Lyα) and $f_{esc}^{Ly\alpha}$, respectively. These correlations suggest a scenario where intense central star formation can drive a galactic wind in galaxies with relatively shallow gravitational potential wells, thus clearing channels for the escape of Lyα photons. This chapter previously published as Kim et al. (2020).

3.2 Introduction

Green Pea galaxies are a class of local starburst galaxies that were discovered by the citizen science "Galaxy Zoo" project based on the Sloan Digital Sky Survey (SDSS) (Lintott *et al.*, 2008). As inferred from their nickname, their optical color is greenish due to their strong [OIII] emission line at their redshifts (i.e., $0.1 \lesssim z \lesssim 0.35$), and their morphology seen in SDSS images is mostly compact and unresolved (e.g., Cardamone *et al.*, 2009). Studies on Green Peas (GPs) have shown that they are low stellar mass ($8 \lesssim \log(M_{\rm star}/M_{\odot}) \lesssim 10$) and metal-poor galaxies for their stellar mass with typically low intrinsic extinction ($E(B-V) \lesssim 0.2$) and high [O III]/[O II] ratios, experiencing intense star formation activities (i.e., $10^{-7}{\rm yr}^{-1} \lesssim$ specific star formation rate (sSFR) $\lesssim 10^{-9}{\rm yr}^{-1}$) (e.g., Amorín *et al.*, 2010; Izotov *et al.*, 2011; Jaskot and Oey, 2013; Yang *et al.*, 2016, 2017a, and references therein). In particular, their UV properties have shown that majority of GPs are Lyα-emitters (LAEs) and some of which have been confirmed as Lyman-continuum (LyC) leakers (e.g., Henry *et al.*, 2015; Yang *et al.*, 2016, 2017a; Izotov *et al.*, 2016, 2018c; Orlitová *et al.*, 2018).

In the field of cosmology, LyC leakers are important possible contributors for reionizing the early Universe ($z > 6$). Therefore, in consideration of the associations between LAEs and LyC leakers (e.g., Verhamme *et al.*, 2015; de Barros *et al.*, 2016; Izotov *et al.*, 2016), searching for LAEs and understanding the Lyα escape mechanisms is of astrophysical interest (e.g., Ahn *et al.*, 2003; Verhamme *et al.*, 2006; Gronke and Dijkstra, 2016). An ideal approach for studying LAEs would be directly measuring their physical properties from observation (e.g., Dey *et al.*, 1998; Rhoads *et al.*, 2000; Gawiser *et al.*, 2007). However, since most of LAEs are observed at high redshift ($z \gtrsim 2$, e.g., Song *et al.*, 2014; Shibuya *et al.*, 2019, and reference therein), directly observing them has been challenging mainly due to their observed faintness

associated with redshift and the intervening intergalactic medium (IGM) absorption along the line of sight. In this regard, an alternative approach for studying high-z LAEs would be studying the physical properties of *local* analogs of high-z LAEs such as GPs (e.g., Izotov *et al.*, 2011; Yang *et al.*, 2016, 2017a).

Morphologically, it has been reported that LAEs are typically "compact", often with multiple clumps in the rest-frame UV continuum (i.e., the effective radius $R_{\rm eff}$ $\lesssim$ 1.5 kpc) over a wide range of redshift $0 \lesssim z \lesssim 6$ (e.g., Bond *et al.*, 2009; Malhotra *et al.*, 2012; Jiang *et al.*, 2013; Paulino-Afonso *et al.*, 2018; Shibuya *et al.*, 2019; Ritondale *et al.*, 2019, and references therein). While there is an overall consensus regarding the compact and clumpy morphologies of most of LAEs studied, it does not seem entirely clear how these compact morphologies could be related to the observed Lyα profiles—and more fundamentally, whether the compact/clumpy morphology of Lyα-emitting galaxies is one of the important physical conditions that makes a galaxy a Lyα-emitting galaxy (e.g., Malhotra *et al.*, 2012; Izotov *et al.*, 2018a).

In this context, we investigate the central UV photometric properties of LAEs and continuum-selected Lyman Break Galaxy Analogs (LBAs), and the associations with the observed Lyα line properties based on GPs and local LBAs (i.e., Heckman *et al.*, 2005). We utilize the Cosmic Origins Spectrograph near-ultraviolet images (COS/NUV) acquisition images from the *Hubble Space Telescope* (*HST*) and the measured Lyα properties from the literature (i.e., Alexandroff et al. 2015; Yang et al. 2017, hereafter Y17). The physical proximity of our sample GPs and LBAs (i.e., $0.1 \lesssim z \lesssim 0.35$) and the high angular resolution (i.e., 0.0235 arcsec pixel^{-1}) of the COS/NUV images are suitable for studying the spatially-resolved central region properties of GPs and LBAs.

Section 3.3 describes our galaxy sample and the central star formation intensity measurements. In Section 3.4, we present our results. In Section 3.5, we discuss the

implications of these results and summarize our primary conclusions. Throughout this paper, we adopt the AB magnitude system and the ΛCDM cosmology of (H_0, Ω_m, Ω_Λ) = (70 kms^{-1} Mpc^{-1}, 0.3, 0.7).

3.3 Samples and Data Analysis

3.3.1 Green Pea and Lyman Break Galaxy Analog Sample

Our Green Pea sample is drawn from the 43 galaxies presented in Y17. As described in that paper, all of the galaxies have been observed with *HST*/COS spectroscopy and the associated NUV imaging through the COS acquisition mode ACQ/IMAGE with MIRRORA except for two galaxies (Green Pea ID 0021+0052 and 0938+5428) that have been observed with the MIRRORB configuration. We adopt additional information (e.g., Green Pea ID, equivalent width of the Lyα line EW(Lyα), Lyα escape fraction $f_{esc}^{Ly\alpha}$, and $E(B-V)$) for our sample Green Pea galaxies from Y17. Among the 43 galaxies, we exclude the two galaxies observed with the MIRRORB configuration in this study. We additionally exclude another galaxy (Green Pea ID 0747+2336) because the galaxy has no Lyα emission line detected in the COS spectroscopy observation (see Y17 for details). Therefore, our final Green Pea sample consists of 40 GPs.

The Lyman Break Galaxy Analog sample is drawn from 21 galaxies analyzed by Alexandroff *et al.* (2015). From the 21 galaxies, we only selected galaxies observed with the MIRRORA configuration, leaving 15 galaxies. LBA ID, galaxy stellar mass, and EW(Lyα) are adopted from Alexandroff *et al.* (2015). $E(B-V)$ value for the Milky Way extinction is obtained from the NASA/IPAC Galactic Dust Reddening and Extinction tool. Hα and Hβ fluxes for the Balmer decrement method to derive an internal extinction correction in Section 3.3.3 are obtained from the MPA-JHU

catalog (Brinchmann *et al.*, 2004; Tremonti *et al.*, 2004). We also note that 5 of the 15 LBA sample have been classified as GPs in Y17 (i.e., GP (LBA) ID 0055-0021 (J0055), 0926+4428 (J0926), 1025+3622 (J1025), 1428+1653 (J1428), and 1429+0643 (J1429)), and thus were already included in the 40 sample GPs. Therefore, the net increase in sample size is 10 additional objects classified as LBAs but not GPs. We note that any statistics quoted for the LBA sample include all 15 LBAs (both the 10 "pure" LBAs and the 5 overlap objects.)

For this combined sample of GPs and LBAs we use of the COS/NUV images to derive their central UV photometric properties. The exposure time of the images is typically greater than 100 seconds. The pivot wavelength of the observed NUV filter is 2319.7 $\mathring{A}$.

3.3.2 Deconvolution and Segmentation Maps

We derive segmentation maps of individual galaxies from the NUV images using an approach based on Haar wavelet decomposition. In order to compare the central properties of the entire sample without bias from redshift-dependent resolution effects, we first deconvolved raw NUV images of galaxies with the COS/NUV PSF image of star P330E taken during the *HST* program 11473 [1] . Specifically, we utilized the Python-based Richardson-Lucy deconvolution package [2] to perform the deconvolution.

We then proceeded with a Haar wavelet decomposition, which represents the galaxy image as a weighted sum of (mutually orthogonal) 2D boxcar functions. The denoising procedure discards terms in that sum whose coefficients are not significantly different from zero, given the noise in the data. Our Haar denoising procedure

[1] http : //www.stsci.edu/hst/cos/documents/isrs/ISR2010_10.pdf

[2] https : //scikit-image.org/docs/dev/api/skimage.restoration.html #skimage.restoration.richardson_lucy

[3] is a 2d generalization of the 1D TIPSH algorithm that Kolaczyk (1997) originally developed for modelling transient light curves.

We also estimated the sky background and subtracted from the processed (i.e., PSF-deconvolved and Haar wavelet denoised) COS/NUV images. The sky is measured by taking the average background values from the four 50×50 pixel corner regions of the 200×200 pixel ($4.7'' \times 4.7''$) galaxy images.

We then apply the Petrosian (1976) method to the processed and sky-subtracted images to derive the galaxy segmentation maps. The Petrosian method identifies the central region of a galaxy by defining a local surface brightness threshold $I_{\rm thresh}$ such that $I_{\rm thresh} = \eta \times \bar{I}(I > I_{\rm thresh})$. (That is, the threshold surface brightness is a factor of η below the average surface brightness enclosed within a contour having surface brightness $I_{\rm thresh}$. While $I_{\rm thresh}$ is implicitly defined, it is nevertheless a uniquely defined quantity for surface brightness profiles where both local surface brightness and total luminosity remain finite, as physics demands of real galaxies.) The $I_{\rm thresh}$ that satisfies the above Petrosian equation is found by sorting image pixels in descending surface brightness order, and thus the associated contour with $I_{\rm thresh}$ is not in general circular. This method has the advantages of being independent of the redshift of a galaxy, and relatively insensitive to dust reddening. We adopt $\eta = 0.2$, which is widely used for deriving galaxy segmentation maps (e.g., Shimasaku *et al.*, 2001). The derived segmentation maps of galaxies are used for measuring the total bolometric luminosity to compare with the central SFI in Section 3.4.1.

3.3.3 Star Formation Intensity Measurements from the Central 250 pc Region

We measure the star formation intensity (SFI, star formation rate per unit area which is equivalent to star formation rate surface density (SFRD)) from the central

[3] http : //butler.lab.asu.edu/wavelet_denoising

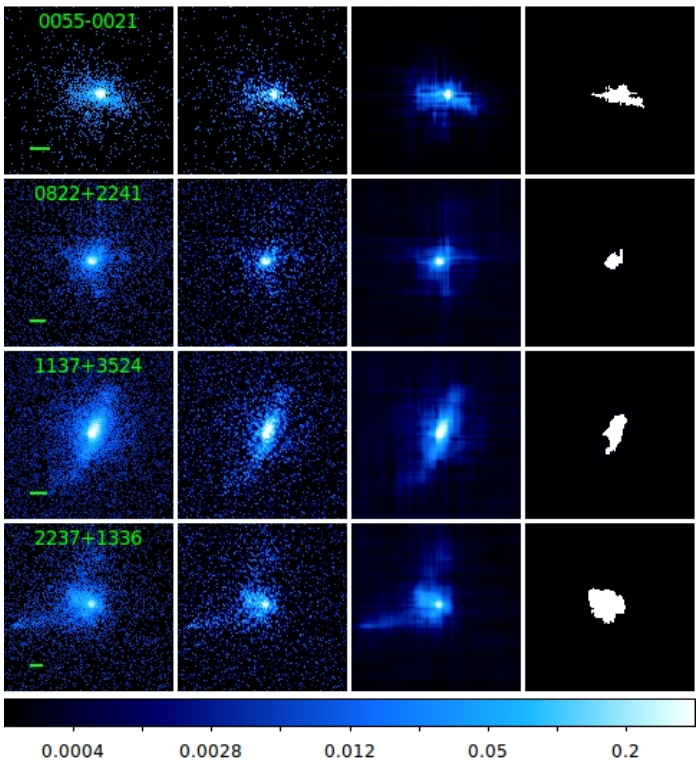

Figure 3.1: Examples of COS/NUV images of some Green Pea samples. Each row shows an individual Green Pea. From left to right, the raw NUV image, the PSF-deconvolved image, the Haar-denoised image, and the segmentation map are displayed, respectively. All images are $3'' \times 3''$ sized. Green Pea ID is marked top middle and a green bar indicates 1 kpc in the raw NUV image. The color bar at the bottom represents flux in the unit of count s^{-1}.

region of galaxies based on the UV surface brightness in the processed COS/NUV images described in Section 3.3.2. Our approach is similar to that employed in Meurer *et al.* (1997); Hathi *et al.* (2008); Malhotra *et al.* (2012).

We first apply extinction corrections and k-correction to estimate the intrinsic UV continuum flux measured at the same rest-frame wavelength for each galaxy. We apply the Milky Way extinction correction following the method of Fitzpatrick and Massa (1990) and Fitzpatrick (1999). We also perform an internal extinction correction adopting the Balmer decrement method and the extinction law from Calzetti *et al.* (2000). The k-correction is performed with respect to the mean rest-frame wavelength

of 1877.15 $\mathring{A}$ in the Green Pea sample. We adopt the intrinsic UV slope of -2 for typical starburst galaxies (e.g., Hathi *et al.*, 2008; Malhotra *et al.*, 2012). The galaxy center is set as the brightest pixel in the extinction and k-correction processed NUV images.

We then resample each image to a common pixel scale of 10 pc pixel^{-1}, using the IRAF "magnify" task with a redshift-dependent magnification factor. At this point, the images of our different sample galaxies have been processed to compensate for nonuniform properties introduced by distance (PSF deconvolution; pixel resampling), redshift (k-correction), and extinction (both foreground and internal).

We then measure the UV luminosity from the central 250×250 pc region ($L_{\rm bol,250pc}$ in the unit of $L_\odot$) together with the associated central SFI ($S_{\rm 250pc}$ in the unit of $L_\odot$ kpc^{-2}), by directly summing up the flux from 25×25 resampled pixels. We adopt the solar bolometric magnitude of 4.74 (Bessell *et al.*, 1998) and the UV to bolometric luminosity ratio ($L_{\rm UV}/L_{\rm bol}$) of 0.33 for typical starbursts (e.g., Meurer *et al.*, 1997; Hathi *et al.*, 2008). We also convert luminosities ($L_\odot$) into equivalent star formation rates ($M_\odot$ yr^{-1}) by using the scale factor $L_{\rm bol}/4.5 \times 10^9 L_\odot = {\rm SFR}/(1\, M_\odot\ {\rm yr}^{-1})$. This factor is derived by Meurer *et al.* (1997) based on starburst population modelling with a solar metallicity and a Salpeter (1955) IMF with lower and upper limit masses of 0.1 $M_\odot$ and 100 $M_\odot$ respectively.

Examples of raw NUV images, the deconvolved images, the Haar wavelet denoised images, and the derived segmentation maps of some sample galaxies are shown in Figure 3.1. Also, the measured $S_{\rm 250pc}$ and $L_{\rm bol,total}$ are provided in Table 3.1.

Table 3.1: The measured $S_{250\mathrm{pc}}$ and $L_{\mathrm{bol,total}}$, and adopted EW(Lyα) and $f_{esc}^{Ly\alpha}$ of Sample Galaxies

Green Pea ID[a]	SDSS ObjID[b]	log$S_{250\mathrm{pc}}$[c,d] ($L_\odot$ kpc^{-2})	log(SFI)[c,e] ($M_\odot$ yr^{-1} kpc^{-2})	log$L_{\mathrm{bol,total}}$[c,f] ($L_\odot$)	log(SFR)[c,g] ($M_\odot$ yr^{-1})	EW(Lyα)[h] ($\AA$)	$f_{esc}^{Ly\alpha}$[i]
0055-0021[j]	1237663783666581565	11.099 ± 0.100	1.445 ± 0.100	10.411 ± 0.171	0.757 ± 0.171	3.20	0.005
0303-0759	1237652900231053501	10.876 ± 0.025	1.223 ± 0.025	10.124 ± 0.054	0.470 ± 0.054	14.17	0.098
0339-0725	1237649961383493869	10.851 ± 0.050	1.198 ± 0.050	10.808 ± 0.083	1.155 ± 0.083	6.74	0.016
0749+3337	1237674366992646574	10.901 ± 0.054	1.247 ± 0.054	10.962 ± 0.105	1.310 ± 0.105	8.86	0.010
0751+1638	1237673807042708368	10.393 ± 0.075	0.740 ± 0.075	10.149 ± 0.149	0.496 ± 0.149	15.77	0.043
0805+0925	1237667729656905788	10.725 ± 0.077	1.071 ± 0.077	10.582 ± 0.141	0.929 ± 0.141	9.20	0.009
0815+2156	1237664668421849521	10.690 ± 0.017	1.036 ± 0.017	9.793 ± 0.035	0.139 ± 0.035	82.15	0.327
0822+2241	1237664092897083648	11.054 ± 0.038	1.401 ± 0.038	10.437 ± 0.076	0.784 ± 0.076	51.62	0.037
0911+1831	1237667429018697946	11.197 ± 0.017	1.543 ± 0.017	10.621 ± 0.033	0.968 ± 0.033	56.53	0.177
0917+3152	1237661382232768711	11.311 ± 0.032	1.658 ± 0.032	10.760 ± 0.045	1.107 ± 0.045	37.97	0.169
0925+1403[k]	1237671262812897597	11.042 ± 0.014	1.389 ± 0.014	10.500 ± 0.028	0.846 ± 0.028	90.01	0.186
0926+4428[j]	1237657630590107652	10.915 ± 0.080	1.262 ± 0.080	10.328 ± 0.115	0.675 ± 0.115	47.85	0.287
0927+1740	1237667536393142625	10.489 ± 0.071	0.835 ± 0.071	10.479 ± 0.126	0.826 ± 0.126	7.20	0.013
1009+2916	1237665126921011548	10.470 ± 0.047	0.817 ± 0.047	9.884 ± 0.078	0.230 ± 0.078	69.54	0.373
1018+4106	1237661851459584247	10.557 ± 0.045	0.904 ± 0.045	10.101 ± 0.104	0.457 ± 0.104	33.05	0.059
1025+3622[j]	1237664668435677291	10.780 ± 0.048	1.126 ± 0.048	10.433 ± 0.096	0.779 ± 0.096	26.27	0.154
1032+2717	1237667211592794251	10.408 ± 0.064	0.755 ± 0.064	9.990 ± 0.108	0.337 ± 0.108	5.50	0.009
1054+5238	1237658801495474207	11.045 ± 0.034	1.392 ± 0.034	10.705 ± 0.053	1.052 ± 0.053	17.65	0.112
1122+6154	1237655464839479591	10.866 ± 0.033	1.213 ± 0.033	9.957 ± 0.057	0.304 ± 0.057	59.95	0.187
1133+6514	1237651067351073064	10.507 ± 0.030	0.854 ± 0.030	10.334 ± 0.060	0.681 ± 0.060	42.30	0.422
1137+3524	1237665129613885585	10.903 ± 0.029	1.250 ± 0.029	10.483 ± 0.059	0.829 ± 0.059	40.45	0.157
1152+3400[k]	1237665127467647162	10.961 ± 0.021	1.308 ± 0.021	10.671 ± 0.039	1.018 ± 0.039	74.45	0.287
1205+2620	1237667321644908846	10.942 ± 0.039	1.289 ± 0.039	10.422 ± 0.073	0.769 ± 0.073	3.00	0.006
1219+1526	1237661070336852109	10.897 ± 0.023	1.244 ± 0.023	10.243 ± 0.036	0.590 ± 0.036	164.55	0.702
1244+0216	1237671266571387104	10.697 ± 0.021	1.044 ± 0.021	10.558 ± 0.065	0.904 ± 0.065	46.98	0.077
1249+1234	1237661817096962164	10.749 ± 0.019	1.096 ± 0.019	10.404 ± 0.047	0.751 ± 0.047	101.82	0.412
1333+6246[k]	1237651249891967264	10.538 ± 0.017	0.885 ± 0.017	10.176 ± 0.047	0.523 ± 0.047	72.34	1.180
1339+1516	1237664292084318332	10.984 ± 0.037	1.331 ± 0.037	10.091 ± 0.054	0.438 ± 0.054	44.74	0.034
1424+4217	1237661360765730849	10.724 ± 0.033	1.071 ± 0.033	10.101 ± 0.069	0.448 ± 0.069	89.53	0.290
1428+1653[j]	1237668297680683015	11.192 ± 0.032	1.539 ± 0.032	10.761 ± 0.070	1.108 ± 0.070	29.07	0.106
1429+0643[j]	1237662268069511204	11.045 ± 0.073	1.392 ± 0.073	10.459 ± 0.094	0.806 ± 0.094	42.75	0.123
1440+4619	1237662301362978958	11.154 ± 0.040	1.501 ± 0.040	10.815 ± 0.068	1.162 ± 0.068	33.82	0.128
1442-0209[k]	1237655498671849789	11.124 ± 0.018	1.470 ± 0.018	10.416 ± 0.042	0.763 ± 0.042	134.90	0.430
1454+4528	1237662301900964026	11.118 ± 0.036	1.465 ± 0.036	10.496 ± 0.069	0.843 ± 0.069	29.95	0.061
1457+2232	1237665549967294628	10.804 ± 0.019	1.151 ± 0.019	9.987 ± 0.044	0.334 ± 0.044	5.30	0.010
1503+3644[k]	1237661872417407304	10.811 ± 0.014	1.158 ± 0.014	10.262 ± 0.025	0.609 ± 0.025	106.61	0.431
1514+3852	1237661362380734819	10.876 ± 0.031	1.223 ± 0.031	10.272 ± 0.051	0.619 ± 0.051	60.00	0.698
1543+3446	1237662336790036887	10.024 ± 0.080	0.371 ± 0.080	9.654 ± 0.141	0.001 ± 0.141	5.40	0.024

1559+0841	1237662636912280219	10.628 ± 0.039	0.975 ± 0.039	9.936 ± 0.068	0.283 ± 0.068	95.96	0.735
2237+1336	1237656495641788638	10.752 ± 0.054	1.099 ± 0.054	10.758 ± 0.124	1.104 ± 0.124	15.31	0.063
LBA ID[l]							
J0150	1237649918971084879	11.019 ± 0.070	1.365 ± 0.070	10.431 ± 0.145	0.778 ± 0.145	3.04	...
J0213	1237649919510446221	11.318 ± 0.073	1.665 ± 0.073	10.317 ± 0.092	0.664 ± 0.092	9.20	...
J0921	1237657242433486943	11.440 ± 0.021	1.787 ± 0.021	10.885 ± 0.041	1.232 ± 0.041	4.01	...
J2103	1237652598489153748	11.471 ± 0.134	1.818 ± 0.134	10.517 ± 0.147	0.864 ± 0.147	25.56	...
J1112	1237657591929831540	11.236 ± 0.058	1.582 ± 0.058	10.683 ± 0.082	1.030 ± 0.082	7.60	...
J1113	1237667212133728444	10.620 ± 0.033	0.966 ± 0.033	10.290 ± 0.133	0.637 ± 0.133	0.85	...
J1144	1237662225675124894	10.687 ± 0.049	1.034 ± 0.049	10.573 ± 0.109	0.919 ± 0.109	0.78	...
J1416	1237662528992378986	11.240 ± 0.094	1.587 ± 0.094	10.504 ± 0.101	0.851 ± 0.101	1.69	...
J1521	1237662264860344485	10.980 ± 0.072	1.327 ± 0.072	10.456 ± 0.095	0.802 ± 0.095	3.96	...
J1612	1237662637450592299	11.447 ± 0.071	1.794 ± 0.071	10.857 ± 0.088	1.204 ± 0.088	13.60	...

[a] Green Pea IDs match those in Yang et al 2017.

[b] SDSS DR14 BestObjID.

[c] The associated errors are flux measurement uncertainties based on photon counting statistics (i.e., Poisson statistics) and propagation of the errors during the image calibration procedures such as flat-field correction. Resulting errors are typically 0.05 dex and 0.081 dex in $S_{250\mathrm{pc}}$ and $L_{\mathrm{bol,total}}$, respectively. Additional sources of measurement uncertainty come from the UV-continuum extinction corrections and the k-correction described in Section 3.3.3. These corrections are typically 0.29 dex and 0.04 dex, respectively, with uncertainties that are considerably smaller than the corrections but still potentially significant.

[d] The measured $S_{250\mathrm{pc}}$ in the unit of $\mathrm{L}_{\odot}$ kpc^{-2}. See Section 3.3.3 for details.

[e] The measured star formation intensity (SFI) in the unit of $M_{\odot}$ yr^{-1} kpc^{-2}, which is converted from $\mathrm{L}_{\odot}$ kpc^{-2} into equivalent star formation rate surface density (SFRD). See Section 3.3.3 for details.

[f] The measured $L_{\mathrm{bol,total}}$ in the unit of $\mathrm{L}_{\odot}$. See Section 3.3.3 for details.

[g] The measured star formation rate in the unit of $M_{\odot}$ yr^{-1}, which is converted from $\mathrm{L}_{\odot}$ into equivalent star formation rate (SFR). See Section 3.3.3 for details.

[h] Equivalent Width of Lyα emission line. EW(Lyα) is measured in Yang et al. 2017 and Alexandroff *et al.* (2015) for the sample GPs and LBAs, respectively. The typical measurement uncertainties are $\sim$ 15 % mainly dominated by the systematic error.

[i] Lyα Escape fraction measured in Yang et al. 2017. The typical measurement uncertainties are $\sim$ 15 % mainly dominated by the systematic error.

[j] Green Peas that are also classified as Lyman Break Galaxy Analogs by Alexandroff *et al.* (2015).

[k] Confirmed Lyman continuum leakers identified by Izotov *et al.* (2016).

[l] Lyman Break Galaxy Analog IDs match those in Alexandroff *et al.* (2015).

3.4 Results

3.4.1 Equivalent Width and Escape Fraction of Lyα Emission versus the Central SFI

We now investigate whether the Lyα properties of GPs and LBAs are related to their central SFI. [4] Figure 3.2 shows the relations between EW(Lyα), $f_{esc}^{Ly\alpha}$, and $S_{250\mathrm{pc}}$. First of all, the measured $\log(S_{250\mathrm{pc}}/M_{\odot}\ \mathrm{yr}^{-1}\ \mathrm{kpc}^{-2})$ for 40 sample GPs ranges from ~ 0.37 to ~ 1.66, with a mean $\log(S_{250\mathrm{pc}}/M_{\odot}\ \mathrm{yr}^{-1}\ \mathrm{kpc}^{-2})$ of 1.17. Compared to approximately two orders of magnitude distributions of EW(Lyα) and $f_{esc}^{Ly\alpha}$ of sample GPs, the distribution of their $S_{250\mathrm{pc}}$ is narrower by an order of magnitude. It has a standard deviation of 0.266 dex, which corresponds to a factor of ~ 1.85. For the 15 sample LBAs (that is, including the 5 LBAs also classified as GPs), their measured $\log(S_{250\mathrm{pc}}/M_{\odot}\ \mathrm{yr}^{-1}\ \mathrm{kpc}^{-2})$ is typically larger than that of GPs. The mean $\log(S_{250\mathrm{pc}}/M_{\odot}\ \mathrm{yr}^{-1}\ \mathrm{kpc}^{-2})$ is 1.45 with a standard deviation of 0.271 dex.

We find no significant correlations of either EW(Lyα) (panel (a)) or $f_{esc}^{Ly\alpha}$ (panel (b)) with $S_{250\mathrm{pc}}$, at least for our sample of GPs (i.e., the diamond symbol in the figure) with their relatively narrow dynamic range of $S_{250\mathrm{pc}}$. The associated Spearman correlation coefficients (hereafter, r_{s}) (p-value) with EW(Lyα) and $f_{esc}^{Ly\alpha}$ are only 0.074 (0.7) and -0.027 (0.9), respectively. For comparison, the total bolometric luminosity $L_{\mathrm{bol,total}}$ shows weak and statistically insignificant anti-correlations with EW(Lyα) and $f_{esc}^{Ly\alpha}$, with the associated r_{s} values (p-values) of -0.206 (0.2) and -0.230 (0.2), respectively. Even with the inclusion of LBAs, the correlation between EW(Lyα) and $S_{250\mathrm{pc}}$ in panel (a) does not seem significant, with the associated r_{s} (p-value) of -0.079 (0.6).

[4] We note that our analysis with our sample LBAs is limited to their EW(Lyα), since there is no measured $f_{esc}^{Ly\alpha}$ for our sample LBAs from the literature.

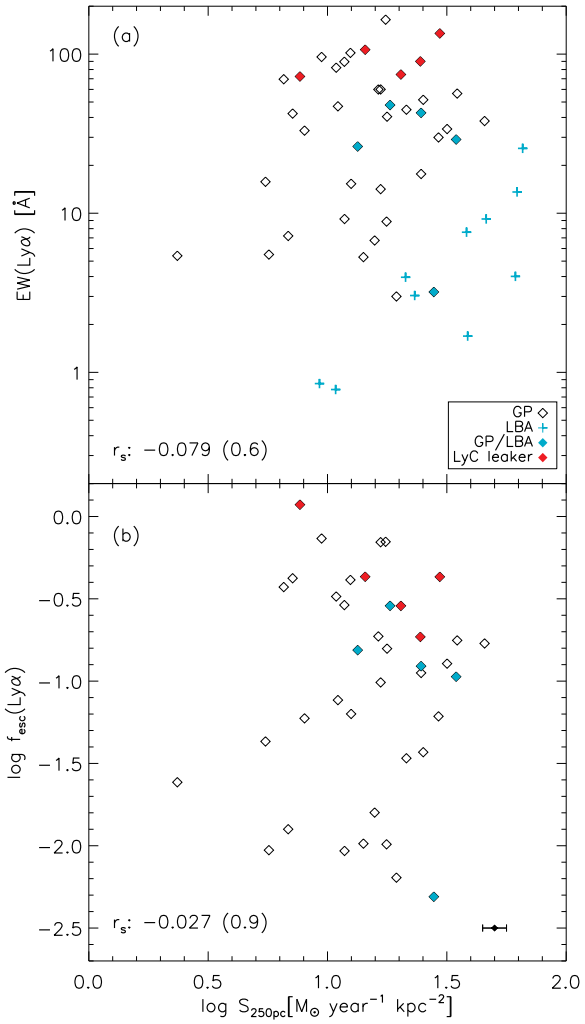

Figure 3.2: EW(Lyα) (panel (a)) and $f_{esc}^{Ly\alpha}$ (panel (b)) vs. $S_{250\mathrm{pc}}$ for sample GPs and LBAs and sample GPs only, respectively. The associated r_{s} values (p-values) are shown in bottom left of each panel. In panel (a), the blue crosses are LBAs, while the blue-filled diamonds are the LBAs that are also classified as GPs (See Section 3.3.1 for details). The red-filled diamonds indicate the five confirmed LyC leakers from Izotov *et al.* (2016). The typical measurement error in $S_{250\mathrm{pc}}$ due to photon counts and propagation of the errors during the image calibration procedures such as flat-field correction is 0.05 dex, which corresponds to 0.125 error in magnitude. The typical error is marked in bottom right in panel (b).

We also mark the five confirmed LyC leakers from Izotov *et al.* (2016) among our sample GPs in the figure (i.e., the red-filled diamonds). The $S_{250\mathrm{pc}}$ that we derived for these LyC leakers using NUV-continuum flux is in broad agreement with that derived using Hβ luminosity and the measured NUV-continuum size (i.e., in the unit of scalelength) in Izotov *et al.* (2016), matching within a factor of ~ 2, except for one galaxy (Green Pea ID 1333+6246) that shows a factor of ~ 3 difference between the studies.

3.4.2 Examining Specific Star Formation Intensity

The specific star formation rate (sSFR), defined as star formation rate normalized by stellar mass, is a powerful summary statistic for the level of star formation in galaxies (e,g., Whitaker *et al.*, 2012; Kim *et al.*, 2018). Since the power available to drive galactic winds increases with increasing star formation, while the escape velocity for such winds increases with stellar mass, it is reasonable to expect galactic scale outflows to be more common and stronger where sSFR is high. Very actively star-forming galaxies like Green Peas and higher redshift Lyα emitters commonly have sSFR $\gtrsim 10^{-8}\mathrm{yr}^{-1}$, implying stellar mass doubling times of $< 10^8$ yr (e.g., Cardamone *et al.*, 2009; Izotov *et al.*, 2011; Finkelstein *et al.*, 2015; Yang *et al.*, 2017a; Jiang *et al.*, 2019b).

Next, therefore, we examine the dependences of EW(Lyα), $f_{esc}^{Ly\alpha}$, and $S_{250\mathrm{pc}}$ on both sSFR and also the specific star formation intensity (sSFI), which we define as the SFI divided by total stellar mass. LAEs, including GPs, typically have low stellar mass ($8 \lesssim \log(M_{\mathrm{star}}/M_{\odot}) \lesssim 10$) (e.g., Gawiser et al. 2007; Pirzkal et al. 2007; Y17), and show an anti-correlation between stellar mass and EW(Lyα) (e.g., Marchi *et al.*, 2019). This provides a further empirical motivation to investigate the effect of stellar mass on the observed trends between EW(Lyα), $f_{esc}^{Ly\alpha}$, and $S_{250\mathrm{pc}}$. Figure

3.3 again plots both EW(Lyα) and $f_{esc}^{Ly\alpha}$, but now as functions of $S_{250\mathrm{pc}}$ *divided* by stellar mass ($\log S_{250\mathrm{pc}}/M_{\mathrm{star}}$). For our sample GPs, we find that both EW(Lyα) and $f_{esc}^{Ly\alpha}$ show significant positive correlations with $\log S_{250\mathrm{pc}}/M_{\mathrm{star}}$. The correlations with $\log S_{250\mathrm{pc}}/M_{\mathrm{star}}$ are stronger than those with sSFR (which are $r_{\mathrm{s}} = 0.475$, $p = 2\times10^{-3}$; and $r_{\mathrm{s}} = 0.420$, $p = 7\times10^{-3}$, respectively.) Moreover, when our sample LBAs are also considered in the correlation between EW(Lyα) and $\log S_{250\mathrm{pc}}/M_{\mathrm{star}}$ (i.e., panel (a) in the figure), the associated r_{s} value shows the most significant correlation coefficient of 0.702 with its p-value of 10^{-8} among the ones we explored. All the correlation coefficients are summarized in Table 3.2.

As in Figure 3.2, the five confirmed LyC leakers are marked in the red-filled diamonds in Figure 3.3. In the parameter space of $S_{250\mathrm{pc}}/M_{\mathrm{star}}$, all five LyC leakers have $S_{250\mathrm{pc}}/M_{\mathrm{star}} \gtrsim 10^{-7.7}$ yr^{-1} kpc^{-2}, larger than the median of $10^{-8.1}$ yr^{-1} kpc^{-2} of the entire sample distribution.

3.5 Discussion and Conclusions

In this study, we have identified a sample of Green Pea and Lyman Break Analog galaxies, which are (respectively) some of the best local analogs of high-z Lyα- and Lyman break galaxies. Using this sample, we have measured the central UV SFI ($S_{250\mathrm{pc}}$) and specific star formation intensity $S_{250\mathrm{pc}}/M_{\mathrm{star}}$, and investigated the correlations between these two quantities and Lyα line strength, as characterized by EW(Lyα) and $f_{esc}^{Ly\alpha}$. We summarize our primary results and conclusions below.

First, the central UV SFI of GPs and LBAs is approximately three orders of magnitude larger than typical for normal star-forming galaxies (e.g., Kennicutt, 1998). Moreover, this SFI has a relatively narrow distribution, with $\sigma \sim 0.27$ dex. And, the typical SFI for LBAs is about double that for GPs. (Specifically, the mean $S_{250\mathrm{pc}}$ is $\sim 28\ M_{\odot}$ yr^{-1} kpc^{-2} for LBAs, and 15 $M_{\odot}$ yr^{-1} kpc^{-2} for GPs).

Table 3.2: The Spearman Correlation Coefficients Between Parameters, and the Associated Probability Values

	EW(Lyα)		$f_{esc}^{Ly\alpha}$	
Parameter	$r_{\rm s}$	p	$r_{\rm s}$	p
GP only				
SFI $\equiv S_{250\rm pc}$	0.074	0.7	-0.027	0.9
$L_{\rm bol,total}$	-0.206	0.2	-0.229	0.2
sSFR $\equiv$ SFR $/M_{\rm star}$	0.475	2×10^{-3}	0.420	7×10^{-3}
$1/M_{\rm star}$	0.544	3×10^{-4}	0.503	1×10^{-3}
sSFI $\equiv S_{250\rm pc}/M_{\rm star}$	0.626	2×10^{-5}	0.529	5×10^{-4}
GP+LBA				
SFI $\equiv S_{250\rm pc}$	-0.079	0.6	...	...
$L_{\rm bol,total}$	-0.272	0.06	...	...
sSFR $\equiv$ SFR $/M_{\rm star}$	0.617	2×10^{-6}	...	...
$1/M_{\rm star}$	0.645	4×10^{-7}	...	...
sSFI $\equiv S_{250\rm pc}/M_{\rm star}$	0.702	1×10^{-8}	...	...

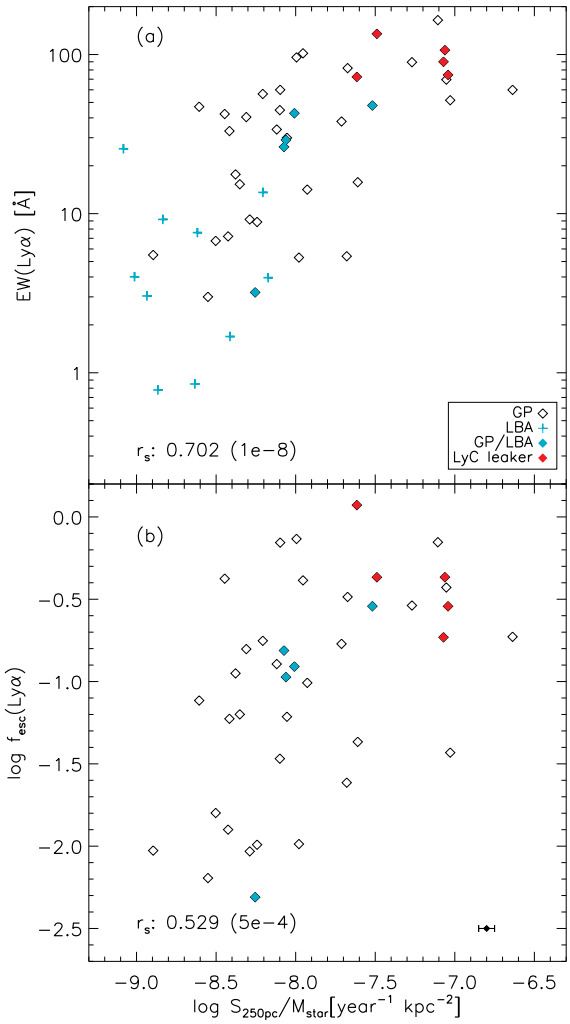

Figure 3.3: Same as Figure 3.2, but for against $\log S_{250\mathrm{pc}}/M_{\mathrm{star}}$ on x-axis. The more significant positive correlations of EW(Lyα) and $f_{esc}^{Ly\alpha}$ with $\log S_{250\mathrm{pc}}/M_{\mathrm{star}}$ than with $S_{250\mathrm{pc}}$ are shown.

Such high SFI may blow significant holes in the ISM, where the HI column density ($N_{\rm HI}$) becomes low enough that Lyα photons escape more easily. We note that most Lyα-emitting galaxies have compact morphological properties (e.g., Malhotra *et al.*, 2012; Alexandroff *et al.*, 2015; Verhamme *et al.*, 2017; Izotov *et al.*, 2018a; Ritondale *et al.*, 2019), and that their small sizes allow moderate star formation to produce the comparatively high SFI ($\gtrsim 0.1 M_\odot$ yr^{-1} kpc^{-2}, Heckman (2001); Izotov *et al.* (2016)) needed for this mechanism.

High SFI is linked to high central pressure P_0. This pressure is most likely dominated by contributions from stellar winds and (possibly) supernovae feedback from the central starburst regions, and may drive galactic outflows (e.g., Heckman *et al.*, 2015; Heckman and Borthakur, 2016). (Note, however, that intense star formation in nascent massive star clusters can generate high ambient pressure, but under some conditions may also lead to radiative cooling that reduces the resulting feedback (e.g., Silich and Tenorio-Tagle, 2018)). Indeed, all of our sample GPs and LBAs have SFI $> 0.1 M_\odot$ yr^{-1} kpc^{-2}, which is a suggested SFI threshold for galactic-scale outflows (i.e., Heckman, 2002). Adopting the relationship between the effective surface brightness $S_{\rm eff}$ and P_0 of $S_{\rm eff}/10^{11} L_\odot$ kpc$^{-2} = P_0/1.63 \times 10^{-9}$dy cm^{-2} (which Meurer *et al.* (1997) derived from a starburst population model), the $S_{\rm 250pc}$ distribution of our Green Pea and LBA samples corresponds to the P_0 range of $10^{6.1}$ Kcm^{-3} $\lesssim P_0/k_{\rm B}$ $\lesssim 10^{7.54}$ Kcm^{-3}, with a median $P_0/k_{\rm B}$ of $10^{6.97}$ Kcm^{-3}, where $k_{\rm B}$ is the Boltzmann constant. Although the details and uncertainties should be considered, the $P_0/k_{\rm B}$ distribution derived using $S_{\rm 250pc}$ is largely consistent with the gas pressures derived using optical emission lines in a sample of GPs and LBAs (i.e., Jiang *et al.*, 2019b).

However, high SFI alone does not guarantee high Lyα photon escape, since the direct comparisons between $S_{\rm 250pc}$, EW(Lyα), and $f_{esc}^{Ly\alpha}$ do not show significant positive correlations. In particular, our sample LBAs show larger $S_{\rm 250pc}$ than our sample

GPs do, but do not necessarily show larger EW(Lyα) (i.e., Figure 3.2). The absence of significant correlations between EW(Lyα) or $f_{esc}^{Ly\alpha}$ and $S_{250\mathrm{pc}}$ suggests that additional physical properties beyond high SFI alone must play a large role in Lyα photon escape. These could include low gas density associated with the ISM geometry, low stellar mass, low gas-phase metallicity, and so on (e.g., Gawiser et al. 2007; Shibuya et al. 2014; Song et al. 2014; Y17).

The strongest correlations in our study are of EW(Lyα) and $f_{esc}^{Ly\alpha}$ with sSFI $\equiv S_{250\mathrm{pc}}/M_{\mathrm{star}}$ (Figure 3.3 and Table 3.2), and not with $S_{250\mathrm{pc}}$ alone. This suggests that stellar mass (or related galaxy properties) plays a role in Lyα escape, such that galaxies with lower stellar masses have higher Lyα escape for any particular value of $S_{250\mathrm{pc}}$. The correlations of EW(Lyα) with $S_{250\mathrm{pc}}/M_{\mathrm{star}}$ ($r_{\mathrm{s}} = 0.626$, $p = 2 \times 10^{-5}$) and $f_{esc}^{Ly\alpha}$ with $S_{250\mathrm{pc}}/M_{\mathrm{star}}$ ($r_{\mathrm{s}} = 0.529$, $p = 5 \times 10^{-4}$) are stronger than the corresponding correlations with $1/M_{\mathrm{star}}$ alone ($r_{\mathrm{s}} = 0.544$, $p = 3{\times}10^{-4}$; and $r_{\mathrm{s}} = 0.503$, $p = 1{\times}10^{-3}$). They are likewise stronger than the correlations with sSFR, as examined in Section 3.4.2.

The correlation between EW(Lyα) and sSFI becomes even stronger when we add the LBAs to the sample, with $r_{\mathrm{s}} = 0.702$ and $p = 10^{-8}$.

We suggest Lyα escape in galaxies that have high sSFI results from an interstellar medium with holes in the neutral hydrogen distribution, and/or outflow of neutral hydrogen (with consequent reduction of resonant scattering optical depth). Such ISM geometry and kinematics would be produced by the combination of high pressure in regions of high SFI, which provides a driving force for outflows that clear neutral hydrogen; and low mass, which results in shallow gravitational potentials and makes it easier for winds to effectively remove material from the neighborhood of the star formation. There is a metallicity dependence in the conversion from Hα luminosity to SFR, but over the full metallicity range of our sample ($7.7 \lesssim 12 + \log(\mathrm{O/H}) \lesssim 8.5$)

this conversion factor changes only 0.1 dex (c.f., Figure 6 of Lee *et al.*, 2009). This is insignificant compared to the 2.5 dex spread we observe in sSFI.

The importance of sSFI in UV photon escape is further demonstrated by a progression in measured sSFI between LyC leakers, GPs, and LBAs. LyC leakers typically show the highest sSFI, GPs the next, and LBAs the lowest (i.e., panel (a) in Figure 3.3). Both Lyman continuum and Lyα escape are enabled by low HI column densities, but Lyman continuum escape tends to require lower columns than Lyα escape, especially given that resonant scattering effects may enable Lyα to escape for a wider range of geometries (e.g., Neufeld, 1991).

In conclusion, we have examined the relation between Lyα emission and multiple tracers of star formation activity. We find that both high star formation intensity (SFI, defined as star formation rate per area) and high specific star formation rate (sSFR, star formation rate per unit stellar mass) are general properties of Green Peas and Lyman Break Galaxy Analogs, distinguishing them from the broader population of star-forming galaxies. But beyond that, we have demonstrated that the specific star formation intensity (sSFI, defined as SFI per unit stellar mass) is the most powerful predictor of Lyα emission. This is likely because channels of low HI opacity are more easily cleared in galaxies with high sSFI, due to the interplay between star formation intensity that drives galactic winds and gravitational potential that impedes them.

Chapter 4

THE COMPACT UV SIZE OF GREEN PEA GALAXIES AS LOCAL ANALOGS OF HIGH REDSHIFT LYα-EMITTERS

4.1 Abstract

We study the dependence of Lyα escape from galaxies on UV continuum size and luminosity using a sample of 40 Green Pea (GP) galaxies, which are the best local analogs of high-redshift Lyα emitters (LAEs). We use the high angular resolution (0.0235 arcsec pixel^{-1}) Cosmic Origins Spectrograph near-ultraviolet images from the *Hubble Space Telescope* to measure the UV size and luminosity. Like most galaxies the GPs show a log-normal size distribution. They also show a positive correlation between size and luminosity. The slope of the size-luminosity relation for GPs is consistent with those of continuum-selected star-forming galaxies at low and high redshifts. A distinctive feature of GPs is a very compact typical radius of 0.28 ± 0.14 kpc. The peak of the size distribution and the intercept of the size-luminosity relation of GPs are noticeably smaller than those of typical star-forming galaxies at similar redshifts. There are statistically significant anti-correlations found between $r_{\rm cir,50}$, the Lyα equivalent width (EW(Lyα)), and the Lyα escape faction ($f_{esc}^{Ly\alpha}$), suggesting that small UV-continuum radii are crucial for Lyα emission. GPs and high-redshift LAEs have similar sizes, once spatial resolution effects are properly considered. Our results show that a compact size is crucial for escape of Lyα photons, and that Lyα emitters show constant characteristic size independent of their redshift.

4.2 Introduction

Lyα-emitting galaxies (i.e., Lyα-emitters, LAEs) are a class of galaxies characterized by spectra with prominent Lyα emission lines. Since Lyα photons are usually generated by intense star formation activity, most LAEs have relatively high star formation rate (SFR) for their stellar mass (i.e., specific star formation rate (sSFR) $\gtrsim 10^{-8}\mathrm{yr}^{-1}$) and relatively young stellar population ages ($\lesssim 50$ Myr) (e.g., Malhotra and Rhoads, 2002; Gawiser *et al.*, 2007; Pirzkal *et al.*, 2007; Finkelstein *et al.*, 2015). However, because Lyα photons are resonantly scattered by neutral hydrogen and significantly affected by dust absorption/scattering (e.g., Ahn *et al.*, 2003), not all actively star-forming galaxies (SFGs) have observable Lyα emission, which requires that Lyα photons manage to escape from star-forming regions within the galaxy all the way to the intergalactic medium (IGM). So, what are the properties of LAEs that allow Lyα to escape?

Lyα emission from galaxies is also one of the most promising indicators for identifying Lyman-continuum (LyC) leakers (i.e., galaxies that emit significant amounts of ionizing radiation to the IGM) (Verhamme *et al.*, 2015; de Barros *et al.*, 2016; Izotov *et al.*, 2016; Gazagnes *et al.*, 2020). LyC leaking galaxies are important for cosmology, because they were significant and probably dominant sources of the photons that drove reionization of the early universe ($z > 6$). Thus, studying the physical properties of LAEs and understanding their Lyα (and potentially LyC) escape mechanisms have been important topics in the fields of galaxy evolution and cosmology, respectively (e.g., Malhotra and Rhoads, 2002; Malhotra *et al.*, 2012; Rhoads *et al.*, 2000, 2014; Finkelstein *et al.*, 2015; Oyarzún *et al.*, 2017, and references therein).

Multiple observations and morphological analysis of LAEs show that they are mostly compact (with effective radius $r_{\mathrm{eff}} \lesssim 1.5$ kpc), sometimes with clumpy features

shown in UV continuum, at high redshifts $2 \lesssim z \lesssim 7$ (e.g., Dow-Hygelund *et al.*, 2007; Overzier *et al.*, 2008; Bond *et al.*, 2009; Taniguchi *et al.*, 2009; Bond *et al.*, 2012; Malhotra *et al.*, 2012; Jiang *et al.*, 2013; Paulino-Afonso *et al.*, 2018; Shibuya *et al.*, 2019; Ritondale *et al.*, 2019). Based on the approximately constant typical sizes of LAEs over a wide span of redshift ($2 \lesssim z \lesssim 6$), Malhotra *et al.* (2012) suggested that the compact size of LAEs is a crucial physical condition for a galaxy to become an LAE, as recent analytic calculations on morphologically compact conditions for LyC leakers also suggest (Cen, 2020). This has been supported by later studies (e.g., Jiang *et al.*, 2013; Paulino-Afonso *et al.*, 2018), but others (notably Shibuya *et al.*, 2019) have challenged this with the view that LAEs follow similar size-luminosity relations, and show size evolution with redshift similar to high redshift Lyman Break Galaxies.

Extending this redshift dependence to lower redshifts would give a more sensitive test of whether the characteristic radius of LAEs evolves like $(1 + z)^{-1.37}$ (Shibuya *et al.*, 2019) or is flat. Going from $z = 6$ to 2 gives a factor of 3 change in the size while going to $z = 0.3$ predicts more than a factor of 10 in radius change. Green Peas are the best low redshift analogs of high-redshift LAEs in terms of equivalent width distribution (Yang *et al.*, 2016). Green Peas were selected as high equivalent width [OIII] emitters in a citizen science project, and have generally low metallicities and low masses (Cardamone *et al.*, 2009; Amorín *et al.*, 2010; Jaskot and Oey, 2013; Henry *et al.*, 2015; Izotov *et al.*, 2016; Yang *et al.*, 2016, 2017c,b; Izotov *et al.*, 2018b; Orlitová *et al.*, 2018; Jiang *et al.*, 2019a,c; Jaskot *et al.*, 2019).

This is the second of the series of papers where we investigate the UV continuum morphologies of Green Pea (GP) galaxies to understand the mechanisms enabling Lyα escape. In the first paper (Kim *et al.*, 2020) we investigated the effects of star-formation per unit area (star formation intensity, SFI) and specific star-formation rate (sSFR). In this paper we investigate the UV size and luminosity of a sample

of GPs that were observed with the Cosmic Origins Spectrograph near-ultraviolet (COS/NUV) acquisition images from the *Hubble Space Telescope (HST)*. The high angular resolution (i.e., 0.0235 arcsec pixel^{-1}) of the COS/NUV images and the low redshifts (0.1-0.3) of GPs have enabled us to measure the spatially resolved UV sizes with a factor of ~ 2 better resolution limit compared to other *HST* instrument+filter combinations typically used for measuring the sizes of high-z LAEs (i.e., 0.047 arcsec, vs. 0.09 arcsec for the Advanced Camera for Surveys (ACS) F850LP filter, and 0.13 arcsec for the Wide Field Camera 3 (WFC3) F160W) (Windhorst *et al.*, 2011). We use this exquisite spatial resolution to test whether low-redshift LAEs have compact physical sizes, which would be expected if the small sizes of high-z LAEs are causally linked to Lyα escape. Alternatively, if high-z LAEs are compact merely because high-z galaxies are compact in general, we would expect their local counterparts to be larger. We also use our data set to study more general aspects of the relation between Lyα escape and UV continuum size.

Section 4.3 describes our galaxy sample and procedures for UV size and luminosity measurements. In Section 4.4, we present our results. We summarize our conclusions in Section 4.5. Throughout this paper, we adopt the AB magnitude system and the ΛCDM cosmology of (H_0, Ω_m, Ω_Λ) = (70 kms^{-1} Mpc^{-1}, 0.3, 0.7).

4.3 Sample and Data Analysis

4.3.1 GP Sample

Our GP sample consists of the 40 galaxies that are analyzed and presented by Yang et al. 2017b (hereafter Y17) and Kim *et al.* (2020) (hereafter K20). Our sample GPs have redshifts $0.1 \lesssim z \lesssim 0.35$. We adopt GP ID and Ly$\alpha$ properties such as the equivalent width of Lyα line (EW(Lyα)), the Lyα escape fraction ($f_{esc}^{Ly\alpha}$), and the

Lyα luminosity (L(Lyα)) from Y17. We also adopt galactic internal extinction ($A_{\rm int}$), Milky Way extinction ($A_{\rm MW}$), and the k-correction (k) values from K20 to derive the extinction and k-corrected UV luminosity at rest-frame wavelength of 1877 $\mathring{A}$ of our sample GPs in Section 2.2.

As described in K20, the 40 sample GPs have been observed with the COS/NUV acquisition images with the MIRRORA configuration. The pivot wavelength of the observed filter is 2319.7 $\mathring{A}$. The exposure time of the NUV images of our sample GPs is mostly greater than 100 s. For more details we refer the reader to Paper I (K20: Kim *et al.*, 2020).

4.3.2 Size and Luminosity Measurements

We measure the UV-continuum size and luminosity of our sample GPs using the same point-spread function (PSF)-deconvolved, Haar-wavelet denoised, and sky-subtracted COS/NUV images that we presented in K20 and used in K20 to measure the central star formation intensity (SFI, star formation rate per unit area) of this sample. As a brief description of the image processing, the 200 $\times$ 200 pixel (4.7$''$ $\times$ 4.7$''$) raw NUV images are first deconvolved with the PSF image of star P330E observed during the *HST* program 11473 [1] . The PSF-deconvolved images are then Haar-wavelet denoised by applying the 2D generalized TIPSH algorithm [2] originally developed in 1D for modelling transient light curves (Kolaczyk, 1997). The processed images are then sky-subtracted. We refer to Section 2.2 of K20 for further details.

To measure size, we first derive the galaxy center and apparent axis ratio b/a (and ellipticity $\epsilon = 1 - b/a$) by performing surface brightness profile fitting using the public software GALFIT (version 3.0.5) (Peng *et al.*, 2002, 2010a). During the fitting

[1] http : //www.stsci.edu/hst/cos/documents/isrs/ISR2010_10.pdf

[2] http : //butler.lab.asu.edu/wavelet_denoising

procedure, we assume one component Sérsic profile, and the associated background noise σ images are internally generated by considering image information such as exposure time, readout noise, and the number of combined images from the image header. The initial guesses for galaxy center, apparent magnitude, and the effective radius are adopted from the measured values in K20. Specifically, the brightest pixel of the NUV images, and the Petrosian-based galaxy segmentation maps and the pixel-count based size parameter (Petrosian, 1976; Law *et al.*, 2007; Ribeiro *et al.*, 2016) are used to obtain initial values of the galaxy center, apparent magnitude, and effective radius. The initial values for b/a and Position Angle (i.e., the direction of galaxy major axis in the sky) are set 0.8 and 0 degree, respectively for all sample galaxies.

Additionally, we put constraints on the fitting range of some parameters. A fitting solution for this type of multi-parameter fit does not always guarantee a physically sound result, even with a reasonably good reduced-χ^2 value (e.g., Peng *et al.*, 2010a; Meert *et al.*, 2015; Kim *et al.*, 2016, for relevant discussions). Therefore, to make sure that the fits are physically motivated, the fitted galaxy center is to be within 5 pixels from the initial galaxy center; the effective radius is greater than 1 pixel but less than the twice the total radius derived from the galaxy size parameter mentioned above; the Sérsic index is between 1 and 8; and the b/a value is fitted between 0.2 to 1.

From the fit results, we employ the apparent axis ratio (b/a) and the galaxy center values to measure size and luminosity. Specifically, we adopt the Petrosian radius definition (Petrosian, 1976) for size measurement. Since the Petrosian radius depends on the surface brightness profile (i.e., a curve of growth) of a galaxy, this size definition has the advantages of being redshift independent, less sensitive to dust reddening, and insensitive to variations in the Signal to Noise ratio and in the limiting surface brightness of the observations (Petrosian, 1976; Lotz *et al.*, 2004). The Petrosian radius $r_{\rm p}$ is defined to be the radius at which the surface brightness

$\mu(r_{\rm p})$ is equal to a factor of η times the mean surface brightness $\bar{\mu}(r < r_{\rm p})$ within the $r_{\rm p}$. That is, $\mu(r_{\rm p}) = \eta \times \bar{\mu}\ (r < r_{\rm p})$. A constant η value is typically set to 0.2 (e.g., Petrosian, 1976; Conselice *et al.*, 2000; Shimasaku *et al.*, 2001; Lotz *et al.*, 2004; Guaita *et al.*, 2015). We adopt the same η value of 0.2 for our size measurement.

To solve for the above Petrosian equation, we measure the surface brightness profile of galaxies by performing the IRAF ellipse task with the processed NUV images. During the ellipse task, we fix the galaxy center and the ellipticity ϵ with the values obtained from the GALFIT results. The measured surface brightness profile of sample GPs is used to find the $r_{\rm p}$. The exact value of $r_{\rm p}$ is calculated by first finding the two closest radii to $r_{\rm p}$ at which the surface brightnesses are measured, and then performing linear interpolation or extrapolation with these two closest radii to derive the exact $r_{\rm p}$ that satisfies the Petrosian equation. The typical difference between the exact value of $r_{\rm p}$ derived and the two closest radii found in the measured surface brightness profile is only 0.24 pixels (equivalently 0.0056 arcsec). This small interpolation/extrapolation corresponds to the $\sim$ 4% relative difference between the derived $r_{\rm p}$ and the two closest radii (that is, $1 - (\bar{r_{\rm cl}}/r_{\rm p}) \sim 0.04$ where $\bar{r_{\rm cl}}$ is the mean radius of the two closest radii). Therefore, we do not expect the details of our interpolation procedure (e.g., the polynomial degree used) to significantly change our measured sizes.

We subsequently measure the UV-continuum luminosity $L_{\rm p}$ and the Petrosian half-light radius r_{50} based on the $r_{\rm p}$ by following the conventional definitions of $L_{\rm p}$ and r_{50} (e.g., Shimasaku *et al.*, 2001). The $L_{\rm p}$ is defined to be the total flux within the enclosed area of $2r_{\rm p}$ from galaxy center, and the r_{50} to be the radius within which the half of $L_{\rm p}$ is enclosed. As in the $r_{\rm p}$ measurement, we perform the same linear interpolation/extrapolation to derive the exact values of $L_{\rm p}$ and r_{50}. The measured r_{50} of our sample GPs in pixel unit ranges from 2 pixel $\lesssim r_{50} \lesssim$ 17 pixel, with a median of 4.1 pixel, first and third quartile values of 2.7 pixel and 5.3 pixel,

and a standard deviation of 2.7 pixel. The measurement uncertainties in $L_{\rm p}$ and r_{50} are derived considering the Poisson statistics (i.e., photon counting statistics) and propagation of the errors during the image calibration procedures such as flat-field correction obtained from the provided COS/NUV error images. The typical measurement uncertainties in $L_{\rm p}$ and r_{50} in our sample GPs are 0.3 mag and 0.023 kpc, respectively.

Lastly, the measured $L_{\rm p}$ is corrected for galactic internal extinction ($A_{\rm int}$), Milky Way extinction ($A_{\rm MW}$), and the k-correction (k) with the values obtained from K20 (see Section 4.3.1 for details). By adopting the characteristic luminosity at $z \sim 3$ ($L_{*,{\rm z=3}}$) which corresponds to UV magnitude of -21, the $L_{\rm p}$ of our sample GPs ranges from $0.08L_{*,{\rm z=3}}$ to $1.9L_{*,{\rm z=3}}$, with a median $L_{\rm p}$ of $0.5L_{*,{\rm z=3}}$. We also calculate the circularized half-light radius (i.e., $r_{\rm cir,50} = r_{50} \times \sqrt{b/a}$). We use $r_{\rm cir,50}$ for subsequent analysis in this study. The measured $r_{\rm p}$, r_{50}, $r_{\rm cir,50}$, b/a, and $L_{\rm p}$ as well as the adopted extinction ($A_{\rm int}$ and $A_{\rm MW}$) and k-correction (k) values are listed in Table 2.1.

4.4 Results and Discussion

4.4.1 Size Distribution of GPs

In this section, we investigate the UV size distribution of our sample GPs. Figure 4.1 shows the distribution of $r_{\rm cir,50}$. Our sample GPs show mostly small UV sizes with a median $r_{\rm cir,50}$ of 0.284 kpc and a 1σ spread of 0.15 kpc, marked as the vertical dashed line and the horizontal solid line in figure 4.1, respectively. The size distribution is relatively narrow as its semi-interquartile range is only 0.085 kpc. The mean $r_{\rm cir,50}$ of 0.33 kpc is larger than the median, due to the presence of a long tail toward large sizes as shown in the figure.

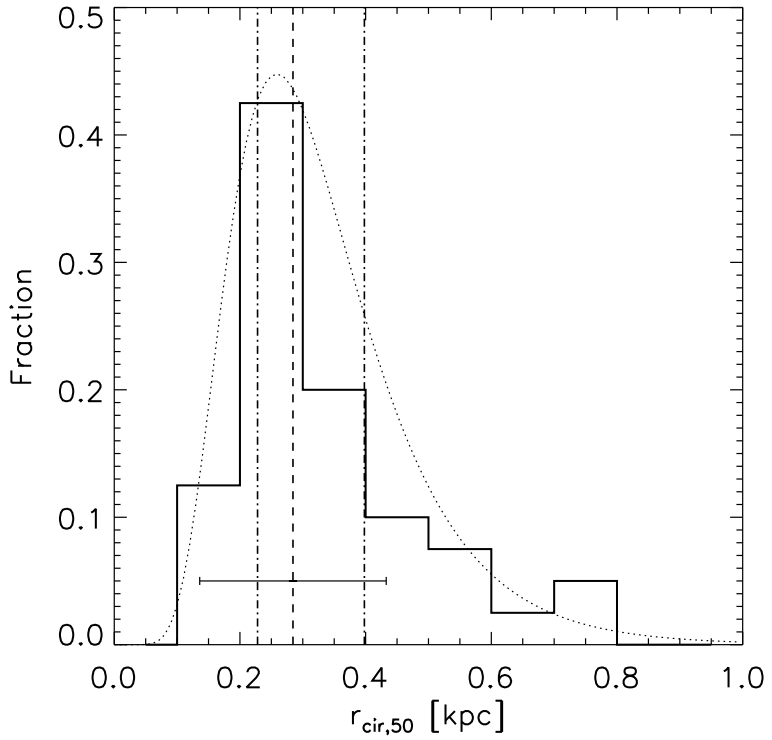

Figure 4.1: The size ($r_{\rm cir,50}$) distribution of 40 sample Green Pea galaxies. The vertical dashed line indicates the median $r_{\rm cir,50}$ of 0.284 kpc, while the horizontal solid line indicates a 1σ of 0.15 kpc. The 25th and 75th quartiles of the size distribution are 0.228 kpc and 0.398 kpc, respectively, marked as the vertical dot-dashed lines. The semi-interquartile range of the distribution is 0.085 kpc. The dotted curve shows the log-normal fit to the size distribution. This fit has median size ($r_{\rm med}$) of 0.31 kpc and the width of ($\sigma_{\ln(\rm r_{cir,50})}$) of 0.41. The fitted log-normal probability density function is scaled by a factor of 0.13 to visualize with the actual distribution.

We also fit the size distribution of our sample GPs with a log-normal distribution:

$$p(r_{\rm cir,50}) = \frac{1}{\sigma_{\ln(\rm r_{cir,50})} r_{\rm cir,50}\sqrt{2\pi}} \exp\left[- \frac{\ln^2(r_{\rm cir,50}/r_{\rm med})}{2{\sigma_{\ln(\rm r_{cir,50})}}^2} \right], \tag{4.1}$$

where $p(r_{\rm cir,50})$ is the log-normal probability density function of $r_{\rm cir,50}$, and $r_{\rm med}$ and $\sigma_{\ln(\rm r_{cir,50})}$ are the median size and the width of the fitted log-normal distribution, respectively. As shown in Figure 4.1, the size distribution of our sample GPs is well fitted by a log-normal function (i.e., dotted line) with the associated $r_{\rm med}$ and $\sigma_{\ln(\rm r_{cir,50})}$ of 0.31 kpc and 0.41, respectively.

A relevant interpretation to the log-normal distribution of galaxy size might come from theoretical galaxy disk formation models (e.g., Peebles, 1969; Fall and Efstathiou, 1980; Barnes and Efstathiou, 1987; Mo *et al.*, 1998) where the pre-collapse dark matter (DM) halo angular momentum—parameterized as the dimensionless spin parameter $\lambda \equiv \frac{J|E|^{1/2}}{GM^{5/2}}$ where J, E, M, and G indicate the total angular momentum, energy, and mass of the system, and the gravitational constant, respectively—is predicted to have a log-normal distribution with the associated peak value $\lambda_{\rm med}$ and the width $\sigma_{\ln(\lambda)}$ of ~ 0.05 and $\sim 0.5 - 0.6$, respectively (Barnes and Efstathiou, 1987; Warren *et al.*, 1992; Cole and Lacey, 1996; Davis and Natarajan, 2009). Assuming that the baryonic component acquired most of its angular momentum through its surrounding dark matter halos and that the galaxy disk size is largely determined by the multiplication of λ by the virial radius ($R_{\rm vir}$) (e.g., Fall and Efstathiou, 1980; Mo *et al.*, 1998), it seems reasonable to expect that the galaxy disk size distribution also follows a log-normal distribution, reflecting the underlying dark matter halo properties. Our fitted log-normal UV size distribution of sample GPs with the associated $\sigma_{\ln(\rm r_{cir,50})}$ of 0.41 shows a $\sim 20\%$ narrower width compared to the predicted dark matter halo λ distribution with the associated $\sigma_{\ln(\lambda)}$ of ~ 0.5, but is broadly consistent with other types of star-forming galaxies at low and high redshifts (e.g., de Jong and Lacey, 2000; Shen *et al.*, 2003; Huang *et al.*, 2013).

4.4.2 UV Size-Luminosity Relation of GPs

The size-luminosity relationship for galaxies is a key piece to understand the growth history of galaxies over cosmic time. For the high-z universe, the UV size-luminosity relations of star-forming galaxies such as LAEs and UV continuum-selected Lyman Break Galaxies (LBGs) have been previously investigated (e.g., Oesch *et al.*, 2010; Huang *et al.*, 2013; Jiang *et al.*, 2013; Ono *et al.*, 2013; Shibuya *et al.*, 2015).

The size-luminosity relation is often parameterized as a power-law with a slope of α:

$$r_{\rm cir,50} = r_0 \left(\frac{L_{\rm UV}}{L_0} \right)^{\alpha}, \tag{4.2}$$

where $L_{\rm UV}$, L_0, and r_0 are the UV luminosity of galaxies, the same characteristic UV luminosity as the $L_{*,z=3}$ of $M_{\rm UV} = -21$ that we adopted in Section 2.2, and the intercept at L_0, respectively.

The fitted α and r_0 of our sample GPs are 0.23 ± 0.08 and 0.37 ± 0.03 kpc, respectively. The slope value is consistent within the uncertainties with those for high-z ($2 \lesssim z \lesssim 8$) star-forming galaxy populations, which show a slope range of $0.15 \lesssim \alpha \lesssim 0.5$ with the typical α of ~ 0.27 (Grazian *et al.*, 2012; Jiang *et al.*, 2013; Huang *et al.*, 2013; Shibuya *et al.*, 2015; Curtis-Lake *et al.*, 2016). A brief interpretation on the slope of the size-luminosity relation might come from theoretical galaxy disk formation models (as in Section 3.1). Based on the Tully-Fisher relation and the assumed constant mass-to-light (M/L) ratio of disks, the fiducial slope of the size-luminosity derived is 1/3 (Mo *et al.*, 1998). The deviation from the fiducial slope value could be due to varying M/L ratio and/or stellar feedback such as SN feedback from star formation in disks, as such effects can change the slope value (Wyithe and Loeb, 2011; Liu *et al.*, 2017). The fitted slope of our sample GPs is broadly in agreement within the uncertainties with the suggested value of 0.25 from the semi-analytic model that accounts for the effect of SN feedback (Liu *et al.*, 2017).

Figure 4.2 shows the UV size-luminosity relation of our sample GPs. Comparing the the distribution of individual data points to lines of constant effective star formation intensity ($S_{\rm eff}$) demonstrates that all of our sample GPs have $S_{\rm eff} \gtrsim 1\ M_\odot\ {\rm yr}^{-1}\ {\rm kpc}^{-2}$, which is 2+ orders of magnitude above those of typical star forming galaxies ($\lesssim 0.01\ M_\odot\ {\rm yr}^{-1}\ {\rm kpc}^{-2}$) (e.g., Kennicutt, 1998). This is mainly due to the compact sizes of GPs given their UV luminosity. Here, the effective SFI is defined as

$S_{\rm eff} \equiv \frac{\rm SFR}{2\pi r^2_{\rm cir,50}} \left(\frac{M_\odot\ {\rm yr}^{-1}}{\rm kpc^2}\right)$. To convert the measured UV luminosity to the corresponding SFR, we adopt the solar bolometric magnitude of 4.74 (Bessell *et al.*, 1998), and the UV to bolometric luminosity ($L_{\rm bol}$) ratio ($L_{\rm UV}/L_{\rm bol}$) of 0.33 and the scale factor $L_{\rm bol}/(4.5 \times 10^9 L_\odot) = {\rm SFR}/(1 M_\odot\ {\rm yr}^{-1})$ that are derived from the starburst population modelling by Meurer *et al.* (1997). The starburst population modelling assumes a solar metallicity and the Salpeter initial mass function (Salpeter, 1955) with upper and lower mass limits of 0.1 $M_\odot$ and 100 $M_\odot$, respectively.

The effective SFI of our sample GPs mostly ranges from 1 to 30 $M_\odot$ yr^{-1} kpc^{-2} as shown in the figure. The range of the effective SFI is similar to the central 250 pc region SFI ($S_{\rm 250pc}$) that we reported in K20, which ranges from 2.3 to 46 $M_\odot$ yr^{-1} kpc^{-2} with a mean $S_{\rm 250pc}$ of 15 $M_\odot$ yr^{-1} kpc^{-2} for the same sample GPs. This is not unexpected, since the typical $r_{\rm cir,50}$ of our sample GPs is $\sim$ 0.3 kpc (i.e., Figure 4.1), so that the effective SFI is measured in a region that largely overlaps the central 250pc for most sample objects.

4.4.3 Correlations between UV Size and the Lyα Properties of GPs

In this section, we investigate the possible correlations between UV size and the Lyα properties such as EW(Lyα), $f_{esc}^{Ly\alpha}$, and L(Lyα) in our sample GPs. Figure 4.3 shows the correlations between $r_{\rm cir,50}$ and EW(Lyα), $f_{esc}^{Ly\alpha}$, and L(Lyα). Panel (a) shows the correlation between $r_{\rm cir,50}$ and EW(Lyα). Based on the distribution and the associated Spearman correlation coefficient (hereafter, $r_{\rm s}$) (p-value) of -0.429 (6×10^{-3}), there is a statistically significant anti-correlation between the two parameters such that a smaller UV size is preferred for a larger EW(Lyα).

The similar anti-correlation with the associated $r_{\rm s}$ (p-value) of -0.64 (0.03) was reported based on 12 local star-forming galaxies ($0.03 < z < 0.2$) from the Lyman alpha reference sample (LARS) (Guaita *et al.*, 2015). For high-z LAEs at $z \simeq 2.1$

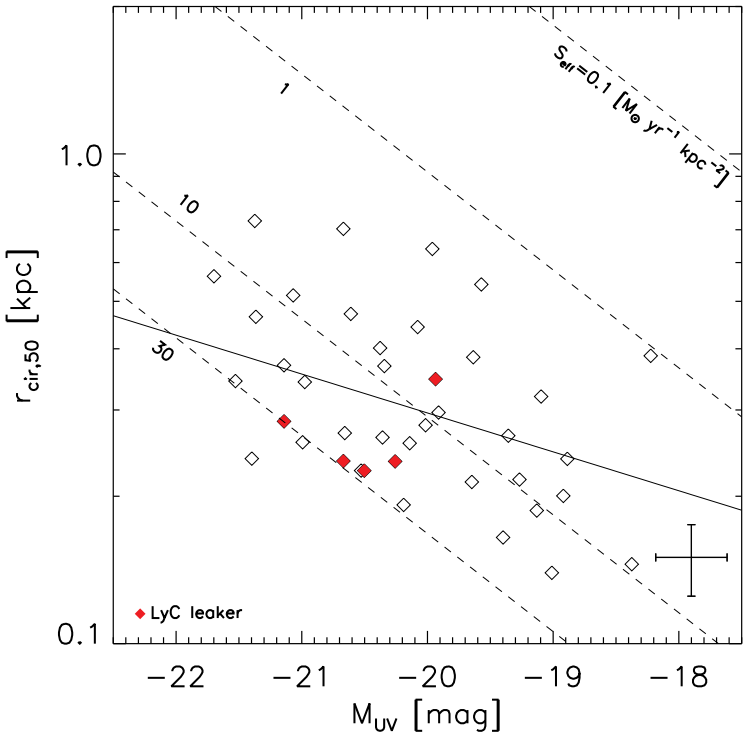

Figure 4.2: The UV-continuum size vs. luminosity relation of GPs. The linear-fit to the UV size-luminosity relation (i.e., Equation 4.2) shows the slope α of 0.23 ± 0.08 and the intercept r_0 of 0.37 ± 0.03 kpc, respectively. The solid line indicates the fitted line. The dashed lines indicate a constant effective SFI defined in Section 4.4.2. The comparison of individual data points with the constant effective SFI lines shows that GPs have SFI that is relatively high (by least 2 order of magnitude) compared to typical star-forming galaxies. (GPs have $S_{\rm eff} \gtrsim 1 M_\odot$ yr^{-1} kpc^{-2}, vs. $\sim 0.01 M_\odot$ yr^{-1} kpc^{-2} for typical low-redshift star forming galaxies). The typical measurement errors of 0.025 kpc and 0.28 mag in $r_{\rm cir,50}$ and UV magnitude are marked in bottom right. The red-filled diamonds are the five confirmed LyC leakers from Izotov *et al.* (2016).

and 3.1, there is a systematic trend seen such that high EW(Lyα) sample LAEs have a smaller median UV size compared to that of low EW(Lyα) sample LAEs (i.e., Bond *et al.*, 2012). Also, a linear-fit to the UV size and EW(Lyα) relation for a sample of high-z LAEs at $2 \lesssim z \lesssim 6$ showing a negative slope of -3.5 by Paulino-Afonso *et al.* (2018) seems qualitatively consistent with the anti-correlation shown in our sample GPs.

A correlation between $r_{\rm cir,50}$ and $f_{esc}^{Ly\alpha}$ is shown in panel (b), which shows a qualitatively similar anti-correlation to that in panel (a). The associated $r_{\rm s}$ (p-value) is -0.358 (0.02). The distribution and the associated $r_{\rm s}$ seem to suggest that a smaller UV size is preferred for larger $f_{esc}^{Ly\alpha}$. The same correlation was investigated based on the 12 LARS sample galaxies, although their $r_{\rm s}$ (p-value) of -0.22 (0.48) is not statistically significant (Guaita *et al.*, 2015).

Panel (c) shows the correlation between $r_{\rm cir,50}$ and L(Lyα). First, we note that one galaxy (GP ID 0339-0725) is omitted from this panel only, since it has no reported L(Lyα) in Y17. Compared to the other correlations examined above with EW(Lyα) and $f_{esc}^{Ly\alpha}$, L(Lyα) does not show a statistically significant anti-correlation with $r_{\rm cir,50}$, as the associated $r_{\rm s}$ (p-value) is only -0.216 (0.2). Nonetheless, it also seems evident that the large $r_{\rm cir,50}$ is not preferred for high L(Lyα) either, as a previous study (Paulino-Afonso *et al.*, 2018) shows a negative slope -0.51 of the linear fit to the UV size and L(Lyα) relation based on a sample of high-z LAEs.

The five confirmed LyC leakers in our sample GPs are marked as the red diamonds in Figure 4.3. Due to their high values of EW(Lyα), $f_{esc}^{Ly\alpha}$, and L(Lyα) (Y17), and relatively small $r_{\rm cir,50}$ compared to the sizes of the entire sample GPs, the confirmed LyC leakers occupy the top left of each panel (that is, small $r_{\rm cir,50}$ and large EW(Lyα) (panel (a)), $f_{esc}^{Ly\alpha}$ (panel (b)), and L(Lyα)(panel (c)), respectively).

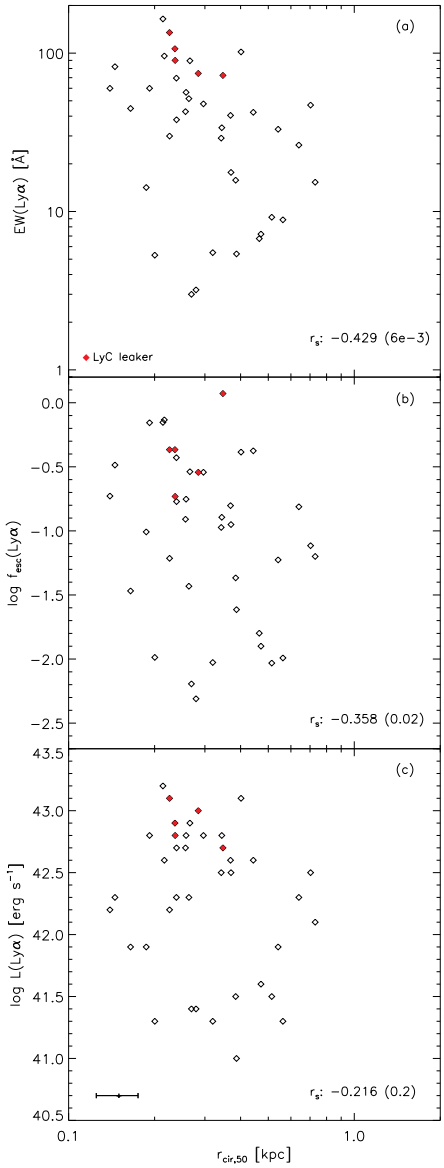

Figure 4.3: The correlations between $r_{\rm cir,50}$ vs. EW(Lyα) (panel (a)), $f_{esc}^{Ly\alpha}$ (panel (b)), and L(Lyα) (panel (c)). The format is the same as in Figure 4.2. The associated $r_{\rm s}$ values (p-values) are shown in bottom right of each panel. Note that the presented Lyα properties (i.e., EW(Lyα), $f_{esc}^{Ly\alpha}$, and L(Lyα)) largely show anti-correlations with $r_{\rm cir,50}$ in our sample GPs. The horizontal error bar in panel (c) indicates the typical measurement uncertainties of 0.025 kpc in $r_{\rm cir,50}$. The typical measurement uncertainties of the adopted EW(Lyα), $f_{esc}^{Ly\alpha}$, and L(Lyα) from Y17 are $\sim$ 15% mainly dominated by the systematic error.

4.4.4 The Size of GPs Compared to High-z LAEs

Malhotra et al. (2012) predict that the sizes of Lyα galaxies should be similar at all redshifts, so GPs should have similar sizes to high-z galaxies. Shibuya et al. 2019, however, predict that the sizes of Lyα galaxies should evolve with redshift as $r_{\rm cir,50} \propto (1+z)^{\beta}$ with (β) values of -1.37, similar to those of Lyman Break Galaxies (LBGs). At redshift of GPs ($z = 0.1 - 0.3$) these predictions differ by a factor of 10. But the average size of Lyα galaxies seems to *decrease* by a factor of 3 instead of increasing by a factor of 10.

The left panel of Figure 4.4 shows the compilation of the median physical sizes of our sample GPs and high-z LAEs as a function of redshift. For the sizes of high-z LAEs at $2 \lesssim z \lesssim 7$, we refer to previous studies (i.e., Malhotra *et al.*, 2012; Bond *et al.*, 2012; Jiang *et al.*, 2013; Paulino-Afonso *et al.*, 2018; Shibuya *et al.*, 2019; Ritondale *et al.*, 2019). The median size of our sample GPs (i.e., the filled diamond) does not follow the predicted size growth evolution of either LAEs (i.e., the dashed line) or LBGs as suggested by previous studies (i.e., Bouwens et al. 2004 for LBGs and Shibuya et al. 2019 for LAEs)— the plotted size evolution curves of LAEs and LBGs in the figure show the reported power-law fitting slope (β) values of -1.37 ± 0.65 and -1.05 ± 0.21 in the relation of $r_{\rm cir,50} \propto (1+z)^{\beta}$ for high-z LAEs and LBGs, respectively. Also, to derive the intercept of each size evolution curve we use the reported size at $z \sim 3.5$ (for LAEs) and at $z \sim 5$ (for LBGs), respectively from the previous studies (see Figure 9 of Shibuya *et al.* (2019) for LAEs and Figure 4 of Bouwens *et al.* (2004) for LBGs for details).

In particular, the median size of 0.284 kpc of our sample GPs is approximately an order of magnitude smaller than predicted using the LAE size evolution models from Shibuya *et al.* (2019). Our size measurement uncertainties are typically ~ 0.03 kpc

and cannot explain the discrepancy. This size difference does not change significantly even if we divided our sample GPs depending on the specific $L_{\rm UV}$ and/or EW(Lyα) bins similar to previous studies for the size of LAEs. For example, a subset of our sample with luminosities $0.3 < L/L_{*,z=3} < 1$ and EW(Lyα) $> 20\mathring{A}$ contains 16 GPs whose median size is 0.30 ± 0.15 kpc, indistinguishable from the result for our full sample. The mean and median sizes of our GP sub-samples with various different $L_{\rm UV}$ and EW(Lyα) cuts are listed in Table 2.2.

On average GPs show radii that are a factor of ~ 3 smaller compared to high-z LAEs (i.e., 0.284 kpc vs. ~ 1 kpc). This difference is due to both the angular resolution of the HST instruments which would increase as (1+z) for the same rest wavelength, and also due to the angular diameter distance increase with redshift. The spatial resolution for different instruments is shown in the right panel of Figure 4.4. If we assume that the sizes of LAEs is unchanged with redshift and convolve the median GPs radius of 0.284 kpc with the typical PSF FWHM of $0.09''$ of ACS/WFC instrument or the typical PSF FWHM of $0.13''$ of WFC3/IR, the measured radii of high-z LAEs are consistent with the radii of GPs. In the right panel of Figure 4.4 we show the results of convolving measured median angular size of GPs (black diamond) with three different PSF FWHM of different instruments (that is, COS/NUV (blue diamond), ACS/WFC (green diamond), and WFC3/IR (orange diamond)) to show the effects of different PSF FWHM on the measured size of galaxies.

This result is supported by measurements of the UV continuum size for lensed LAEs at $z = 2$–3 by Ritondale *et al.* (2019), who find $r_{\rm maj} = 0.561^{+0.013}_{-0.110}$ kpc, with the corresponding circularized size of 0.403 ± 0.213 kpc (the open circle in the left panel of Figure 4.4). This measurement is ~ 2.5 times smaller than the sizes measured for non-lensed LAEs at similar redshifts, and broadly comparable to the sizes of GPs, suggesting again that spatial resolution limits size measurements for high-redshift

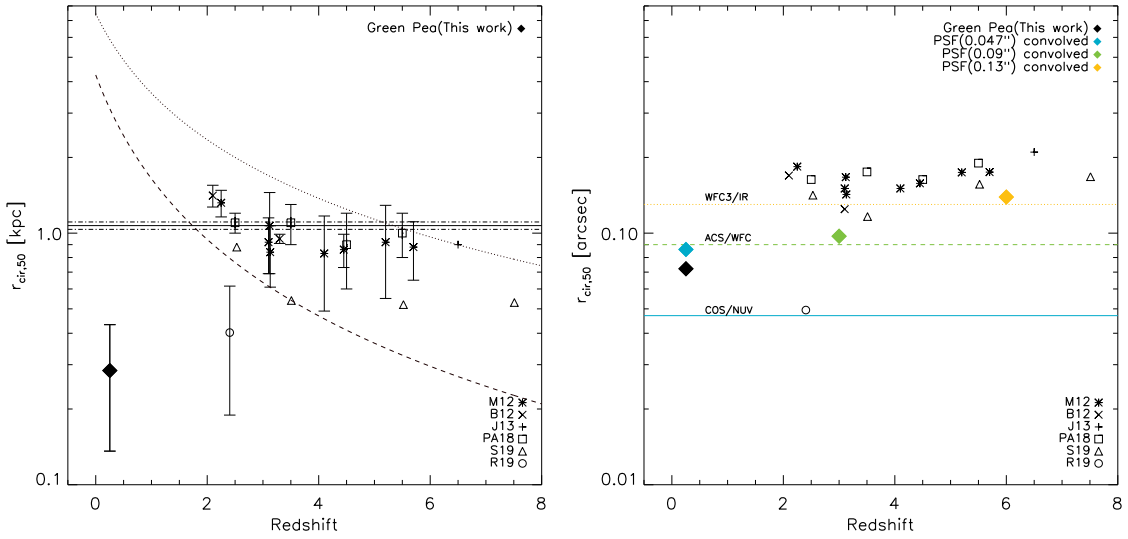

Figure 4.4: Left: The median UV-continuum size of sample GPs (the filled diamond at $z \sim 0.25$) compared to those of high-z LAEs. The sizes of high-z LAEs are from the literature (asterisk: Malhotra et al. (2012; M12), x mark: Bond et al. (2012; B12), cross: Jiang et al. (2013; J13), square: Paulino-Afonso et al. (2018; PA18), triangle: Shibuya et al. (2019; S19), and circle: Ritondale et al. (2019; R19)). The associated error bar indicates the 1σ standard deviation of size distribution of respective sample galaxies except for that of R19 which shows the uncertainties derived from random MCMC realizations to quantify errors of their size measurements of lensed LAEs. The data point for B12 for the $z = 3.1$ sample LAEs is shifted by 0.2 in x-axis for clarity. The solid horizontal line is the weighted mean size of the combined sample LAEs of M12 and PA18, and the dot-dashed lines are the associated weighted standard deviation of the weighted mean size. The dashed line is the predicted size evolution of LAEs based on S19. The dotted line is the predicted size evolution of LBGs from Bouwens *et al.* (2004). Our sample GPs do not follow either of these predicted size evolution models. The small median size of sample GPs dose not change significantly even if the sample GPs are divided into specific $L_{\rm UV}$ and EW(Lyα) bins as listed in Table 2. See the text for detail. Right: Same as the left panel, but for the corresponding angular sizes of GPs and high-z LAEs that are PSF-convolved in quadrature, except for the size of lensed LAEs (circle). The typical PSF FWHM of different *HST* instrument filters are marked as the colored horizontal lines. The blue, green, and orange diamonds are the PSF-convolved angular sizes of original median physical size of sample GPs (black diamond) by employing the different PSF FWHM indicated by each corresponding color. Note that the PSF-convolved angular sizes of GPs and high-z LAEs are largely constant.

LAEs.

4.5 Summary and Conclusions

In this study, we have measured the UV-continuum size and luminosity of a sample of 40 GPs. As GPs are some of the best local analogs to high-z LAEs, their physical proximity and the high spatial resolution (0.0235 arcsec pixel^{-1}) of COS/NUV images have enabled us to study the UV size and luminosity properties of LAEs in local universe and compare with those of high-z LAEs in detail. The main results are summarized as follows.

- GPs show compact sizes with a median $r_{\rm cir,50}$ of 0.284 kpc $\pm$ 0.15 kpc. The size distribution (Figure 4.1) is narrow (with its semi-interquartile range of 0.085 kpc) and is well-fitted by a log-normal distribution with the associated width $\sigma_{\ln(\rm r_{cir,50})}$ of 0.41. While the log-normal shape of the size distribution of GPs is largely consistent with other types of star-forming galaxies, the peak ($r_{\rm cir,50}$ at $\simeq$ 0.3 kpc) of the distribution is smaller due to the compact sizes of GPs.

- The UV size-luminosity relation of GPs (Figure 4.2) shows a fitted slope of 0.23 ± 0.08 and an intercept r_0 at $M_{\rm UV} = -21$ of 0.37 $\pm$0.03 kpc. The fitted slope value is broadly consistent with those of high-z LAEs and LBGs, and local late-type galaxies ($0.15 \lesssim \alpha \lesssim 0.35$) within the uncertainties. Also, the effective SFI of our sample GPs shown in the size-luminosity relation indicates relatively high SFI for GPs (1$-$30 $M_\odot$ yr^{-1} kpc^{-2}), exceeding the typical SFI of star-forming galaxies by 2 orders of magnitude or more.

- There are anti-correlations between UV-continuum size ($r_{\rm cir,50}$), EW(Lyα), $f_{esc}^{Ly\alpha}$, and L(Lyα) in sample GPs (Figure 4.3). In particular, the anti-correlations between $r_{\rm cir,50}$, EW(Lyα), and $f_{esc}^{Ly\alpha}$are statistically significant, and suggest that

small UV-continuum sizes are associated with Lyα galaxies.

- The size comparison of sample GPs with high-z LAEs (Figure 4.4) shows that the typical size of GPs (i.e., 0.284 kpc) is a factor of ~ 3 smaller than those of high-z LAEs ($\simeq 1$ kpc) over a redshift range $2 \lesssim z \lesssim 6$. Also, the compact size of GPs does not seem to follow the predicted size evolution of either high-z LAEs or LBGs, rather showing a factor of ~ 10 smaller size than the predicted size at low redshits.

- The smaller size of our sample GPs compared to those of high-z LAEs, is however, due to the different seeing effects between low-z GPs and high-z LAEs (Figure 4). Once the different seeing effects are properly taken into account, their sizes are consistent with negligible evolution.

All in all, our UV size and luminosity analysis of GP galaxies suggests that a compact size is crucial for escape of Lyα photons, and that LAEs show constant characteristic size independent of their redshift.

Table 4.1: The Measured Parameters of Sample Galaxies.

Green Pea ID[a]	SDSS ObjID[b]	m_{UV} [c,d] (mag)	M_{UV} [e,d] (mag)	$r_{cir,50}$ [f,g] (arcsec)	$r_{cir,50}$ [h,g] (kpc)	$r_{cir,p}$ [i,g] (arcsec)	$r_{cir,p}$ [j,g] (kpc)	b/a [k]	A_{int} [l] (mag)	A_{MW} [m] (mag)	k [n] (mag)
0055-0021	1237663783666581565	20.42 ± 0.51	-20.02 ± 0.51	0.098 ± 0.016	0.279 ± 0.046	0.247 ± 0.062	0.706 ± 0.179	0.69 ± 0.02	0.850	0.184	0.123
0303-0759	1237652900231053501	20.95 ± 0.23	-19.13 ± 0.23	0.066 ± 0.002	0.187 ± 0.007	0.157 ± 0.011	0.443 ± 0.030	0.78 ± 0.02	0	0.716	0.128
0339-0725	1237649961383493869	20.12 ± 0.30	-21.37 ± 0.30	0.115 ± 0.008	0.465 ± 0.032	0.247 ± 0.027	0.998 ± 0.110	0.63 ± 0.01	0.387	0.447	-0.043
0749+3337	1237674366992646574	20.32 ± 0.34	-21.70 ± 0.34	0.135 ± 0.012	0.563 ± 0.049	0.250 ± 0.032	1.042 ± 0.133	0.45 ± 0.01	0.832	0.405	-0.065
0751+1638	1237673807042708368	21.93 ± 0.46	-19.64 ± 0.46	0.094 ± 0.011	0.384 ± 0.046	0.220 ± 0.044	0.899 ± 0.180	0.65 ± 0.01	0.609	0.264	-0.050
0805+0925	1237667729656905788	22.13 ± 0.46	-21.07 ± 0.46	0.108 ± 0.017	0.514 ± 0.079	0.216 ± 0.047	1.026 ± 0.223	0.76 ± 0.04	1.686	0.154	-0.160
0815+2156	1237664668421849521	20.92 ± 0.15	-18.37 ± 0.15	0.059 ± 0.001	0.145 ± 0.003	0.140 ± 0.006	0.349 ± 0.015	0.81 ± 0.01	0.054	0.298	0.173
0822+2241	1237664092897083648	20.86 ± 0.31	-20.36 ± 0.31	0.075 ± 0.004	0.264 ± 0.016	0.183 ± 0.020	0.642 ± 0.071	0.89 ± 0.02	0.781	0.329	0.035
0911+1831	1237667429018697946	20.56 ± 0.16	-20.99 ± 0.16	0.064 ± 0.002	0.258 ± 0.006	0.147 ± 0.007	0.597 ± 0.027	0.65 ± 0.01	0.686	0.206	-0.046
0917+3152	1237661382232768711	20.60 ± 0.21	-21.40 ± 0.21	0.054 ± 0.002	0.239 ± 0.010	0.112 ± 0.007	0.497 ± 0.031	0.88 ± 0.02	0.783	0.143	-0.111
0925+1403[o]	1237671262812897597	21.19 ± 0.14	-20.67 ± 0.14	0.053 ± 0.001	0.236 ± 0.004	0.127 ± 0.005	0.567 ± 0.021	0.92 ± 0.02	0.555	0.225	-0.112
0926+4428	1237657630590107652	20.12 ± 0.41	-19.91 ± 0.41	0.097 ± 0.012	0.296 ± 0.037	0.223 ± 0.039	0.678 ± 0.118	0.67 ± 0.01	0.292	0.132	0.099
0927+1740	1237667536393142625	21.30 ± 0.41	-20.61 ± 0.41	0.109 ± 0.012	0.471 ± 0.051	0.235 ± 0.041	1.018 ± 0.177	0.77 ± 0.02	0.742	0.220	-0.090
1009+2916	1237665126921011548	21.46 ± 0.31	-18.89 ± 0.31	0.067 ± 0.005	0.238 ± 0.016	0.140 ± 0.015	0.500 ± 0.053	0.65 ± 0.02	0	0.163	0.024
1018+4106	1237661851459584247	21.28 ± 0.40	-19.57 ± 0.40	0.144 ± 0.021	0.541 ± 0.078	0.270 ± 0.047	1.014 ± 0.176	0.82 ± 0.02	0.380	0.099	-0.002
1025+3622	1237664668435677291	19.12 ± 0.35	-19.96 ± 0.35	0.283 ± 0.032	0.640 ± 0.071	0.625 ± 0.097	1.414 ± 0.219	0.51 ± 0.01	0.338	0.082	0.201
1032+2717	1237667211592794251	21.22 ± 0.38	-19.10 ± 0.38	0.100 ± 0.010	0.320 ± 0.032	0.213 ± 0.032	0.682 ± 0.104	0.92 ± 0.02	0.384	0.150	0.077
1054+5238	1237658801495474207	19.80 ± 0.22	-21.14 ± 0.22	0.094 ± 0.004	0.370 ± 0.017	0.194 ± 0.014	0.765 ± 0.055	0.93 ± 0.01	0.280	0.107	-0.029
1122+6154	1237655464839479591	21.52 ± 0.26	-19.01 ± 0.26	0.042 ± 0.002	0.140 ± 0.005	0.104 ± 0.008	0.348 ± 0.027	0.75 ± 0.02	0.514	0.058	0.056
1133+6514	1237651067351073064	20.59 ± 0.24	-20.08 ± 0.24	0.116 ± 0.006	0.443 ± 0.021	0.239 ± 0.018	0.911 ± 0.070	0.74 ± 0.01	0.162	0.079	-0.010
1137+3524	1237665129613885585	19.77 ± 0.23	-20.34 ± 0.23	0.114 ± 0.006	0.369 ± 0.018	0.240 ± 0.019	0.776 ± 0.060	0.44 ± 0.01	0.171	0.132	0.074
1152+3400[o]	1237665127467647162	20.95 ± 0.15	-21.14 ± 0.15	0.058 ± 0.001	0.284 ± 0.007	0.113 ± 0.005	0.551 ± 0.024	0.78 ± 0.01	0.480	0.143	-0.179
1205+2620	1237667321644908846	21.70 ± 0.30	-20.66 ± 0.30	0.055 ± 0.003	0.269 ± 0.016	0.127 ± 0.013	0.617 ± 0.064	0.80 ± 0.02	0.750	0.138	-0.180
1219+1526	1237661070336852109	20.37 ± 0.16	-19.65 ± 0.16	0.066 ± 0.002	0.214 ± 0.006	0.149 ± 0.007	0.483 ± 0.023	0.94 ± 0.01	0	0.190	0.072
1244+0216	1237671266571387104	20.16 ± 0.29	-20.67 ± 0.29	0.186 ± 0.011	0.703 ± 0.043	0.458 ± 0.048	1.734 ± 0.183	0.76 ± 0.01	0.251	0.179	-0.006
1249+1234	1237661817096962164	20.86 ± 0.19	-20.38 ± 0.19	0.099 ± 0.003	0.401 ± 0.014	0.198 ± 0.012	0.806 ± 0.047	0.71 ± 0.01	0.343	0.217	-0.048
1333+6246[o]	1237651249891967264	21.45 ± 0.21	-19.94 ± 0.21	0.075 ± 0.002	0.347 ± 0.009	0.184 ± 0.011	0.853 ± 0.052	0.66 ± 0.01	0	0.140	-0.140
1339+1516	1237664292084318332	21.05 ± 0.25	-19.40 ± 0.25	0.052 ± 0.002	0.165 ± 0.008	0.109 ± 0.009	0.349 ± 0.028	0.89 ± 0.02	0.452	0.219	0.078
1424+4217	1237661360765730849	20.50 ± 0.26	-19.36 ± 0.26	0.086 ± 0.005	0.266 ± 0.014	0.191 ± 0.017	0.591 ± 0.051	0.81 ± 0.01	0.111	0.074	0.091
1428+1653	1237668297680683015	19.48 ± 0.27	-20.98 ± 0.27	0.112 ± 0.006	0.342 ± 0.017	0.278 ± 0.026	0.850 ± 0.079	0.81 ± 0.01	0.690	0.142	0.097
1429+0643	1237662268069511204	19.75 ± 0.35	-20.14 ± 0.35	0.087 ± 0.008	0.257 ± 0.023	0.195 ± 0.024	0.574 ± 0.072	0.82 ± 0.02	0.208	0.183	0.112
1440+4619	1237662301362978958	20.26 ± 0.26	-21.53 ± 0.26	0.077 ± 0.005	0.344 ± 0.020	0.169 ± 0.015	0.753 ± 0.067	0.76 ± 0.01	0.613	0.103	-0.111
1442-0209[o]	1237655498671849789	21.28 ± 0.19	-20.50 ± 0.19	0.051 ± 0.001	0.226 ± 0.006	0.112 ± 0.006	0.490 ± 0.028	0.76 ± 0.02	0.388	0.392	-0.099
1454+4528	1237662301900964026	21.20 ± 0.27	-20.53 ± 0.27	0.055 ± 0.003	0.226 ± 0.012	0.125 ± 0.011	0.515 ± 0.046	0.90 ± 0.02	0.691	0.303	-0.057
1457+2232	1237665549967294628	20.75 ± 0.20	-18.92 ± 0.20	0.077 ± 0.002	0.200 ± 0.006	0.194 ± 0.012	0.503 ± 0.031	0.97 ± 0.02	0.237	0.347	0.159
1503+3644[o]	1237661872417407304	21.47 ± 0.13	-20.26 ± 0.13	0.047 ± 0.001	0.236 ± 0.005	0.104 ± 0.004	0.519 ± 0.018	0.82 ± 0.01	0.031	0.111	-0.201
1514+3852	1237661362380734819	21.35 ± 0.24	-20.19 ± 0.24	0.040 ± 0.002	0.192 ± 0.007	0.099 ± 0.007	0.474 ± 0.032	0.69 ± 0.01	0	0.157	-0.164
1543+3446	1237662336790036887	21.70 ± 0.47	-18.22 ± 0.47	0.124 ± 0.018	0.387 ± 0.057	0.269 ± 0.058	0.842 ± 0.182	0.61 ± 0.02	0	0.214	0.087
1559+0841	1237662636912280219	22.05 ± 0.28	-19.27 ± 0.28	0.049 ± 0.003	0.216 ± 0.011	0.093 ± 0.008	0.409 ± 0.036	0.84 ± 0.02	0	0.282	-0.105
2237+1336	1237656495641788638	20.56 ± 0.41	-21.37 ± 0.41	0.166 ± 0.020	0.730 ± 0.088	0.381 ± 0.070	1.670 ± 0.309	0.90 ± 0.02	0.521	0.418	-0.099

[a] Green Pea IDs match those in Yang et al 2017.

[b] SDSS DR14 BestObjID.

[c] The measured apparent NUV magnitude.

[d] The associated errors are magnitude measurement uncertainties based on photon counting statistics (i.e., Poisson statistics) and propagation of the errors during the image calibration procedures such as flat-field correction.

[e] The extinction and k-corrected absolute UV magnitude at 1877 $\AA$.

[f] The circularized Petrosian half-light radius in the unit of arcsec.

[g] The associated errors are based on the associated flux measurement uncertainties.

[h] The circularized Petrosian half-light radius in the unit of kpc assuming the adopted cosmological parameters in Section 4.2.

[i] The circularized Petrosian radius in the unit of arcsec.

[j] The circularized Petrosian radius in the unit of kpc assuming the adopted cosmological parameters in Section 4.2.

[k] The apparent axis ratio and the associated uncertainties derived from the GALFIT surface brightness fitting in Section 4.3.2.

[l] The internal extinction correction derived in Kim et al. 2020 based on the Balmer decrement. Zero indicates that the observed ratio of Hα / Hβ is smaller than 2.86. See their section 2.3 and also Section2.2 of Yang et al. 2017b for details.

[m] The Milky Way extinction correction derived in Kim et al. 2020 based on the NASA/IPAC Galactic Dust Reddening and Extinction tool. See their section 2.3 for details.

[n] The k-correction derived in Kim et al. 2020 at 1877 $\AA$ assuming the UV slope of -2. See their section 2.3 for details.

[o] Confirmed Lyman continuum leakers identified by Izotov *et al.* (2016).

Table 4.2: The Representative UV Size of GP Sub-samples with Different Different $L_{\rm UV}$ and EW(Lyα) Criteria.

Criteria	No EW(Lyα) Cut	EW(Lyα) $>$ 20 Å
$L_{\rm UV}/L_{*,\rm z=3}$	(Number of Galaxies)	(Number of Galaxies)
0.08-0.3	(13)	(8)
Mean / Median	0.26 / 0.22 $\pm$ 0.12 kpc	0.24 / 0.22 $\pm$ 0.13 kpc
0.3-1	(19)	(16)
Mean / Median	0.34 / 0.28 $\pm$ 0.14 kpc	0.34 / 0.30 $\pm$ 0.15 kpc
1-1.9	(8)	(3)
Mean / Median	0.44 / 0.46 $\pm$ 0.16 kpc	0.29 / 0.28 $\pm$ 0.05 kpc
0.08-1.9	(40 = Full GP sample)	(27)
Mean / Median	0.33 / 0.28 $\pm$ 0.15 kpc	0.30 (0.26) $\pm$ 0.14 kpc

Chapter 5

CONCLUSIONS

In this dissertation, we investigated the three main studies of galaxy structural properties and their possible associations with star formation quenching mechanisms and Lyα escape mechanisms in galaxies. The relatively high spatial resolution of the *Hubble Space Telescope (HST)* images enables us to explore the galaxy structural properties such as size, surface density, and visually-classified morphology in detail.

In Chapter 2, we utilized both photometric and spectroscopic data from the *Hubble Space Telescope* to explore the relationships among 4000 Å break (D4000) strength, colors, stellar masses, and galaxy structural properties such as visually-classified morphology and stellar surface density. The galaxy sample consists of 352 galaxies with $\log(M_*/M_\odot) > 9.44$ at intermediate redshifts (i.e., $0.6 \lesssim z \lesssim 1.2$). For morphological information, we divided galaxies into four morphological types depending on the prominence of bulge component into spheroids, early-type disks, late-type disks, and irregulars. We first identified authentically quiescent galaxies in the $U-V$ vs. $V-J$ diagram based on their spectroscopic D4000 strengths. This spectroscopic identification is in good agreement with their photometrically-derived specific star formation rates (sSFR). Morphologically, $\sim$ 97 % of these newly identified quiescent galaxies have a prominent bulge component. However, not all of the bulge-dominated galaxies show the signature of quenching.

We further found that bulge-dominated galaxies show positive correlations among the D4000 strength, stellar mass, and the Sérsic index, while late-type disks do not show such strong positive correlations. Also, bulge-dominated galaxies are clearly separated into two main groups in the parameter space of sSFR vs. stellar mass and

stellar surface density, $\Sigma_{\rm e}$, while late-type disks and irregulars only show high sSFR. This split is directly linked to the 'blue cloud' and the 'red sequence' populations, and correlates with the associated central compactness indicated by $\Sigma_{\rm e}$. While star-forming massive late-type disks and irregulars (with D4000 < 1.5 and $\log(M_*/M_\odot) \gtrsim 10.5$) span a stellar mass range comparable to bulge-dominated galaxies, most have systematically lower $\Sigma_{\rm e} \lesssim 10^9 M_\odot {\rm kpc}^{-2}$. The Kormendy relation for spheroids shows that large D4000 (D4000 > 1.5) spheroids (thus, older luminosity-weighted average age of constituent stellar populations) have more concentrated stellar light profiles than low D4000 (D4000 > 1.5) spheroids. The results suggests that the presence of a bulge is a necessary but not sufficient requirement for quenching at intermediate redshifts.

In Chapter 3, we studied ultraviolet images of 40 Green Pea (GP) galaxies and 15 local Lyman Break Galaxy Analogs (LBAs) to understand the relation between Lyα photon escape and central UV photometric properties. Specifically, we measured star formation intensity (SFI, star formation rate per unit area) from the central 250 pc region ($S_{\rm 250pc}$) using the Cosmic Origins Spectrograph near-ultraviolet (COS/NUV) images from the *HST*. The images are Haar wavelet denoised to reduce the noise, and subsequently PSF-deconvolved to compensate for the different redshifts of sample galaxies. Also, Milky Way and internal extinction corrections and k-correction are applied.

The measured $S_{\rm 250pc}$ of sample GPs ranges from 2.3–46 $M_\odot$ yr^{-1} kpc^{-2}, with a mean of $15 M_\odot$ yr^{-1} kpc^{-2} and a standard deviation of 0.266 dex, forming a relatively narrow distribution. The sample LBAs show a similarly narrow distribution of $S_{\rm 250pc}$ (0.271 dex), though with a larger mean of 28 $M_\odot$ yr^{-1} kpc^{-2}.

We showed that while the Lyα properties of GPs such as the Lyα equivalent width (EW(Lyα)) and the Lyα escape fraction ($f_{esc}^{Ly\alpha}$) are not significantly correlated with

the central SFI ($S_{250\mathrm{pc}}$), both EW(Lyα) and $f_{esc}^{Ly\alpha}$ are positively correlated with the ratio of surface brightness to galaxy stellar mass ($S_{250\mathrm{pc}}/M_{\mathrm{star}}$) that can be regarded as specific star formation intensity (sSFI), with the associated Spearman correlation coefficients (p-values) of 0.702 (1×10^{-8}) and 0.529 (5×10^{-4}) with EW(Lyα) and $f_{esc}^{Ly\alpha}$, respectively. If galaxy stellar mass is considered a proxy for gravitational potentials, these correlations suggest a scenario where intense central star formation can drive a galactic wind in galaxies with relatively shallow gravitational potential wells, thus clearing channels for the escape of Lyα photons.

In Chapter 4, we measured the UV-continuum size and luminosity of a sample of 40 Green Pea (GP) galaxies at $0.1 \lesssim z \lesssim 0.35$ to investigate their UV photometric properties and possible associations with Lyα escape mechanisms. We utilized the same processed COS/NUV images as in Chapter 3. To measure the size of galaxies, we adopted the definition of Petrosian radius for our size measurements.

The measured circularized half-light radius ($r_{\mathrm{cir},50}$) of GPs shows compact sizes with a median of 0.284 kpc and a standard deviation of 0.15 kpc. The size distribution of sample GPs shows a relatively narrow distribution with its semi-interquartile range of 0.085 kpc. We showed that while the log-normal shape of the size distribution and the slope of the size-luminosity relation of GPs are largely consistent with those of other star-forming galaxies at low and high redshifts, the peak of the size distribution and the intercept of the size-luminosity relation of GPs are noticeably smaller than typical star-forming galaxies at similar redshifts due to compact typical sizes of GPs.

Also, the $r_{\mathrm{cir},50}$ shows anti-correlations with the Lyα equivalent width, the Lyα escape faction, and the Lyα luminosity, suggesting that small UV-continuum radii are crucial for Lyα emission. The size comparison of GPs with high-redshift Lyman Alpha Emitters (high-z LAEs) shows that GPs and high-z LAEs have similar sizes, once spatial resolution effects are properly considered. The results in this chapter

show that a compact size is crucial for escape of Lyα photons, and that LAEs show constant characteristic size independent of their redshift.

Therefore, the three studies presented in this dissertation emphasize the importance of galaxy structural parameters in star formation quenching and in Lyα escape.

Abramson, L. E., D. D. Kelson, A. Dressler, B. Poggianti, M. D. Gladders, J. Oemler, Augustus and B. Vulcani, "The Mass-independence of Specific Star Formation Rates in Galactic Disks", ApJL 785, 2, L36 (2014).

Abramson, L. E. and T. Morishita, "Must Star-forming Galaxies Rapidly Get Denser before They Quench?", ApJ 858, 1, 40 (2018).

Ahn, S.-H., H.-W. Lee and H. M. Lee, "P Cygni type Lyα from starburst galaxies", MNRAS 340, 3, 863–869 (2003).

Alexandroff, R. M., T. M. Heckman, S. Borthakur, R. Overzier and C. Leitherer, "Indirect Evidence for Escaping Ionizing Photons in Local Lyman Break Galaxy Analogs", ApJ 810, 2, 104 (2015).

Alpaslan, M., S. Driver, A. S. G. Robotham, D. Obreschkow, E. Andrae, M. Cluver, L. S. Kelvin, R. Lange, M. Owers, E. N. Taylor, S. K. Andrews, S. Bamford, J. Bland-Hawthorn, S. Brough, M. J. I. Brown, M. Colless, L. J. M. Davies, E. Eardley, M. W. Grootes, A. M. Hopkins, R. Kennedy, J. Liske, M. A. Lara-López, Á. R. López-Sánchez, J. Loveday, B. F. Madore, S. Mahajan, M. Meyer, A. Moffett, P. Norberg, S. Penny, K. A. Pimbblet, C. C. Popescu, M. Seibert and R. Tuffs, "Galaxy And Mass Assembly (GAMA): trends in galaxy colours, morphology, and stellar populations with large-scale structure, group, and pair environments", MNRAS 451, 3, 3249–3268 (2015).

Amorín, R. O., E. Pérez-Montero and J. M. Vílchez, "On the Oxygen and Nitrogen Chemical Abundances and the Evolution of the "Green Pea" Galaxies", ApJL 715, 2, L128–L132 (2010).

Anders, P. and U. Fritze-v Alvensleben, "Spectral and photometric evolution of young stellar populations: The impact of gaseous emission at various metallicities", A&A 401, 1063–1070 (2003).

Anderson, T. W., "On the Distribution of the Two-Sample Cramér-von Mises Criterion", Annals of Mathematical Statistics. Institute of Mathematical Statistics 33, 1148–1159 (1962).

Bait, O., S. Barway and Y. Wadadekar, "On the interdependence of galaxy morphology, star formation and environment in massive galaxies in the nearby Universe", MNRAS 471, 3, 2687–2702 (2017).

Baldry, I. K., K. Glazebrook, J. Brinkmann, Ž. Ivezić, R. H. Lupton, R. C. Nichol and A. S. Szalay, "Quantifying the Bimodal Color-Magnitude Distribution of Galaxies", ApJ 600, 2, 681–694 (2004).

Balogh, M. L., S. L. Morris, H. K. C. Yee, R. G. Carlberg and E. Ellingson, "Differential Galaxy Evolution in Cluster and Field Galaxies at z˜0.3", ApJ 527, 1, 54–79 (1999).

Barnes, J. and G. Efstathiou, "Angular Momentum from Tidal Torques", ApJ 319, 575 (1987).

Barro, G., S. M. Faber, D. C. Koo, A. Dekel, J. J. Fang, J. R. Trump, P. G. Pérez-González, C. Pacifici, J. R. Primack, R. S. Somerville, H. Yan, Y. Guo, F. Liu, D. Ceverino, D. D. Kocevski and E. McGrath, "Structural and Star-forming Relations since z 3: Connecting Compact Star-forming and Quiescent Galaxies", ApJ 840, 1, 47 (2017).

Bassett, R., C. Papovich, J. M. Lotz, E. F. Bell, S. L. Finkelstein, J. A. Newman, K.-V. Tran, O. Almaini, C. Lani, M. Cooper, D. Croton, A. Dekel, H. C. Ferguson, D. D. Kocevski, A. M. Koekemoer, D. C. Koo, E. J. McGrath, D. H. McIntosh and R. Wechsler, "CANDELS Observations of the Environmental Dependence of the Color-Mass-Morphology Relation at z = 1.6", ApJ 770, 1, 58 (2013).

Bell, E. F. and R. S. de Jong, "The stellar populations of spiral galaxies", MNRAS 312, 3, 497–520 (2000).

Bell, E. F., A. van der Wel, C. Papovich, D. Kocevski, J. Lotz, D. H. McIntosh, J. Kartaltepe, S. M. Faber, H. Ferguson, A. Koekemoer, N. Grogin, S. Wuyts, E. Cheung, C. J. Conselice, A. Dekel, J. S. Dunlop, M. Giavalisco, J. Herrington, D. C. Koo, E. J. McGrath, D. de Mello, H.-W. Rix, A. R. Robaina and C. C. Williams, "What Turns Galaxies Off? The Different Morphologies of Star-forming and Quiescent Galaxies since z ~2 from CANDELS", ApJ 753, 2, 167 (2012).

Bell, E. F., C. Wolf, K. Meisenheimer, H.-W. Rix, A. Borch, S. Dye, M. Kleinheinrich, L. Wisotzki and D. H. McIntosh, "Nearly 5000 Distant Early-Type Galaxies in COMBO-17: A Red Sequence and Its Evolution since z~1", ApJ 608, 2, 752–767 (2004).

Bernardi, M., R. K. Sheth, J. Annis, S. Burles, D. J. Eisenstein, D. P. Finkbeiner, D. W. Hogg, R. H. Lupton, D. J. Schlegel, M. SubbaRao, N. A. Bahcall, J. P. Blakeslee, J. Brinkmann, F. J. Castander, A. J. Connolly, I. Csabai, M. Doi, M. Fukugita, J. Frieman, T. Heckman, G. S. Hennessy, Ž. Ivezić, G. R. Knapp, D. Q. Lamb, T. McKay, J. A. Munn, R. Nichol, S. Okamura, D. P. Schneider, A. R. Thakar and D. G. York, "Early-type Galaxies in the Sloan Digital Sky Survey. II. Correlations between Observables", AJ 125, 4, 1849–1865 (2003a).

Bernardi, M., R. K. Sheth, J. Annis, S. Burles, D. J. Eisenstein, D. P. Finkbeiner, D. W. Hogg, R. H. Lupton, D. J. Schlegel, M. SubbaRao, N. A. Bahcall, J. P. Blakeslee, J. Brinkmann, F. J. Castander, A. J. Connolly, I. Csabai, M. Doi, M. Fukugita, J. Frieman, T. Heckman, G. S. Hennessy, Ž. Ivezić, G. R. Knapp, D. Q. Lamb, T. McKay, J. A. Munn, R. Nichol, S. Okamura, D. P. Schneider, A. R. Thakar and D. G. York, "Early-Type Galaxies in the Sloan Digital Sky Survey. I. The Sample", AJ 125, 4, 1817–1848 (2003b).

Bershady, M. A., A. Jangren and C. J. Conselice, "Structural and Photometric Classification of Galaxies. I. Calibration Based on a Nearby Galaxy Sample", AJ 119, 6, 2645–2663 (2000).

Bessell, M. S., F. Castelli and B. Plez, "Model atmospheres broad-band colors, bolometric corrections and temperature calibrations for O - M stars", A&A 333, 231–250 (1998).

Blanton, M. R., D. W. Hogg, N. A. Bahcall, I. K. Baldry, J. Brinkmann, I. Csabai, D. Eisenstein, M. Fukugita, J. E. Gunn, Ž. Ivezić, D. Q. Lamb, R. H. Lupton, J. Loveday, J. A. Munn, R. C. Nichol, S. Okamura, D. J. Schlegel, K. Shimasaku, M. A. Strauss, M. S. Vogeley and D. H. Weinberg, "The Broadband Optical Properties of Galaxies with Redshifts 0.02<z<0.22", ApJ 594, 1, 186–207 (2003).

Bluck, A. F. L., J. T. Mendel, S. L. Ellison, J. Moreno, L. Simard, D. R. Patton and E. Starkenburg, "Bulge mass is king: the dominant role of the bulge in determining the fraction of passive galaxies in the Sloan Digital Sky Survey", MNRAS 441, 1, 599–629 (2014).

Bond, N. A., E. Gawiser, C. Gronwall, R. Ciardullo, M. Altmann and K. Schawinski, "Sizes of LYα-emitting Galaxies and Their Rest-frame Ultraviolet Components at z = 3.1", ApJ 705, 1, 639–649 (2009).

Bond, N. A., E. Gawiser, L. Guaita, N. Padilla, C. Gronwall, R. Ciardullo and K. Lai, "Evolution in the Continuum Morphological Properties of Lyα-emitting Galaxies from z = 3.1 to z = 2.1", ApJ 753, 2, 95 (2012).

Bouwens, R. J., G. D. Illingworth, J. P. Blakeslee, T. J. Broadhurst and M. Franx, "Galaxy Size Evolution at High Redshift and Surface Brightness Selection Effects: Constraints from the Hubble Ultra Deep Field", ApJL 611, 1, L1–L4 (2004).

Bower, R. G., J. R. Lucey and R. S. Ellis, "Precision photometry of early-type galaxies in the Coma and Virgo clusters : a test of the universality of the colour-magnitude relation - II. Analysis.", MNRAS 254, 601 (1992).

Bremer, M. N., S. Phillipps, L. S. Kelvin, R. De Propris, R. Kennedy, A. J. Moffett, S. Bamford, L. J. M. Davies, S. P. Driver, B. Häußler, B. Holwerda, A. Hopkins, P. A. James, J. Liske, S. Percival and E. N. Taylor, "Galaxy and Mass Assembly (GAMA): Morphological transformation of galaxies across the green valley", MNRAS 476, 1, 12–26 (2018).

Brennan, R., V. Pandya, R. S. Somerville, G. Barro, A. F. L. Bluck, E. N. Taylor, S. Wuyts, E. F. Bell, A. Dekel, S. r. Faber, H. C. Ferguson, A. M. Koekemoer, P. Kurczynski, D. H. McIntosh, J. A. Newman and J. Primack, "The relationship between star formation activity and galaxy structural properties in CANDELS and a semi-analytic model", MNRAS 465, 1, 619–640 (2017).

Brennan, R., V. Pandya, R. S. Somerville, G. Barro, E. N. Taylor, S. Wuyts, E. F. Bell, A. Dekel, H. C. Ferguson, D. H. McIntosh, C. Papovich and J. Primack, "Quenching and morphological transformation in semi-analytic models and CANDELS", MNRAS 451, 3, 2933–2956 (2015).

Brinchmann, J., S. Charlot, S. D. M. White, C. Tremonti, G. Kauffmann, T. Heckman and J. Brinkmann, "The physical properties of star-forming galaxies in the low-redshift Universe", MNRAS 351, 4, 1151–1179 (2004).

Bruzual, G. and S. Charlot, "Stellar population synthesis at the resolution of 2003", MNRAS 344, 4, 1000–1028 (2003).

Bruzual A., G., "Spectral evolution of galaxies. I. Early-type systems.", ApJ 273, 105–127 (1983).

Calzetti, D., L. Armus, R. C. Bohlin, A. L. Kinney, J. Koornneef and T. Storchi-Bergmann, "The Dust Content and Opacity of Actively Star-forming Galaxies", ApJ 533, 2, 682–695 (2000).

Cardamone, C., K. Schawinski, M. Sarzi, S. P. Bamford, N. Bennert, C. M. Urry, C. Lintott, W. C. Keel, J. Parejko, R. C. Nichol, D. Thomas, D. Andreescu, P. Murray, M. J. Raddick, A. Slosar, A. Szalay and J. Vandenberg, "Galaxy Zoo Green Peas: discovery of a class of compact extremely star-forming galaxies", MNRAS 399, 3, 1191–1205 (2009).

Carollo, C. M., T. J. Bschorr, A. Renzini, S. J. Lilly, P. Capak, A. Cibinel, O. Ilbert, M. Onodera, N. Scoville, E. Cameron, B. Mobasher, D. Sanders and Y. Taniguchi, "Newly Quenched Galaxies as the Cause for the Apparent Evolution in Average Size of the Population", ApJ 773, 2, 112 (2013).

Carollo, C. M., A. Cibinel, S. J. Lilly, A. Pipino, S. Bonoli, A. Finoguenov, F. Miniati, P. Norberg and J. D. Silverman, "ZENS. IV. Similar Morphological Changes Associated with Mass Quenching and Environment Quenching and the Relative Importance of Bulge Growth versus the Fading of Disks*", ApJ 818, 2, 180 (2016).

Cen, R., "Physics of Prodigious Lyman Continuum Leakers", ApJL 889, 1, L22 (2020).

Chabrier, G., "Galactic Stellar and Substellar Initial Mass Function", PASP 115, 809, 763–795 (2003).

Cheung, E., S. M. Faber, D. C. Koo, A. A. Dutton, L. Simard, E. J. McGrath, J. S. Huang, E. F. Bell, A. Dekel, J. J. Fang, S. Salim, G. Barro, K. Bundy, A. L. Coil, M. C. Cooper, C. J. Conselice, M. Davis, A. Domínguez, S. A. Kassin, D. D. Kocevski, A. M. Koekemoer, L. Lin, J. M. Lotz, J. A. Newman, A. C. Phillips, D. J. Rosario, B. J. Weiner and C. N. A. Willmer, "The Dependence of Quenching upon the Inner Structure of Galaxies at 0.5 <= z < 0.8 in the DEEP2/AEGIS Survey", ApJ 760, 2, 131 (2012).

Ciambur, B. C., G. Kauffmann and S. Wuyts, "On the evolution of the bi-modal distribution of galaxies in the plane of specific star formation rate versus stellar mass", MNRAS 432, 3, 2488–2495 (2013).

Cole, S. and C. Lacey, "The structure of dark matter haloes in hierarchical clustering models", MNRAS 281, 716 (1996).

Conselice, C. J., "The Relationship between Stellar Light Distributions of Galaxies and Their Formation Histories", ApJL 147, 1, 1–28 (2003).

Conselice, C. J., "The Evolution of Galaxy Structure Over Cosmic Time", araa 52, 291–337 (2014).

Conselice, C. J., M. A. Bershady and A. Jangren, "The Asymmetry of Galaxies: Physical Morphology for Nearby and High-Redshift Galaxies", ApJ 529, 2, 886–910 (2000).

Cowie, L. L., A. Songaila, E. M. Hu and J. G. Cohen, "New Insight on Galaxy Formation and Evolution From Keck Spectroscopy of the Hawaii Deep Fields", AJ 112, 839 (1996).

Curtis-Lake, E., R. J. McLure, J. S. Dunlop, A. B. Rogers, T. Targett, A. Dekel, R. S. Ellis, S. M. Faber, H. C. Ferguson, N. A. Grogin, D. D. Kocevski, A. M. Koekemoer, K. Lai, E. Mármol-Queraltó and B. E. Robertson, "Non-parametric analysis of the rest-frame UV sizes and morphological disturbance amongst L_* galaxies at 4 < z < 8", MNRAS 457, 1, 440–464 (2016).

Davis, A. J. and P. Natarajan, "Angular momentum and clustering properties of early dark matter haloes", MNRAS 393, 4, 1498–1502 (2009).

de Barros, S., E. Vanzella, R. Amorín, M. Castellano, B. Siana, A. Grazian, H. Suh, I. Balestra, C. Vignali, A. Verhamme, G. Zamorani, M. Mignoli, G. Hasinger, A. Comastri, L. Pentericci, E. Pérez-Montero, A. Fontana, M. Giavalisco and R. Gilli, "An extreme [O III] emitter at z = 3.2: a low metallicity Lyman continuum source", A&A 585, A51 (2016).

de Jong, R. S. and C. Lacey, "The Local Space Density of SB-SDM Galaxies as Function of Their Scale Size, Surface Brightness, and Luminosity", ApJ 545, 2, 781–797 (2000).

De Lucia, G., V. Springel, S. D. M. White, D. Croton and G. Kauffmann, "The formation history of elliptical galaxies", MNRAS 366, 2, 499–509 (2006).

Dekel, A. and A. Burkert, "Wet disc contraction to galactic blue nuggets and quenching to red nuggets", MNRAS 438, 2, 1870–1879 (2014).

Dekel, A., R. Sari and D. Ceverino, "Formation of Massive Galaxies at High Redshift: Cold Streams, Clumpy Disks, and Compact Spheroids", ApJ 703, 1, 785–801 (2009).

Dey, A., H. Spinrad, D. Stern, J. R. Graham and F. H. Chaffee, "A Galaxy at z = 5.34", ApJL 498, 2, L93–L97 (1998).

Dow-Hygelund, C. C., B. P. Holden, R. J. Bouwens, G. D. Illingworth, A. van der Wel, M. Franx, P. G. van Dokkum, H. Ford, P. Rosati, D. Magee and A. Zirm, "Spectroscopy of z ~6 i-Dropout Galaxies: Frequency of Lyα Emission and the Sizes of Lyα-emitting Galaxies1,", ApJ 660, 1, 47–61 (2007).

Dressler, A., "Galaxy morphology in rich clusters: implications for the formation and evolution of galaxies.", ApJ 236, 351–365 (1980).

Driver, S. P., P. D. Allen, A. W. Graham, E. Cameron, J. Liske, S. C. Ellis, N. J. G. Cross, R. De Propris, S. Phillipps and W. J. Couch, "The Millennium Galaxy Catalogue: morphological classification and bimodality in the colour-concentration plane", MNRAS 368, 1, 414–434 (2006).

Eales, S., P. de Vis, M. W. L. Smith, K. Appah, L. Ciesla, C. Duffield and S. Schofield, "The Galaxy End Sequence", MNRAS 465, 3, 3125–3133 (2017).

Fall, S. M. and G. Efstathiou, "Formation and rotation of disc galaxies with haloes.", MNRAS 193, 189–206 (1980).

Fang, J. J., S. M. Faber, D. C. Koo and A. Dekel, "A Link between Star Formation Quenching and Inner Stellar Mass Density in Sloan Digital Sky Survey Central Galaxies", ApJ 776, 1, 63 (2013).

Ferreras, I., T. Lisker, C. M. Carollo, S. J. Lilly and B. Mobasher, "Evolution of Field Early-Type Galaxies: The View from GOODS CDFS", ApJ 635, 1, 243–259 (2005).

Ferreras, I., T. Lisker, A. Pasquali and S. Kaviraj, "Exploring the formation of spheroidal galaxies out to z ~1.5 in GOODS", MNRAS 395, 1, 554–566 (2009).

Finkelstein, K. D., S. L. Finkelstein, V. Tilvi, S. Malhotra, J. E. Rhoads, N. A. Grogin, N. Pirzkal, A. Dey, B. T. Jannuzi, B. Mobasher, S. Pakzad, B. Salmon and J. Wang, "Probing the Physical Properties of z = 4.5 Lyman Alpha Emitters with Spitzer", ApJ 813, 1, 78 (2015).

Fisher, D. B. and N. Drory, "Bulges of Nearby Galaxies with Spitzer: Scaling Relations in Pseudobulges and Classical Bulges", ApJ 716, 2, 942–969 (2010).

Fitzpatrick, E. L., "Correcting for the Effects of Interstellar Extinction", PASP 111, 755, 63–75 (1999).

Fitzpatrick, E. L. and D. Massa, "An Analysis of the Shapes of Ultraviolet Extinction Curves. III. an Atlas of Ultraviolet Extinction Curves", APJS 72, 163 (1990).

Fontana, A., S. D'Odorico, F. Poli, E. Giallongo, S. Arnouts, S. Cristiani, A. Moorwood and P. Saracco, "Photometric Redshifts and Selection of High-Redshift Galaxies in the NTT and Hubble Deep Fields", AJ 120, 5, 2206–2219 (2000).

Franx, M., P. G. van Dokkum, N. M. Förster Schreiber, S. Wuyts, I. Labbé and S. Toft, "Structure and Star Formation in Galaxies out to z = 3: Evidence for Surface Density Dependent Evolution and Upsizing", ApJ 688, 2, 770–788 (2008).

Gadotti, D. A., "Structural properties of pseudo-bulges, classical bulges and elliptical galaxies: a Sloan Digital Sky Survey perspective", MNRAS 393, 4, 1531–1552 (2009).

Gawiser, E., H. Francke, K. Lai, K. Schawinski, C. Gronwall, R. Ciardullo, R. Quadri, A. Orsi, L. F. Barrientos, G. A. Blanc, G. Fazio, J. J. Feldmeier, J.-s. Huang, L. Infante, P. Lira, N. Padilla, E. N. Taylor, E. Treister, C. M. Urry, P. G. van Dokkum and S. N. Virani, "Lyα-Emitting Galaxies at z = 3.1: L* Progenitors Experiencing Rapid Star Formation", ApJ 671, 1, 278–284 (2007).

Gazagnes, S., J. Chisholm, D. Schaerer, A. Verhamme and Y. Izotov, "The origin of the escape of Lyman alpha and ionizing photons in Lyman Continuum Emitters", arXiv e-prints p. arXiv:2005.07215 (2020).

Genzel, R., N. M. Förster Schreiber, P. Lang, S. Tacchella, L. J. Tacconi, S. Wuyts, K. Bandara, A. Burkert, P. Buschkamp, C. M. Carollo, G. Cresci, R. Davies, F. Eisenhauer, E. K. S. Hicks, J. Kurk, S. J. Lilly, D. Lutz, C. Mancini, T. Naab, S. Newman, Y. Peng, A. Renzini, K. Shapiro Griffin, A. Sternberg, D. Vergani, E. Wisnioski, E. Wuyts and G. Zamorani, "The SINS/zC-SINF Survey of z ~2 Galaxy Kinematics: Evidence for Gravitational Quenching", ApJ 785, 1, 75 (2014).

Giallongo, E., S. D'Odorico, A. Fontana, S. Cristiani, E. Egami, E. Hu and R. G. McMahon, "The Photometric Redshift Distribution and Evolutionary Properties of Galaxies up to Z ~4.5 in the Field of the Quasar BR 1202-0725", AJ 115, 6, 2169–2183 (1998).

Giavalisco, M., H. C. Ferguson, A. M. Koekemoer, M. Dickinson, D. M. Alexander, F. E. Bauer, J. Bergeron, C. Biagetti, W. N. Brandt, S. Casertano, C. Cesarsky, E. Chatzichristou, C. Conselice, S. Cristiani, L. Da Costa, T. Dahlen, D. de Mello, P. Eisenhardt, T. Erben, S. M. Fall, C. Fassnacht, R. Fosbury, A. Fruchter, J. P. Gardner, N. Grogin, R. N. Hook, A. E. Hornschemeier, R. Idzi, S. Jogee, C. Kretchmer, V. Laidler, K. S. Lee, M. Livio, R. Lucas, P. Madau, B. Mobasher, L. A. Moustakas, M. Nonino, P. Padovani, C. Papovich, Y. Park, S. Ravindranath, A. Renzini, M. Richardson, A. Riess, P. Rosati, M. Schirmer, E. Schreier, R. S. Somerville, H. Spinrad, D. Stern, M. Stiavelli, L. Strolger, C. M. Urry, B. Vandame, R. Williams and C. Wolf, "The Great Observatories Origins Deep Survey: Initial Results from Optical and Near-Infrared Imaging", ApJL 600, 2, L93–L98 (2004).

Grazian, A., M. Castellano, A. Fontana, L. Pentericci, J. S. Dunlop, R. J. McLure, A. M. Koekemoer, M. E. Dickinson, S. M. Faber, H. C. Ferguson, A. Galametz, M. Giavalisco, N. A. Grogin, N. P. Hathi, D. D. Kocevski, K. Lai, J. A. Newman and E. Vanzella, "The size-luminosity relation at z = 7 in CANDELS and its implication on reionization", A&A 547, A51 (2012).

Grogin, N. A., D. D. Kocevski, S. M. Faber, H. C. Ferguson, A. M. Koekemoer, A. G. Riess, V. Acquaviva, D. M. Alexander, O. Almaini, M. L. N. Ashby, M. Barden, E. F. Bell, F. Bournaud, T. M. Brown, K. I. Caputi, S. Casertano, P. Cassata, M. Castellano, P. Challis, R.-R. Chary, E. Cheung, M. Cirasuolo, C. J. Conselice, A. Roshan Cooray, D. J. Croton, E. Daddi, T. Dahlen, R. Davé, D. F. de Mello, A. Dekel, M. Dickinson, T. Dolch, J. L. Donley, J. S. Dunlop, A. A. Dutton, D. Elbaz, G. G. Fazio, A. V. Filippenko, S. L. Finkelstein, A. Fontana, J. P. Gardner, P. M. Garnavich, E. Gawiser, M. Giavalisco, A. Grazian, Y. Guo, N. P. Hathi,

B. Häussler, P. F. Hopkins, J.-S. Huang, K.-H. Huang, S. W. Jha, J. S. Kartaltepe, R. P. Kirshner, D. C. Koo, K. Lai, K.-S. Lee, W. Li, J. M. Lotz, R. A. Lucas, P. Madau, P. J. McCarthy, E. J. McGrath, D. H. McIntosh, R. J. McLure, B. Mobasher, L. A. Moustakas, M. Mozena, K. Nandra, J. A. Newman, S.-M. Niemi, K. G. Noeske, C. J. Papovich, L. Pentericci, A. Pope, J. R. Primack, A. Rajan, S. Ravindranath, N. A. Reddy, A. Renzini, H.-W. Rix, A. R. Robaina, S. A. Rodney, D. J. Rosario, P. Rosati, S. Salimbeni, C. Scarlata, B. Siana, L. Simard, J. Smidt, R. S. Somerville, H. Spinrad, A. N. Straughn, L.-G. Strolger, O. Telford, H. I. Teplitz, J. R. Trump, A. van der Wel, C. Villforth, R. H. Wechsler, B. J. Weiner, T. Wiklind, V. Wild, G. Wilson, S. Wuyts, H.-J. Yan and M. S. Yun, "CANDELS: The Cosmic Assembly Near-infrared Deep Extragalactic Legacy Survey", ApJL 197, 2, 35 (2011).

Gronke, M. and M. Dijkstra, "Lyman-α Spectra from Multiphase Outflows, and their Connection to Shell Models", ApJ 826, 1, 14 (2016).

Gu, Y., G. Fang, Q. Yuan, Z. Cai and T. Wang, "The Morphological Evolution, AGN Fractions, Dust Content, Environments, and Downsizing of Massive Green Valley Galaxies at 0.5 < z < 2.5 in 3D-HST/CANDELS", ApJ 855, 1, 10 (2018).

Guaita, L., J. Melinder, M. Hayes, G. Östlin, J. E. Gonzalez, G. Micheva, A. Adamo, J. M. Mas-Hesse, A. Sandberg, H. Otí-Floranes, D. Schaerer, A. Verhamme, E. Freeland, I. Orlitová, P. Laursen, J. M. Cannon, F. Duval, T. Rivera-Thorsen, E. C. Herenz, D. Kunth, H. Atek, J. Puschnig, P. Gruyters and S. A. Pardy, "The Lyman alpha reference sample. IV. Morphology at low and high redshift", A&A 576, A51 (2015).

Guo, Y., H. C. Ferguson, M. Giavalisco, G. Barro, S. P. Willner, M. L. N. Ashby, T. Dahlen, J. L. Donley, S. M. Faber, A. Fontana, A. Galametz, A. Grazian, K.-H. Huang, D. D. Kocevski, A. M. Koekemoer, D. C. Koo, E. J. McGrath, M. Peth, M. Salvato, S. Wuyts, M. Castellano, A. R. Cooray, M. E. Dickinson, J. S. Dunlop, G. G. Fazio, J. P. Gardner, E. Gawiser, N. A. Grogin, N. P. Hathi, L.-T. Hsu, K.-S. Lee, R. A. Lucas, B. Mobasher, K. Nand ra, J. A. Newman and A. van der Wel, "CANDELS Multi-wavelength Catalogs: Source Detection and Photometry in the GOODS-South Field", ApJL 207, 2, 24 (2013).

Haines, C. P., A. Iovino, J. Krywult, L. Guzzo, I. Davidzon, M. Bolzonella, B. Garilli, M. Scodeggio, B. R. Granett, S. de la Torre, G. De Lucia, U. Abbas, C. Adami, S. Arnouts, D. Bottini, A. Cappi, O. Cucciati, P. Franzetti, A. Fritz, A. Gargiulo, V. Le Brun, O. Le Fèvre, D. Maccagni, K. Małek, F. Marulli, T. Moutard, M. Polletta, A. Pollo, L. A. M. Tasca, R. Tojeiro, D. Vergani, A. Zanichelli, G. Zamorani, J. Bel, E. Branchini, J. Coupon, O. Ilbert, L. Moscardini, J. A. Peacock and M. Siudek, "The VIMOS Public Extragalactic Redshift Survey (VIPERS). Downsizing of the blue cloud and the influence of galaxy size on mass quenching over the last eight billion years", A&A 605, A4 (2017).

Hamilton, D., "The spectral evolution of galaxies. I. an observational approach.", ApJ 297, 371–389 (1985).

Hathi, N. P., I. Ferreras, A. Pasquali, S. Malhotra, J. E. Rhoads, N. Pirzkal, R. A. Windhorst and C. Xu, "Stellar Populations of Late-Type Bulges at z 1 in the Hubble Ultra Deep Field", ApJ 690, 2, 1866–1882 (2009).

Hathi, N. P., S. Malhotra and J. E. Rhoads, "Starburst Intensity Limit of Galaxies at z simeq 5-6", ApJ 673, 2, 686–693 (2008).

Heckman, T. M., "Galactic Superwinds at Low and High Redshift", in "Gas and Galaxy Evolution", edited by J. E. Hibbard, M. Rupen and J. H. van Gorkom, vol. 240 of *Astronomical Society of the Pacific Conference Series*, p. 345 (2001).

Heckman, T. M., "Galactic Superwinds Circa 2001", in "Extragalactic Gas at Low Redshift", edited by J. S. Mulchaey and J. T. Stocke, vol. 254 of *Astronomical Society of the Pacific Conference Series*, p. 292 (2002).

Heckman, T. M., R. M. Alexandroff, S. Borthakur, R. Overzier and C. Leitherer, "The Systematic Properties of the Warm Phase of Starburst-Driven Galactic Winds", ApJ 809, 2, 147 (2015).

Heckman, T. M. and S. Borthakur, "The Implications of Extreme Outflows from Extreme Starbursts", ApJ 822, 1, 9 (2016).

Heckman, T. M., C. G. Hoopes, M. Seibert, D. C. Martin, S. Salim, R. M. Rich, G. Kauffmann, S. Charlot, T. A. Barlow, L. Bianchi, Y.-I. Byun, J. Donas, K. Forster, P. G. Friedman, P. N. Jelinsky, Y.-W. Lee, B. F. Madore, R. F. Malina, B. Milliard, P. F. Morrissey, S. G. Neff, D. Schiminovich, O. H. W. Siegmund, T. Small, A. S. Szalay, B. Y. Welsh and T. K. Wyder, "The Properties of Ultraviolet-luminous Galaxies at the Current Epoch", ApJL 619, 1, L35–L38 (2005).

Henry, A., C. Scarlata, C. L. Martin and D. Erb, "Lyα Emission from Green Peas: The Role of Circumgalactic Gas Density, Covering, and Kinematics", ApJ 809, 1, 19 (2015).

Hernán-Caballero, A., A. Alonso-Herrero, P. G. Pérez-González, N. Cardiel, A. Cava, I. Ferreras, G. Barro, L. Tresse, E. Daddi, J. Cenarro, C. J. Conselice, R. Guzmán and J. Gallego, "SHARDS: stellar populations and star formation histories of a mass-selected sample of 0.65 < z < 1.1 galaxies", MNRAS 434, 3, 2136–2152 (2013).

Hopkins, P. F., K. Bundy, L. Hernquist and R. S. Ellis, "Observational Evidence for the Coevolution of Galaxy Mergers, Quasars, and the Blue/Red Galaxy Transition", ApJ 659, 2, 976–996 (2007).

Huang, K.-H., H. C. Ferguson, S. Ravindranath and J. Su, "The Bivariate Size-Luminosity Relations for Lyman Break Galaxies at z ~4-5", ApJ 765, 1, 68 (2013).

Hubble, E. P., "Extragalactic nebulae.", ApJ 64, 321–369 (1926).

Hubble, E. P., *Realm of the Nebulae* (1936).

Huertas-Company, M., M. Bernardi, P. G. Pérez-González, M. L. N. Ashby, G. Barro, C. Conselice, E. Daddi, A. Dekel, P. Dimauro, S. M. Faber, N. A. Grogin, J. S. Kartaltepe, D. D. Kocevski, A. M. Koekemoer, D. C. Koo, S. Mei and F. Shankar, "Mass assembly and morphological transformations since z $\sim$ 3 from CANDELS", MNRAS 462, 4, 4495–4516 (2016).

Huertas-Company, M., P. G. Pérez-González, S. Mei, F. Shankar, M. Bernardi, E. Daddi, G. Barro, G. Cabrera-Vives, A. Cattaneo, P. Dimauro and R. Gravet, "The Morphologies of Massive Galaxies from z ~3—Witnessing the Two Channels of Bulge Growth", ApJ 809, 1, 95 (2015).

Ilbert, O., M. Salvato, E. Le Floc'h, H. Aussel, P. Capak, H. J. McCracken, B. Mobasher, J. Kartaltepe, N. Scoville, D. B. Sanders, S. Arnouts, K. Bundy, P. Cassata, J. P. Kneib, A. Koekemoer, O. Le Fèvre, S. Lilly, J. Surace, Y. Taniguchi, L. Tasca, D. Thompson, L. Tresse, M. Zamojski, G. Zamorani and E. Zucca, "Galaxy Stellar Mass Assembly Between 0.2 < z < 2 from the S-COSMOS Survey", ApJ 709, 2, 644–663 (2010).

Izotov, Y. I., N. G. Guseva and T. X. Thuan, "Green Pea Galaxies and Cohorts: Luminous Compact Emission-line Galaxies in the Sloan Digital Sky Survey", ApJ 728, 2, 161 (2011).

Izotov, Y. I., D. Schaerer, T. X. Thuan, G. Worseck, N. G. Guseva, I. Orlitová and A. Verhamme, "Detection of high Lyman continuum leakage from four low-redshift compact star-forming galaxies", MNRAS 461, 4, 3683–3701 (2016).

Izotov, Y. I., D. Schaerer, G. Worseck, N. G. Guseva, T. X. Thuan, A. Verhamme, I. Orlitová and K. J. Fricke, "J1154+2443: a low-redshift compact star-forming galaxy with a 46 per cent leakage of Lyman continuum photons", MNRAS 474, 4, 4514–4527 (2018a).

Izotov, Y. I., D. Schaerer, G. Worseck, N. G. Guseva, T. X. Thuan, A. Verhamme, I. Orlitová and K. J. Fricke, "J1154+2443: a low-redshift compact star-forming galaxy with a 46 per cent leakage of Lyman continuum photons", MNRAS 474, 4, 4514–4527 (2018b).

Izotov, Y. I., G. Worseck, D. Schaerer, N. G. Guseva, T. X. Thuan, A. Fricke, Verhamme and I. Orlitová, "Low-redshift Lyman continuum leaking galaxies with high [O III]/[O II] ratios", MNRAS 478, 4, 4851–4865 (2018c).

Jaskot, A. E., T. Dowd, M. S. Oey, C. Scarlata and J. McKinney, "New Insights on Lyα and Lyman Continuum Radiative Transfer in the Greenest Peas", ApJ 885, 1, 96 (2019).

Jaskot, A. E. and M. S. Oey, "The Origin and Optical Depth of Ionizing Radiation in the "Green Pea" Galaxies", ApJ 766, 2, 91 (2013).

Jiang, L., E. Egami, X. Fan, R. A. Windhorst, S. H. Cohen, R. Davé, K. Finlator, N. Kashikawa, M. Mechtley, M. Ouchi and K. Shimasaku, "Physical Properties of Spectroscopically Confirmed Galaxies at z >= 6. II. Morphology of the Rest-frame UV Continuum and Lyα Emission", ApJ 773, 2, 153 (2013).

Jiang, T., S. Malhotra, J. E. Rhoads and H. Yang, "Direct T $_e$ Metallicity Calibration of R23 in Strong Line Emitters", ApJ 872, 2, 145 (2019a).

Jiang, T., S. Malhotra, H. Yang and J. E. Rhoads, "Correlation between SFR Surface Density and Thermal Pressure of Ionized Gas in Local Analogs of High-redshift Galaxies", ApJ 872, 2, 146 (2019b).

Jiang, T., S. Malhotra, H. Yang and J. E. Rhoads, "Correlation between SFR Surface Density and Thermal Pressure of Ionized Gas in Local Analogs of High-redshift Galaxies", ApJ 872, 2, 146 (2019c).

Jung, I., S. L. Finkelstein, M. Song, M. Dickinson, A. Dekel, H. C. Ferguson, A. Fontana, A. M. Koekemoer, Y. Lu, B. Mobasher, C. Papovich, J. Ryan, Russell E., B. Salmon and A. N. Straughn, "Evidence for Reduced Specific Star Formation Rates in the Centers of Massive Galaxies at z = 4", ApJ 834, 1, 81 (2017).

Kartaltepe, J. S., M. Mozena, D. Kocevski, D. H. McIntosh, J. Lotz, E. F. Bell, S. Faber, H. Ferguson, D. Koo, R. Bassett, M. Bernyk, K. Blancato, F. Bournaud, P. Cassata, M. Castellano, E. Cheung, C. J. Conselice, D. Croton, T. Dahlen, D. F. de Mello, L. DeGroot, J. Donley, J. Guedes, N. Grogin, N. Hathi, M. Hilton, B. Hollon, A. Koekemoer, N. Liu, R. A. Lucas, M. Martig, E. McGrath, C. McPartland, B. Mobasher, A. Morlock, E. O'Leary, M. Peth, J. Pforr, A. Pillepich, D. Rosario, E. Soto, A. Straughn, O. Telford, B. Sunnquist, J. Trump, B. Weiner, S. Wuyts, H. Inami, S. Kassin, C. Lani, G. B. Poole and Z. Rizer, "CANDELS Visual Classifications: Scheme, Data Release, and First Results", ApJL 221, 1, 11 (2015).

Kauffmann, G., T. M. Heckman, S. D. M. White, S. Charlot, C. Tremonti, J. Brinchmann, G. Bruzual, E. W. Peng, M. Seibert, M. Bernardi, M. Blanton, J. Brinkmann, F. Castander, I. Csábai, M. Fukugita, Z. Ivezic, J. A. Munn, R. C. Nichol, N. Padmanabhan, A. R. Thakar, D. H. Weinberg and D. York, "Stellar masses and star formation histories for 10^5 galaxies from the Sloan Digital Sky Survey", MNRAS 341, 1, 33–53 (2003a).

Kauffmann, G., T. M. Heckman, S. D. M. White, S. Charlot, C. Tremonti, E. W. Peng, M. Seibert, J. Brinkmann, R. C. Nichol, M. SubbaRao and D. York, "The dependence of star formation history and internal structure on stellar mass for 10^5 low-redshift galaxies", MNRAS 341, 1, 54–69 (2003b).

Kennicutt, J., Robert C., "The Global Schmidt Law in Star-forming Galaxies", ApJ 498, 2, 541–552 (1998).

Khim, H.-g., J. Park, S.-W. Seo, J. Lee, R. Smith and S. K. Yi, "Demographics of Isolated Galaxies along the Hubble Sequence", ApJL 220, 1, 3 (2015).

Kim, K., S. Malhotra, J. E. Rhoads, N. R. Butler and H. Yang, "The Importance of Star Formation Intensity in Lyα Escape from Green Pea Galaxies and Lyman Break Galaxy Analogs", ApJ 893, 2, 134 (2020).

Kim, K., S. Malhotra, J. E. Rhoads, B. Joshi, I. Fererras and A. Pasquali, "Galaxy Structure, Stellar Populations, and Star Formation Quenching at $0.6 \lesssim z \lesssim 1.2$", ApJ 867, 2, 118 (2018).

Kim, K., S. Oh, H. Jeong, A. Aragón-Salamanca, R. Smith and S. K. Yi, "The Demographics of Galactic Bulges in the SDSS Database", APJS 225, 1, 6 (2016).

Koekemoer, A. M., S. M. Faber, H. C. Ferguson, N. A. Grogin, D. D. Kocevski, D. C. Koo, K. Lai, J. M. Lotz, R. A. Lucas, E. J. McGrath, S. Ogaz, A. Rajan, A. G. Riess, S. A. Rodney, L. Strolger, S. Casertano, M. Castellano, T. Dahlen, M. Dickinson, T. Dolch, A. Fontana, M. Giavalisco, A. Grazian, Y. Guo, N. P. Hathi, K.-H. Huang, A. van der Wel, H.-J. Yan, V. Acquaviva, D. M. Alexander, O. Almaini, M. L. N. Ashby, M. Barden, E. F. Bell, F. Bournaud, T. M. Brown, K. I. Caputi, P. Cassata, P. J. Challis, R.-R. Chary, E. Cheung, M. Cirasuolo, C. J. Conselice, A. Roshan Cooray, D. J. Croton, E. Daddi, R. Davé, D. F. de Mello, L. de Ravel, A. Dekel, J. L. Donley, J. S. Dunlop, A. A. Dutton, D. Elbaz, G. G. Fazio, A. V. Filippenko, S. L. Finkelstein, C. Frazer, J. P. Gardner, P. M. Garnavich, E. Gawiser, R. Gruetzbauch, W. G. Hartley, B. Häussler, J. Herrington, P. F. Hopkins, J.-S. Huang, S. W. Jha, A. Johnson, J. S. Kartaltepe, A. A. Khostovan, R. P. Kirshner, C. Lani, K.-S. Lee, W. Li, P. Madau, P. J. McCarthy, D. H. McIntosh, R. J. McLure, C. McPartland, B. Mobasher, H. Moreira, A. Mortlock, L. A. Moustakas, M. Mozena, K. Nandra, J. A. Newman, J. L. Nielsen, S. Niemi, K. G. Noeske, C. J. Papovich, L. Pentericci, A. Pope, J. R. Primack, S. Ravindranath, N. A. Reddy, A. Renzini, H.-W. Rix, A. R. Robaina, D. J. Rosario, P. Rosati, S. Salimbeni, C. Scarlata, B. Siana, L. Simard, J. Smidt, D. Snyder, R. S. Somerville, H. Spinrad, A. N. Straughn, O. Telford, H. I. Teplitz, J. R. Trump, C. Vargas, C. Villforth, C. R. Wagner, P. Wand ro, R. H. Wechsler, B. J. Weiner, T. Wiklind, V. Wild, G. Wilson, S. Wuyts and M. S. Yun, "CANDELS: The Cosmic Assembly Near-infrared Deep Extragalactic Legacy Survey—The Hubble Space Telescope Observations, Imaging Data Products, and Mosaics", ApJL 197, 2, 36 (2011).

Kolaczyk, E. D., "Nonparametric Estimation of Gamma-Ray Burst Intensities Using Haar Wavelets", ApJ 483, 1, 340–349 (1997).

Kormendy, J., "Brightness distributions in compact and normal galaxies. II. Structure parameters of the spheroidal component.", ApJ 218, 333–346 (1977).

Kümmel, M., J. R. Walsh, N. Pirzkal, H. Kuntschner and A. Pasquali, "The Slitless Spectroscopy Data Extraction Software aXe", PASP 121, 875, 59 (2009).

La Barbera, F., G. Busarello, P. Merluzzi, M. Massarotti and M. Capaccioli, "On the Invariant Distribution of Galaxies in the r_e-<μ>$_e$ Plane out to z=0.64", ApJ 595, 1, 127–136 (2003).

Lang, P., S. Wuyts, R. S. Somerville, N. M. Förster Schreiber, R. Genzel, E. F. Bell, G. Brammer, A. Dekel, S. r. M. Faber, H. C. Ferguson, N. A. Grogin, D. D. Kocevski, A. M. Koekemoer, D. Lutz, E. J. McGrath, I. Momcheva, E. J. Nelson, J. R. Primack, D. J. Rosario, R. E. Skelton, L. J. Tacconi, P. G. van Dokkum and K. E. Whitaker, "Bulge Growth and Quenching since z = 2.5 in CANDELS/3D-HST", ApJ 788, 1, 11 (2014).

Law, D. R., C. C. Steidel, D. K. Erb, M. Pettini, N. A. Reddy, A. E. Shapley, K. L. Adelberger and D. J. Simenc, "The Physical Nature of Rest-UV Galaxy Morphology during the Peak Epoch of Galaxy Formation", ApJ 656, 1, 1–26 (2007).

Lee, B., M. Giavalisco, K. Whitaker, C. C. Williams, H. C. Ferguson, V. Acquaviva, A. M. Koekemoer, A. N. Straughn, Y. Guo, J. S. Kartaltepe, J. Lotz, C. Pacifici, D. J. Croton, R. S. Somerville and Y. Lu, "The Intrinsic Characteristics of Galaxies on the SFR-M $_*$ Plane at 1.2 < z < 4: I. The Correlation between Stellar Age, Central Density, and Position Relative to the Main Sequence", ApJ 853, 2, 131 (2018).

Lee, J. C., A. Gil de Paz, C. Tremonti, J. Kennicutt, Robert C., S. Salim, M. Bothwell, D. Calzetti, J. Dalcanton, D. Dale, C. Engelbracht, S. J. J. G. Funes, B. Johnson, S. Sakai, E. Skillman, L. van Zee, F. Walter and D. Weisz, "Comparison of Hα and UV Star Formation Rates in the Local Volume: Systematic Discrepancies for Dwarf Galaxies", ApJ 706, 1, 599–613 (2009).

Lilly, S. J. and C. M. Carollo, "Surface Density Effects in Quenching: Cause or Effect?", ApJ 833, 1, 1 (2016).

Lintott, C. J., K. Schawinski, A. Slosar, K. Land, S. Bamford, D. Thomas, M. J. Raddick, R. C. Nichol, A. Szalay, D. Andreescu, P. Murray and J. Vandenberg, "Galaxy Zoo: morphologies derived from visual inspection of galaxies from the Sloan Digital Sky Survey", MNRAS 389, 3, 1179–1189 (2008).

Liu, C., S. J. Mutch, G. B. Poole, P. W. Angel, A. R. Duffy, P. M. Geil, A. Mesinger and J. S. B. Wyithe, "Dark-ages reionization and galaxy-formation simulation - VII. The sizes of high-redshift galaxies", MNRAS 465, 3, 3134–3142 (2017).

Longhetti, M., P. Saracco, P. Severgnini, R. Della Ceca, F. Mannucci, R. Bender, N. Drory, G. Feulner and U. Hopp, "The Kormendy relation of massive elliptical galaxies at z ~1.5: evidence for size evolution", MNRAS 374, 2, 614–626 (2007).

Lopes, P. A. A., S. B. Rembold, A. L. B. Ribeiro, R. S. Nascimento and B. Vajgel, "NoSOCS in SDSS - V. Red disc and blue bulge galaxies across different environments", MNRAS 461, 3, 2559–2579 (2016).

Lotz, J. M., J. Primack and P. Madau, "A New Nonparametric Approach to Galaxy Morphological Classification", AJ 128, 1, 163–182 (2004).

Malhotra, S. and J. E. Rhoads, "Large Equivalent Width Lyα line Emission at z=4.5: Young Galaxies in a Young Universe?", ApJL 565, 2, L71–L74 (2002).

Malhotra, S., J. E. Rhoads, S. L. Finkelstein, N. Hathi, K. Nilsson, E. McLinden and N. Pirzkal, "Sizing up Lyα and Lyman Break Galaxies", ApJL 750, 2, L36 (2012).

Marchi, F., L. Pentericci, L. Guaita, M. Talia, M. Castellano, N. Hathi, D. Schaerer, R. Amorin, M. Bolzonella, A. C. Carnall, S. Charlot, J. Chevallard, F. Cullen, S. L. Finkelstein, A. Fontana, F. Fontanot, B. Garilli, P. Hibon, A. M. Koekemoer,

D. Maccagni, R. J. McLure, C. Papovich, L. Pozzetti and A. Saxena, "The VANDELS survey: the role of ISM and galaxy physical properties in the escape of Lyα emission in z $\sim$ 3.5 star-forming galaxies", A&A 631, A19 (2019).

Margalef-Bentabol, B., C. J. Conselice, A. Mortlock, W. Hartley, K. Duncan, H. C. Ferguson, A. Dekel and J. R. Primack, "The formation of bulges, discs and two-component galaxies in the CANDELS Survey at z < 3", MNRAS 461, 3, 2728–2746 (2016).

Margalef-Bentabol, B., C. J. Conselice, A. Mortlock, W. Hartley, K. Duncan, R. Kennedy, D. D. Kocevski and G. Hasinger, "Stellar populations, stellar masses and the formation of galaxy bulges and discs at z < 3 in CANDELS", MNRAS 473, 4, 5370–5384 (2018).

Martig, M., F. Bournaud, R. Teyssier and A. Dekel, "Morphological Quenching of Star Formation: Making Early-Type Galaxies Red", ApJ 707, 1, 250–267 (2009).

Martig, M., A. F. Crocker, F. Bournaud, E. Emsellem, J. M. Gabor, K. Alatalo, L. Blitz, M. Bois, M. Bureau, M. Cappellari, R. L. Davies, T. A. Davis, A. Dekel, P. T. de Zeeuw, P.-A. Duc, J. Falcón-Barroso, S. Khochfar, D. Krajnović, H. Kuntschner, R. Morganti, R. M. McDermid, T. Naab, T. Oosterloo, M. Sarzi, N. Scott, P. Serra, K. S. Griffin, R. Teyssier, A.-M. Weijmans and L. M. Young, "The ATLAS^{3D} project - XXII. Low-efficiency star formation in early-type galaxies: hydrodynamic models and observations", MNRAS 432, 3, 1914–1927 (2013).

McGrath, E. J., A. Stockton, G. Canalizo, M. Iye and T. Maihara, "Morphologies and Color Gradients of Luminous Evolved Galaxies at z ˜1.5", ApJ 682, 1, 303–318 (2008).

Meert, A., V. Vikram and M. Bernardi, "A catalogue of 2D photometric decompositions in the SDSS-DR7 spectroscopic main galaxy sample: preferred models and systematics", MNRAS 446, 4, 3943–3974 (2015).

Meurer, G. R., T. M. Heckman, M. D. Lehnert, C. Leitherer and J. Lowenthal, "The Panchromatic Starburst Intensity Limit at Low and High Redshift", AJ 114, 54–68 (1997).

Mo, H. J., S. Mao and S. D. M. White, "The formation of galactic discs", MNRAS 295, 2, 319–336 (1998).

Muzzin, A., D. Marchesini, M. Stefanon, M. Franx, H. J. McCracken, B. Milvang-Jensen, J. S. Dunlop, J. P. U. Fynbo, G. Brammer, I. Labbé and P. G. van Dokkum, "The Evolution of the Stellar Mass Functions of Star-forming and Quiescent Galaxies to z = 4 from the COSMOS/UltraVISTA Survey", ApJ 777, 1, 18 (2013).

Neufeld, D. A., "The Escape of Lyman-Alpha Radiation from a Multiphase Interstellar Medium", ApJL 370, L85 (1991).

Noeske, K. G., B. J. Weiner, S. M. Faber, C. Papovich, D. C. Koo, R. S. Somerville, K. Bundy, C. J. Conselice, J. A. Newman, D. Schiminovich, E. Le Floc'h, A. L. Coil, G. H. Rieke, J. M. Lotz, J. R. Primack, P. Barmby, M. C. Cooper, M. Davis, R. S. Ellis, G. G. Fazio, P. Guhathakurta, J. Huang, S. A. Kassin, D. C. Martin, A. C. Phillips, R. M. Rich, T. A. Small, C. N. A. Willmer and G. Wilson, "Star Formation in AEGIS Field Galaxies since z=1.1: The Dominance of Gradually Declining Star Formation, and the Main Sequence of Star-forming Galaxies", ApJL 660, 1, L43–L46 (2007).

Noguchi, M., "Early Evolution of Disk Galaxies: Formation of Bulges in Clumpy Young Galactic Disks", ApJ 514, 1, 77–95 (1999).

Oesch, P. A., R. J. Bouwens, C. M. Carollo, G. D. Illingworth, M. Trenti, M. Stiavelli, D. Magee, I. Labbé and M. Franx, "Structure and Morphologies of z ~7-8 Galaxies from Ultra-deep WFC3/IR Imaging of the Hubble Ultra-deep Field", ApJL 709, 1, L21–L25 (2010).

Oh, K., H. Choi, H.-G. Kim, J.-S. Moon and S. K. Yi, "Demographics of Sloan Digital Sky Survey Galaxies along the Hubble Sequence", AJ 146, 6, 151 (2013).

Oke, J. B. and J. E. Gunn, "Secondary standard stars for absolute spectrophotometry.", ApJ 266, 713–717 (1983).

Omand, C. M. B., M. L. Balogh and B. M. Poggianti, "The connection between galaxy structure and quenching efficiency", MNRAS 440, 1, 843–858 (2014).

Ono, Y., M. Ouchi, E. Curtis-Lake, M. A. Schenker, R. S. Ellis, R. J. McLure, J. S. Dunlop, B. E. Robertson, A. M. Koekemoer, R. A. A. Bowler, A. B. Rogers, E. Schneider, S. Charlot, D. P. Stark, K. Shimasaku, S. R. Furlanetto and M. Cirasuolo, "Evolution of the Sizes of Galaxies over 7 < z < 12 Revealed by the 2012 Hubble Ultra Deep Field Campaign", ApJ 777, 2, 155 (2013).

Orlitová, I., A. Verhamme, A. Henry, C. Scarlata, A. Jaskot, M. S. Oey and D. Schaerer, "Puzzling Lyman-alpha line profiles in green pea galaxies", A&A 616, A60 (2018).

Overzier, R. A., R. J. Bouwens, N. J. G. Cross, B. P. Venemans, G. K. Miley, A. W. Zirm, N. Benítez, J. P. Blakeslee, D. Coe, R. Demarco, H. C. Ford, N. L. Homeier, G. D. Illingworth, J. D. Kurk, A. R. Martel, S. Mei, I. Oliveira, H. J. A. Röttgering, Z. I. Tsvetanov and W. Zheng, "Lyman Break Galaxies, Lyα Emitters, and a Radio Galaxy in a Protocluster at z = 4.1", ApJ 673, 1, 143–162 (2008).

Ownsworth, J. R., C. J. Conselice, C. J. Mundy, A. Mortlock, W. G. Hartley, K. Duncan and O. Almaini, "The evolution of galaxies at constant number density: a less biased view of star formation, quenching, and structural formation", MNRAS 461, 1, 1112–1129 (2016).

Oyarzún, G. A., G. A. Blanc, V. González, M. Mateo and I. Bailey, John I., "A Comprehensive Study of Lyα Emission in the High-redshift Galaxy Population", ApJ 843, 2, 133 (2017).

Pacifici, C., S. A. Kassin, B. J. Weiner, B. Holden, J. P. Gardner, S. M. Faber, H. C. Ferguson, D. C. Koo, J. R. Primack, E. F. Bell, A. Dekel, E. Gawiser, M. Giavalisco, M. Rafelski, R. C. Simons, G. Barro, D. J. Croton, R. Davé, A. Fontana, N. A. Grogin, A. M. Koekemoer, S.-K. Lee, B. Salmon, R. Somerville and P. Behroozi, "The Evolution of Star Formation Histories of Quiescent Galaxies", ApJ 832, 1, 79 (2016).

Pandya, V., R. Brennan, R. S. Somerville, E. Choi, G. Barro, S. Wuyts, E. N. Taylor, P. Behroozi, A. Kirkpatrick, S. M. Faber, J. Primack, D. C. Koo, D. H. McIntosh, D. Kocevski, E. F. Bell, A. Dekel, J. J. Fang, H. C. Ferguson, N. Grogin, A. M. Koekemoer, Y. Lu, K. Mantha, B. Mobasher, J. Newman, C. Pacifici, C. Papovich, A. van der Wel and H. M. Yesuf, "The nature of massive transition galaxies in CANDELS, GAMA and cosmological simulations", MNRAS 472, 2, 2054–2084 (2017).

Pasquali, A., A. Gallazzi, F. Fontanot, F. C. van den Bosch, G. De Lucia, H. J. Mo and X. Yang, "Ages and metallicities of central and satellite galaxies: implications for galaxy formation and evolution", MNRAS 407, 2, 937–954 (2010).

Paulino-Afonso, A., D. Sobral, B. Ribeiro, J. Matthee, S. Santos, J. Calhau, A. Forshaw, A. Johnson, J. Merrick, S. Pérez and O. Sheldon, "On the UV compactness and morphologies of typical Lyman α emitters from z $\sim$ 2 to z $\sim$ 6", MNRAS 476, 4, 5479–5501 (2018).

Peebles, P. J. E., "Origin of the Angular Momentum of Galaxies", ApJ 155, 393 (1969).

Peng, C. Y., L. C. Ho, C. D. Impey and H.-W. Rix, "Detailed Structural Decomposition of Galaxy Images", AJ 124, 1, 266–293 (2002).

Peng, C. Y., L. C. Ho, C. D. Impey and H.-W. Rix, "Detailed Decomposition of Galaxy Images. II. Beyond Axisymmetric Models", AJ 139, 6, 2097–2129 (2010a).

Peng, Y.-j., S. J. Lilly, K. Kovač, M. Bolzonella, L. Pozzetti, A. Renzini, G. Zamorani, O. Ilbert, C. Knobel, A. Iovino, C. Maier, O. Cucciati, L. Tasca, C. M. Carollo, J. Silverman, P. Kampczyk, L. de Ravel, D. Sanders, N. Scoville, T. Contini, V. Mainieri, M. Scodeggio, J.-P. Kneib, O. Le Fèvre, S. Bardelli, A. Bongiorno, K. Caputi, G. Coppa, S. de la Torre, P. Franzetti, B. Garilli, F. Lamareille, J.-F. Le Borgne, V. Le Brun, M. Mignoli, E. Perez Montero, R. Pello, E. Ricciardelli, M. Tanaka, L. Tresse, D. Vergani, N. Welikala, E. Zucca, P. Oesch, U. Abbas, L. Barnes, R. Bordoloi, D. Bottini, A. Cappi, P. Cassata, A. Cimatti, M. Fumana, G. Hasinger, A. Koekemoer, A. Leauthaud, D. Maccagni, C. Marinoni, H. McCracken, P. Memeo, B. Meneux, P. Nair, C. Porciani, V. Presotto and R. Scaramella, "Mass and Environment as Drivers of Galaxy Evolution in SDSS and zCOSMOS and the Origin of the Schechter Function", ApJ 721, 1, 193–221 (2010b).

Petrosian, V., "Surface Brightness and Evolution of Galaxies", ApJL 210, L53 (1976).

Pirzkal, N., S. Malhotra, J. E. Rhoads and C. Xu, "Optical-to-Mid-Infrared Observations of Lyα Galaxies at z~5 in the Hubble Ultra Deep Field: A Young and Low-Mass Population", ApJ 667, 1, 49–59 (2007).

Powell, M. C., C. M. Urry, C. N. Cardamone, B. D. Simmons, K. Schawinski, S. Young and M. Kawakatsu, "Morphology and the Color-mass Diagram as Clues to Galaxy Evolution at z&approx1", ApJ 835, 1, 22 (2017).

Pozzetti, L., M. Bolzonella, E. Zucca, G. Zamorani, S. Lilly, A. Renzini, M. Moresco, M. Mignoli, P. Cassata, L. Tasca, F. Lamareille, C. Maier, B. Meneux, C. Halliday, P. Oesch, D. Vergani, K. Caputi, K. Kovač, A. Cimatti, O. Cucciati, A. Iovino, Y. Peng, M. Carollo, T. Contini, J. P. Kneib, O. Le Févre, V. Mainieri, M. Scodeggio, S. Bardelli, A. Bongiorno, G. Coppa, S. de la Torre, L. de Ravel, P. Franzetti, B. Garilli, P. Kampczyk, C. Knobel, J. F. Le Borgne, V. Le Brun, R. Pellò, E. Perez Montero, E. Ricciardelli, J. D. Silverman, M. Tanaka, L. Tresse, U. Abbas, D. Bottini, A. Cappi, L. Guzzo, A. M. Koekemoer, A. Leauthaud, D. Maccagni, C. Marinoni, H. J. McCracken, P. Memeo, C. Porciani, R. Scaramella, C. Scarlata and N. Scoville, "zCOSMOS - 10k-bright spectroscopic sample. The bimodality in the galaxy stellar mass function: exploring its evolution with redshift", A&A 523, A13 (2010).

Proctor, R. N. and A. E. Sansom, "A comparison of stellar populations in galaxy spheroids across a wide range of Hubble types", MNRAS 333, 3, 517–543 (2002).

Rhoads, J. E., S. Malhotra, A. Dey, D. Stern, H. Spinrad and B. T. Jannuzi, "First Results from the Large-Area Lyman Alpha Survey", ApJL 545, 2, L85–L88 (2000).

Rhoads, J. E., S. Malhotra, M. L. A. Richardson, S. L. Finkelstein, J. P. U. Fynbo, E. M. McLinden and V. S. Tilvi, "The Dynamical Masses, Densities, and Star Formation Scaling Relations of Lyα Galaxies", ApJ 780, 1, 20 (2014).

Ribeiro, B., O. Le Fèvre, L. A. M. Tasca, B. C. Lemaux, P. Cassata, B. Garilli, D. Maccagni, G. Zamorani, E. Zucca, R. Amorín, S. Bardelli, A. Fontana, M. Giavalisco, N. P. Hathi, A. Koekemoer, J. Pforr, L. Tresse and J. Dunlop, "Size evolution of star-forming galaxies with 2 <z < 4.5 in the VIMOS Ultra-Deep Survey", A&A 593, A22 (2016).

Ritondale, E., M. W. Auger, S. Vegetti and J. P. McKean, "Resolving on 100 pc scales the UV-continuum in Lyman-α emitters between redshift 2 and 3 with gravitational lensing", MNRAS 482, 4, 4744–4762 (2019).

Saintonge, A., L. J. Tacconi, S. Fabello, J. Wang, B. Catinella, R. Genzel, J. Graciá-Carpio, C. Kramer, S. Moran, T. M. Heckman, D. Schiminovich, K. Schuster and S. Wuyts, "The Impact of Interactions, Bars, Bulges, and Active Galactic Nuclei on Star Formation Efficiency in Local Massive Galaxies", ApJ 758, 2, 73 (2012).

Salim, S. and R. M. Rich, "Star Formation Signatures in Optically Quiescent Early-type Galaxies", ApJL 714, 2, L290–L294 (2010).

Salimbeni, S., E. Giallongo, N. Menci, M. Castellano, A. Fontana, A. Grazian, L. Pentericci, D. Trevese, S. Cristiani, M. Nonino and E. Vanzella, "The red and blue galaxy populations in the GOODS field: evidence for an excess of red dwarfs", A&A 477, 3, 763–773 (2008).

Salpeter, E. E., "The Luminosity Function and Stellar Evolution.", ApJ 121, 161 (1955).

Sandage, A. and N. Visvanathan, "The color - absolute magnitude relation for E and S0 galaxies. II. New colors, magnitudes, and types for 405 galaxies.", ApJ 223, 707–729 (1978).

Santini, P., H. C. Ferguson, A. Fontana, B. Mobasher, G. Barro, M. Castellano, S. L. Finkelstein, A. Grazian, L. T. Hsu, B. Lee, S. K. Lee, J. Pforr, M. Salvato, T. Wiklind, S. Wuyts, O. Almaini, M. C. Cooper, A. Galametz, B. Weiner, R. Amorin, K. Boutsia, C. J. Conselice, T. Dahlen, M. E. Dickinson, M. Giavalisco, N. A. Grogin, Y. Guo, N. P. Hathi, D. Kocevski, A. M. Koekemoer, P. Kurczynski, E. Merlin, A. Mortlock, J. A. Newman, D. Paris, L. Pentericci, R. Simons and S. P. Willner, "Stellar Masses from the CANDELS Survey: The GOODS-South and UDS Fields", ApJ 801, 2, 97 (2015).

Santini, P., A. Fontana, A. Grazian, S. Salimbeni, F. Fiore, F. Fontanot, K. Boutsia, M. Castellano, S. Cristiani, C. de Santis, S. Gallozzi, E. Giallongo, N. Menci, M. Nonino, D. Paris, L. Pentericci and E. Vanzella, "Star formation and mass assembly in high redshift galaxies", A&A 504, 3, 751–767 (2009).

Schaerer, D. and S. de Barros, "The impact of nebular emission on the ages of z≈ 6 galaxies", A&A 502, 2, 423–426 (2009).

Schawinski, K., C. M. Urry, B. D. Simmons, L. Fortson, S. Kaviraj, W. C. Keel, C. J. Lintott, K. L. Masters, R. C. Nichol, M. Sarzi, R. Skibba, E. Treister, K. W. Willett, O. I. Wong and S. K. Yi, "The green valley is a red herring: Galaxy Zoo reveals two evolutionary pathways towards quenching of star formation in early- and late-type galaxies", MNRAS 440, 1, 889–907 (2014).

Sersic, J. L., *Atlas de Galaxias Australes* (1968).

Shen, S., H. J. Mo, S. D. M. White, M. R. Blanton, G. Kauffmann, W. Voges, J. Brinkmann and I. Csabai, "The size distribution of galaxies in the Sloan Digital Sky Survey", MNRAS 343, 3, 978–994 (2003).

Shibuya, T., M. Ouchi and Y. Harikane, "Morphologies of 190,000 Galaxies at z = 0-10 Revealed with HST Legacy Data. I. Size Evolution", APJS 219, 2, 15 (2015).

Shibuya, T., M. Ouchi, Y. Harikane and K. Nakajima, "Morphologies of ∼190,000 Galaxies at z = 0-10 Revealed with HST Legacy Data. III. Continuum Profile and Size Evolution of Lyα Emitters", ApJ 871, 2, 164 (2019).

Shimasaku, K., M. Fukugita, M. Doi, M. Hamabe, T. Ichikawa, S. Okamura, M. Sekiguchi, N. Yasuda, J. Brinkmann, I. Csabai, S.-I. Ichikawa, Z. Ivezić, P. Z. Kunszt, D. P. Schneider, G. P. Szokoly, M. Watanabe and D. G. York, "Statistical Properties of Bright Galaxies in the Sloan Digital Sky Survey Photometric System", AJ 122, 3, 1238–1250 (2001).

Silich, S. and G. Tenorio-Tagle, "Gas expulsion versus gas retention in young stellar clusters-II. Effects of cooling and mass segregation", MNRAS 478, 4, 5112–5122 (2018).

Song, M., S. L. Finkelstein, K. Gebhardt, G. J. Hill, N. Drory, M. L. N. Ashby, G. A. Blanc, J. Bridge, T. Chonis, R. Ciardullo, M. Fabricius, G. G. Fazio, E. Gawiser, C. Gronwall, A. Hagen, J.-S. Huang, S. Jogee, R. Livermore, B. Salmon, D. P. Schneider, S. P. Willner and G. R. Zeimann, "The HETDEX Pilot Survey. V. The Physical Origin of Lyα Emitters Probed by Near-infrared Spectroscopy", ApJ 791, 1, 3 (2014).

Springel, V., T. Di Matteo and L. Hernquist, "Black Holes in Galaxy Mergers: The Formation of Red Elliptical Galaxies", ApJL 620, 2, L79–L82 (2005).

Storey, P. J. and D. G. Hummer, "Recombination line intensities for hydrogenic ions-IV. Total recombination coefficients and machine-readable tables for Z=1 to 8", MNRAS 272, 1, 41–48 (1995).

Strateva, I., Ž. Ivezić, G. R. Knapp, V. K. Narayanan, M. A. Strauss, J. E. Gunn, R. H. Lupton, D. Schlegel, N. A. Bahcall, J. Brinkmann, R. J. Brunner, T. Budavári, I. Csabai, F. J. Castander, M. Doi, M. Fukugita, Z. Győry, M. Hamabe, G. Hennessy, T. Ichikawa, P. Z. Kunszt, D. Q. Lamb, T. A. McKay, S. Okamura, J. Racusin, M. Sekiguchi, D. P. Schneider, K. Shimasaku and D. York, "Color Separation of Galaxy Types in the Sloan Digital Sky Survey Imaging Data", AJ 122, 4, 1861–1874 (2001).

Tacchella, S., C. M. Carollo, A. Renzini, N. M. F. Schreiber, P. Lang, S. Wuyts, G. Cresci, A. Dekel, R. Genzel, S. J. Lilly, C. Mancini, S. Newman, M. Onodera, A. Shapley, L. Tacconi, J. Woo and G. Zamorani, "Evidence for mature bulges and an inside-out quenching phase 3 billion years after the Big Bang", Science 348, 6232, 314–317 (2015).

Tacchella, S., A. Dekel, C. M. Carollo, D. Ceverino, C. DeGraf, S. Lapiner, N. Mand elker and J. R. Primack, "Evolution of density profiles in high-z galaxies: compaction and quenching inside-out", MNRAS 458, 1, 242–263 (2016).

Taniguchi, Y., T. Murayama, N. Z. Scoville, S. S. Sasaki, T. Nagao, Y. Shioya, T. Saito, Y. Ideue, A. Nakajima, K. Matsuoka, D. B. Sanders, B. Mobasher, H. Aussel, P. Capak, M. Salvato, A. Koekemoer, C. Carilli, A. Cimatti, R. S. Ellis, B. Garilli, M. Giavalisco, O. Ilbert, C. D. Impey, M. G. Kitzbichler, O. Le Fèvre, H. J. McCracken, C. Scarlata, E. Schinnerer, V. Smolcic, S. Tribiano and J. R. Trump, "Hubble Space Telescope/Advanced Camera for Surveys Morphology of Lyα Emitters at Redshift 5.7 in the COSMOS Field", ApJ 701, 2, 915–944 (2009).

Tojeiro, R., K. L. Masters, J. Richards, W. J. Percival, S. P. Bamford, C. Maraston, R. C. Nichol, R. Skibba and D. Thomas, "The different star formation histories of blue and red spiral and elliptical galaxies", MNRAS 432, 1, 359–373 (2013).

Trager, S. C., S. M. Faber, G. Worthey and J. J. González, "The Stellar Population Histories of Early-Type Galaxies. II. Controlling Parameters of the Stellar Populations", AJ 120, 1, 165–188 (2000).

Tremonti, C. A., T. M. Heckman, G. Kauffmann, J. Brinchmann, S. Charlot, S. D. M. White, M. Seibert, E. W. Peng, D. J. Schlegel, A. Uomoto, M. Fukugita and J. Brinkmann, "The Origin of the Mass-Metallicity Relation: Insights from 53,000 Star-forming Galaxies in the Sloan Digital Sky Survey", ApJ 613, 2, 898–913 (2004).

van der Wel, A., E. F. Bell, B. Häussler, E. J. McGrath, Y.-Y. Chang, Y. Guo, D. H. McIntosh, H. W. Rix, M. Barden, E. Cheung, S. M. Faber, H. C. Ferguson, A. Galametz, N. A. Grogin, W. Hartley, J. S. Kartaltepe, D. D. Kocevski, A. M. Koekemoer, J. Lotz, M. Mozena, M. A. Peth and C. Y. Peng, "Structural Parameters of Galaxies in CANDELS", ApJL 203, 2, 24 (2012).

van der Wel, A., M. Franx, P. G. van Dokkum, R. E. Skelton, I. G. Momcheva, K. E. Whitaker, G. B. Brammer, E. F. Bell, H. W. Rix, S. Wuyts, H. C. Ferguson, B. P. Holden, G. Barro, A. M. Koekemoer, Y.-Y. Chang, E. J. McGrath, B. Häussler, A. Dekel, P. Behroozi, M. Fumagalli, J. Leja, B. F. Lundgren, M. V. Maseda, E. J. Nelson, D. A. Wake, S. G. Patel, I. Labbé, S. M. Faber, N. A. Grogin and D. D. Kocevski, "3D-HST+CANDELS: The Evolution of the Galaxy Size-Mass Distribution since z = 3", ApJ 788, 1, 28 (2014).

van Dokkum, P. G. and M. Franx, "The Fundamental Plane in CL 0024 at z = 0.4: implications for the evolution of the mass-to-light ratio.", MNRAS 281, 3, 985–1000 (1996).

van Dokkum, P. G., K. E. Whitaker, G. Brammer, M. Franx, M. Kriek, I. Labbé, D. Marchesini, R. Quadri, R. Bezanson, G. D. Illingworth, A. Muzzin, G. Rudnick, T. Tal and D. Wake, "The Growth of Massive Galaxies Since z = 2", ApJ 709, 2, 1018–1041 (2010).

Vazdekis, A., E. Ricciardelli, A. J. Cenarro, J. G. Rivero-González, L. A. Díaz-García and J. Falcón-Barroso, "MIUSCAT: extended MILES spectral coverage - I. Stellar population synthesis models", MNRAS 424, 1, 157–171 (2012).

Verhamme, A., I. Orlitová, D. Schaerer and M. Hayes, "Using Lyman-α to detect galaxies that leak Lyman continuum", A&A 578, A7 (2015).

Verhamme, A., I. Orlitová, D. Schaerer, Y. Izotov, G. Worseck, T. X. Thuan and N. Guseva, "Lyman-α spectral properties of five newly discovered Lyman continuum emitters", A&A 597, A13 (2017).

Verhamme, A., D. Schaerer and A. Maselli, "3D Lyα radiation transfer. I. Understanding Lyα line profile morphologies", A&A 460, 2, 397–413 (2006).

Vulcani, B., B. M. Poggianti, J. Fritz, G. Fasano, A. Moretti, R. Calvi and A. Paccagnella, "From Blue Star-forming to Red Passive: Galaxies in Transition in Different Environments", ApJ 798, 1, 52 (2015).

Warren, M. S., P. J. Quinn, J. K. Salmon and W. H. Zurek, "Dark Halos Formed via Dissipationless Collapse. I. Shapes and Alignment of Angular Momentum", ApJ 399, 405 (1992).

Whitaker, K. E., R. Bezanson, P. G. van Dokkum, M. Franx, A. van der Wel, G. Brammer, N. M. Förster-Schreiber, M. Giavalisco, I. Labbé, I. G. Momcheva, E. J. Nelson and R. Skelton, "Predicting Quiescence: The Dependence of Specific Star Formation Rate on Galaxy Size and Central Density at 0.5 < z < 2.5", ApJ 838, 1, 19 (2017).

Whitaker, K. E., M. Franx, R. Bezanson, G. B. Brammer, P. G. van Dokkum, M. T. Kriek, I. Labbé, J. Leja, I. G. Momcheva, E. J. Nelson, J. R. Rigby, H.-W. Rix, R. E. Skelton, A. van der Wel and S. Wuyts, "Galaxy Structure as a Driver of the Star Formation Sequence Slope and Scatter", ApJL 811, 1, L12 (2015).

Whitaker, K. E., I. Labbé, P. G. van Dokkum, G. Brammer, M. Kriek, D. Marchesini, R. F. Quadri, M. Franx, A. Muzzin, R. J. Williams, R. Bezanson, G. D. Illingworth, K.-S. Lee, B. Lundgren, E. J. Nelson, G. Rudnick, T. Tal and D. A. Wake, "The NEWFIRM Medium-band Survey: Photometric Catalogs, Redshifts, and the Bimodal Color Distribution of Galaxies out to z ~3", ApJ 735, 2, 86 (2011).

Whitaker, K. E., P. G. van Dokkum, G. Brammer and M. Franx, "The Star Formation Mass Sequence Out to z = 2.5", ApJL 754, 2, L29 (2012).

Williams, C. C., M. Giavalisco, R. Bezanson, N. Cappelluti, P. Cassata, T. Liu, B. Lee, E. Tundo and E. Vanzella, "Morphology Dependence of Stellar Age in Quenched Galaxies at Redshift ∼1.2: Massive Compact Galaxies Are Older than More Extended Ones", ApJ 838, 2, 94 (2017).

Williams, R. J., R. F. Quadri, M. Franx, P. van Dokkum and I. Labbé, "Detection of Quiescent Galaxies in a Bicolor Sequence from Z = 0-2", ApJ 691, 2, 1879–1895 (2009).

Windhorst, R. A., S. H. Cohen, N. P. Hathi, P. J. McCarthy, J. Ryan, Russell E., H. Yan, I. K. Baldry, S. P. Driver, J. A. Frogel, D. T. Hill, L. S. Kelvin, A. M. Koekemoer, M. Mechtley, R. W. O'Connell, A. S. G. Robotham, M. J. Rutkowski, M. Seibert, A. N. Straughn, R. J. Tuffs, B. Balick, H. E. Bond, H. Bushouse, D. Calzetti, M. Crockett, M. J. Disney, M. A. Dopita, D. N. B. Hall, J. A. Holtzman, S. Kaviraj, R. A. Kimble, J. W. MacKenty, M. Mutchler, F. Paresce, A. Saha, J. I. Silk, J. T. Trauger, A. R. Walker, B. C. Whitmore and E. T. Young, "The Hubble Space Telescope Wide Field Camera 3 Early Release Science Data: Panchromatic Faint Object Counts for 0.2-2 μm Wavelength", APJS 193, 2, 27 (2011).

Wuyts, S., N. M. Förster Schreiber, A. van der Wel, B. Magnelli, Y. Guo, R. Genzel, D. Lutz, H. Aussel, G. Barro, S. Berta, A. Cava, J. Graciá-Carpio, N. P. Hathi,

K.-H. Huang, D. D. Kocevski, A. M. Koekemoer, K.-S. Lee, E. Le Floc'h, E. J. McGrath, R. Nordon, P. Popesso, F. Pozzi, L. Riguccini, G. Rodighiero, A. Saintonge and L. Tacconi, "Galaxy Structure and Mode of Star Formation in the SFR-Mass Plane from z ~2.5 to z ~0.1", ApJ 742, 2, 96 (2011).

Wyithe, J. S. B. and A. Loeb, "Extrapolating the evolution of galaxy sizes to the epoch of reionization", MNRAS 413, 1, L38–L42 (2011).

Yang, H., S. Malhotra, M. Gronke, J. E. Rhoads, M. Dijkstra, A. Jaskot, Z. Zheng and J. Wang, "Green Pea Galaxies Reveal Secrets of Lyα Escape", ApJ 820, 2, 130 (2016).

Yang, H., S. Malhotra, M. Gronke, J. E. Rhoads, C. Leitherer, A. Wofford, T. Jiang, M. Dijkstra, V. Tilvi and J. Wang, "Lyα Profile, Dust, and Prediction of Lyα Escape Fraction in Green Pea Galaxies", ApJ 844, 2, 171 (2017a).

Yang, H., S. Malhotra, M. Gronke, J. E. Rhoads, C. Leitherer, A. Wofford, T. Jiang, M. Dijkstra, V. Tilvi and J. Wang, "Lyα Profile, Dust, and Prediction of Lyα Escape Fraction in Green Pea Galaxies", ApJ 844, 2, 171 (2017b).

Yang, H., S. Malhotra, J. E. Rhoads, C. Leitherer, A. Wofford, T. Jiang and J. Wang, "Lyα and UV Sizes of Green Pea Galaxies", ApJ 838, 1, 4 (2017c).